Dipl.-Physiker Moritz Theisen

Aggregation of Rb and Cs atoms on helium nanodroplets and laser ionization of cold clusters

DOCTORAL THESIS

For obtaining the academic degree of
Doktor der Naturwissenschaften

Doctoral Programme of Natural Sciences
Technical Physics

Graz University of Technology

Supervisor:
Univ.-Prof. Dipl.-Phys. Dr.rer.nat Wolfang Ernst
Institute of Experimental Physics

Graz, September 2011

Acknowledgement

First and foremost I want to thank my advisor Univ.-Prof. Dipl.-Phys. Dr. rer. nat Wolfgang E. Ernst. I would like to thank for his brilliant mentoring and his dedicated and friendly support. He has made available his support in a number of ways.

I owe my deepest gratitude to Prof. Dr. Goran Pichler for his friendly support and for his correction of this thesis.

Carlo Callegari introduced me into the helium droplet world. I am grateful for his extraordinary helpfulness and many fruitful discussions about the concerning physics behind the experiments.

I would like to thank all members of the Institute of Experimental Physics for the pleasant and cooperative working atmosphere. I am especially grateful to Florian Lackner, Günter Krois, and Markus Krug, who made this thesis possible. Markus Koch has made available his support in a number of ways and advised me in many technical aspects. I would like to show my gratitude to Johannes Poms and Alexander Volk, who performed many helium droplet related calculations with me. I am also indebted to my many student colleagues for providing a stimulating and fun environment in which to learn and grow. I would like to thank Martin Ratschek, Andreas Kautsch, Matthias Hasewend, Anton Tamtögl, Michael Mayrhofer-Reinhartshuber, and Patrick Kraus.

I also want to mention Josef Friedrich, Reinhard Dämon, and Christian Neureiter of the electric workshop, who always helped, when I had problems with the electronics. I also appreciate the help of Rupert Maierhofer, Werner Luttenberger, and Uwe Seidl of the mechanical workshop, who manufactured several constructions.

Lastly and most importantly, I wish to thank my wife Kerstin, who always helped me out of stressful days.

Abstract

Superfluid helium droplets (He_N) have attracted strong interest as cold hosts for the investigation of weakly bound molecules. While the host-dopant interaction is weak for neutral molecules, ion impurities may be surrounded by frozen shells of polarized helium (He) atoms. An extreme example of the different behavior is given by alkali metal (Ak) impurities that stay at the surface of the droplet but immerse into the droplet as cations releasing a considerable amount of binding energy.

The experimental and theoretical results of this thesis are presented in the following way: First, two-photon experiments and two-step excitations of rubidium (Rb) on helium droplets are presented. Here, the bound character of the $5^2P_{1/2}$ ($^2\Pi_{1/2}$) state of Rb on the helium droplet has been used to further excite an Ak atom fully attached to the surface of a helium droplet. The excitation of the Ak atom is of the form $n^2D \leftarrow n^2P \leftarrow n^2S$.

Second, the formation of Rb^+ snowballs in the center of He_N is shown after the ionization of single Rb atoms on He_N using resonant two-photon ionization. The possibility to create large artificial atoms consisting of an Ak ion core surrounded by He is discussed.

Third, the behavior of cesium (Cs) atoms on He droplets has been re-examined and compared with results of other groups. We found that Cs does not desorb from the surface of the He droplet when excited with certain photon energies close to its $6^2P_{1/2}$ ($^2\Pi_{1/2}$) state similar as Rb. Moreover, we use this behavior to form Cs^+ snowballs in the center of the He droplet.

Fourth, the formation of a positive charge inside the helium droplet with an electron orbiting around the complex is of tremendous fundamental interest and is often called Sekatskii atom. The creation of Rydberg states of Ak atoms on helium droplets with $n \sim 100$ may be an option to create such a system. With this in mind we monitored the shift of the ionization threshold of Rb and Cs atoms due to the influence of the helium droplet as well as the lifetime of highly excited states of Cs atoms on He_N.

Fifth, Ak clusters (Ak_n) are formed on the helium droplet and are examined. The formation process of the Ak_n leads to different species. The clusters can exist in low- and high-spin configurations, which should show different properties.

Kurzfassung

Suprafluide Heliumnanotröpfchen werden als Matrix zur Untersuchung von schwach gebundenen Molekülen genutzt und haben in den letzten Jahren großes Interesse erfahren. Die Wechselwirkung zwischen Heliumnanotröpfchen und Dotiersubstanz ist im Fall von neutralen Molekülen gering. Im Gegensatz hierzu können ionische Fremdkörper von gefrorenen Heliumschalen umgeben sein. Ein Extrembeispiel für das unterschiedliche Verhalten von neutralen und ionischen Teilchen sind Alkaliatome. Während das Alkaliatom sich auf der Oberfläche des Heliumnanotröpfchens befindet, dringt das Kation unter Freisetzung von Bindungsenergie in das Tröpfchen ein.

Die experimentellen und theoretischen Resultate werden in folgender Reihenfolge dargestellt: Zunächst wurden Zwei-Photonen-Experimente und Zwei-Stufen-Anregungen von Rubidium (Rb) auf Heliumnanotröpfchen untersucht. Auf Grund des gebundenen Charakters des $5^2\mathrm{P}_{1/2}$ ($^2\Pi_{1/2}$) Zustands von Rb auf Heliumnanotröpfchen kann das Alkaliatom in höhere elektronische Zustände angeregt werden, wobei es sich während der Anregungen auf der Oberfläche des Heliumnanotröpfchens befindet. Die untersuchte Anregung des Alkaliatoms ist von der Form $n^2\mathrm{D}\leftarrow n^2\mathrm{P}\leftarrow n^2\mathrm{S}$.

Des Weiteren wurde die Bildung von Rb^+ Schneebällen, die sich im Zentrum des Heliumnanotröpfchens befinden, nach resonanter Zwei-Photonen-Ionisation beobachtet. In diesem Zusammenhang wird die Möglichkeit diskutiert, ein großes künstliches Atom zu erzeugen, welches aus einem Alkalikation umgeben vom Heliumtröpfchen besteht.

Die Eigenschaften von Cäsiumatomen (Cs) auf Heliumnanotröpfchen wurden erneut untersucht und mit Resultaten von anderen Arbeitsgruppen verglichen. Eine wichtiges neues Ergebnis ist, dass Cs ähnlich wie Rb nicht von der Oberfläche des Tröpfchens desorbiert, wenn Cs mit Photonenenergien nahe seines $6^2\mathrm{P}_{1/2}$ ($^2\Pi_{1/2}$) Zustands angeregt wird. Mit dieser Erkenntnis ist es gelungen, Cs^+ Schneebälle im Inneren des Tröpfchens zu formen.

Die Erzeugung einer positiven Ladung im Tröpfchen mit einem Elektron, welches sich außerhalb dieses Komplexes befindet, wird in der Literatur als Sekatskii-Atom bezeichnet. Die Erzeugung von Rydbergzuständen von Alkaliatomen mit $n \sim 100$ wäre eine Möglichkeit ein solches ungewöhnliches Rydbergsystem zu kreieren. Vor diesem Hin-

tergrund wurde sowohl die Verschiebung der Ionisationsenergien von Rubidium- und Cäsiumatomen, die durch den Einfluss des Tröpfchens verursacht wird, als auch die Lebensdauer von hochangeregten Zuständen des Cäsiumatoms auf Heliumnanotröpfchen beobachtet.

Den Abschluss der Arbeit bildet die Erzeugung und Untersuchung von Alkaliclustern (Ak_n), die sich auf Heliumnanotröpfchen bilden. Auf Grund des Erzeugungsprozesses entstehen Ak_n in verschiedenen Zuständen. Die Cluster können sowohl in Niedrig- als auch in Hochspin Zuständen existieren und sollten unterschiedliche Eigenschaften aufweisen.

Articles related to this work

During the time of the thesis the following articles have been published:

- M. Theisen, F. Lackner, F. Ancilotto, C. Callegari, and W. E. Ernst, Two-step excitation of Rb atoms on He nanodroplets, European Physical Journal D **61** (2011), 403, DOI: 10.1140/epjd/e2010-10504-5.[1]

- M. Theisen, F. Lackner, and W. E. Ernst, Forming Rb^+ snowballs in the center of He nanodroplets, Phys. Chem. Chem. Phys. 12 (2010), 14861, DOI: 10.1039/C0CP01283A (cover article).[2]

- M. Theisen, F. Lackner, and W. E. Ernst, Rb and Cs Oligomers in Different Spin Configurations on Helium Nanodroplets, J. Chem. Phys. A, **115** (2011), 7005, special issue: J. P. Toennies Festschrift, DOI: 10.1021/jp112223k.[3]

- M. Theisen, F. Lackner, and W. E. Ernst, Cs atoms on helium nanodroplets and the immersion of Cs^+ into the nanodroplet, J. Chem. Phys. 135 (2011), 074306, DOI: 10.1063/1.3624840;[4] also published in the Virtual Journal of Nanoscale Science & Technology, 24 (2011), issue 10.

- M. Theisen, F. Lackner, G. Krois, and W. E. Ernst, Ionization Thresholds of Alkali Metal Atoms on He Droplets, J. Phys. Chem. Lett. handed in (2011).

- F. Lackner, G. Krois, M. Theisen, M. Koch, and W. E. Ernst, Spectroscopy of nS, nP, and nD Rydberg series of Cs atoms on helium nanodroplets, Phys. Chem. Chem. Phys. in press (2011), DOI: 10.1039/C1CP21280J.[5]

In this thesis we present the results of the first five named articles. The last one will be presented in detail in the thesis of F. Lackner in the near future. We are confident that there will be more articles written based on our experimental work and theoretical findings.

Deutsche Fassung:
Beschluss der Curricula-Kommission für Bachelor-, Master- und Diplomstudien vom 10.11.2008
Genehmigung des Senates am 1.12.2008

EIDESSTATTLICHE ERKLÄRUNG

Ich erkläre an Eides statt, dass ich die vorliegende Arbeit selbstständig verfasst, andere als die angegebenen Quellen/Hilfsmittel nicht benutzt, und die den benutzten Quellen wörtlich und inhaltlich entnommene Stellen als solche kenntlich gemacht habe.

Graz, am ……. ……..
(Unterschrift)

Englische Fassung:

STATUTORY DECLARATION

I declare that I have authored this thesis independently, that I have not used other than the declared sources / resources, and that I have explicitly marked all material which has been quoted either literally or by content from the used sources.

……. ……..
date (signature)

Contents

List of Figures

List of Tables

1. Introduction

The possibility to create atoms and molecules on the surface or in the interior of rare gas clusters allows one to study systems isolated in a nanoscale host. The clusters consist of up to several thousand rare gas atoms, which are weakly bound to each other, and can be are widely used isolating atoms or molecules.

Tailored systems can be created by a pick-up technique, where the clusters are subsequently doped with foreign complexes. These systems can be experimentally manipulated, which allows one to study the interaction between dopant and cluster, too.[6] The study of single complexes itself can be seen as a link between an atomic and a macroscopic picture.

Clusters or droplets consisting of helium (He) atoms are moreover a nearly ideal spectroscopic matrix. They build an isothermal low-temperature environment ($T \sim 370\,mK$ for ^4He), where single atoms or molecules can be examined. ^4He nanodroplets (^4He_N) give us the possibility to study the effect of superfluidity on a microscopic scale. Due to the low interaction between ^4He and other molecules the disturbance induced by the He_N is very low compared to other matrix isolation techniques. The research done on systems consisting of doped He nanodroplets is part of the fundamental research in physics and physical chemistry.

In this work the interaction between single alkali-metal (Ak) atoms in higher electronic states as well as the interaction between Ak^+ ions with the He nanodroplet are examined. In addition, large Ak_n clusters of the heavy Ak atoms rubidium (Rb) and cesium (Cs) on He_N in different spin configurations are observed for the first time.

In this chapter we present theoretical aspects of He nanodroplets as well as a motivation for the experiments. First the properties of liquid He are discussed. Second the production of He nanodroplets and aspects about supersonic beam expansion will be explained. At the end of this chapter we give an overview of the current scientific developments in this specific field, which leads to our motivation.

1.1. Helium

Rare gases are known as the most inert elements, which means among other things that they cannot share electrons with other elements in chemical bonds easily. This originates from their filled electronic shells. Here, helium has been aggregated to liquid nanodroplets or clusters. In the following we explain the properties of this noble gas as well as the production of He nanodroplets or clusters in detail.

Helium is the lightest rare gas and is known as the most inert element. It has been first discovered by Jules Janssen in 1868 as a spectral line at a solar eclipse.[7] Nearly 30 years later helium was found on earth by William Ramsay in 1895. The first time helium was liquified was in 1908 done by Heike Kamerlingh Onnes. There are several features of helium, which were discovered soon: e.g. helium could not be solidified at this time. Furthermore, there is a singularity and a density maximum in the temperature profile of the specific heat at 2.2 K. All this phenomena can be explained with today's knowledge.

There are two stable isotopes (^{3}He, ^{4}He) with an ionization potential of $\sim 24.59\,\mathrm{eV}$.[8] Both have two protons and one (^{3}He) or two (^{4}He) neutrons, which defines ^{3}He as a fermion with a resulting spin of $1/2$ and ^{4}He as a boson with a resulting spin of 0. Their ground-state configuration is $1s^2$, so that no p-part exists in their ground state. Their boiling points are 3.19 K and 4.21 K, and at atmospheric pressure both remain liquid at zero temperature (Fig. 1.1). Liquid ^{4}He as well as ^{3}He have special characteristics.

At the so-called λ-point ^{4}He undergoes a phase transition. Above the λ-temperature of 2.18 K at 1 atm it is called He I; below He II (cf. Fig. 1.1), whereby both have different properties.[7] He I behaves like a usual fluid in contrast to He II being superfluid.

^{3}He also undergoes a phase transition, but at much lower temperature (2.6 mK) at 1 atm. The reason for the different behavior of ^{4}He and ^{3}He is the quantum statistics. For fermions like ^{3}He-atoms it is forbidden by the Pauli exclusion principle that more than one fermion is in the same one-particle state. ^{3}He-atoms form weakly bound pairs, so called Cooper pairs, at the λ-point. These pairs have in sum zero spin and behave as bosons, which explains their superfluidity. As ^{3}He has not been used in our experiments, we only describe the properties of ^{4}He in the following.

Macroscopic as well as microscopic objects can move without fiction inside a superfluid up to a certain speed limit, which is called Landau velocity.[9] The heat conductivity in He II is so high, that there is no temperature gradient inside the fluid and the evaporation takes place only at the surface. This has been studied by Kapitza[10] as well as by Allen and Misener[11] in 1938. By watching the oscillation of a torsional pendulum, which

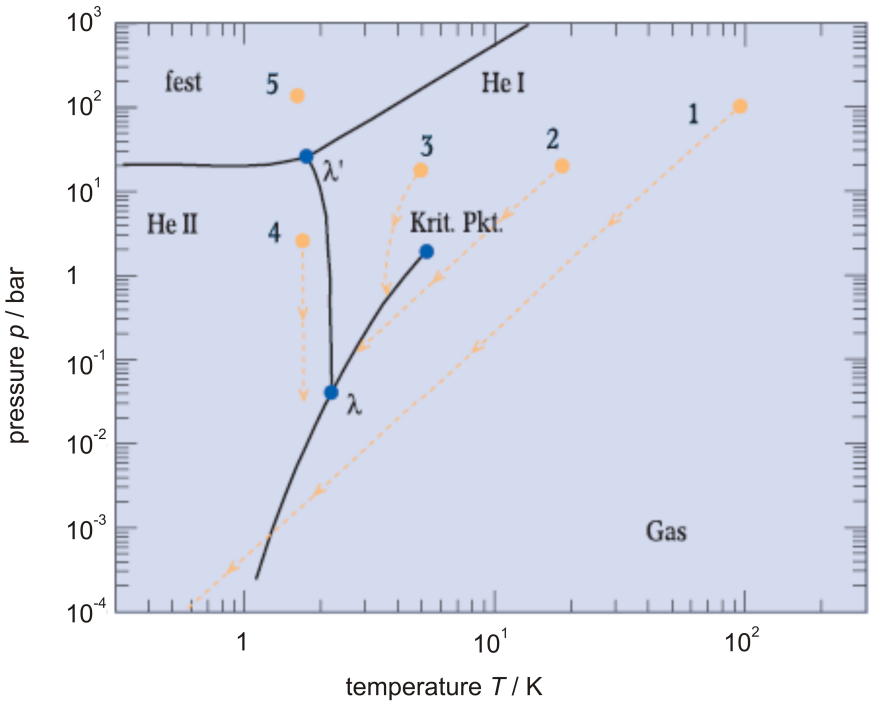

Figure 1.1.: In the phase diagram of ^{4}He the different possibilities to form He droplets are displayed. Most expansion modes follow an isentrope, which cuts the vapor pressure curve. The different points (1-5) correspond to different temperatures and pressures of the source and lead to different maximum He droplet sizes. 1: atomic beam with high intensity; 2: He droplets ($\bar{N}_i \leq 10^4$ He atoms); 3: He droplets ($\bar{N}_i \leq 10^7$ He atoms); 4: He droplets ($\bar{N}_i \leq 10^{12}$ He atoms) and slow velocities ($v \sim 15\,\mathrm{m/s}$); 5: He II expansion from solid He.[6] Here, mainly He droplets from starting point 2 are used. Fig. taken from Ref. 6 (modified).

is submerged in liquid helium, it was seen that the moment of inertia of the pendulum decreases below the λ-point,[12] meaning that there is only small viscosity and entropy. Tisza[13] and later Landau[9] explained this by a two-liquid model, where one component is normal and the other is superfluid. The proportion of the two components in He II is temperature-dependent. At the λ-point ^{4}He consists only of the normal component and acts as an usual fluid. At zero temperature it consists of the superfluid part only.

A good explanation for the Landau velocity is given by McClintock.[14] By exciting superfluid He the normal fluid is formed and thermal energy is created. The excitations consist of two density fluctuations, rotons and phonons. Rotons are low temperature excitations with an energy of $\sim 6\,\mathrm{cm}^{-1}$ (cf. Fig. 1.2).[15] Phonons are sound waves with an energy of

$$E = c\hbar k, \tag{1.1}$$

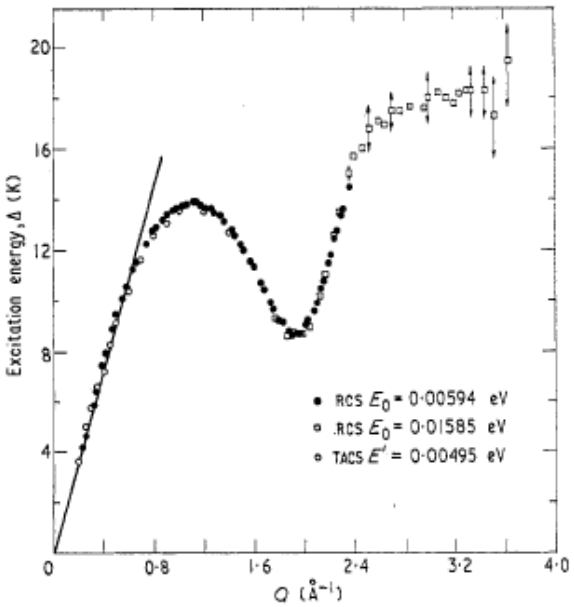

Figure 1.2.: Dispersion curve of superfluid ^{4}He at 1.1 K taken from Ref. 16.

where c is the velocity of sound, $\hbar$ is Planck's constant and k is the wave vector. The dispersion curve of superfluid helium (Fig. 1.2) shows two minima at $Q \to 0\,\text{Å}^{-1}$ and $Q \to 2\,\text{Å}^{-1}$ and a maximum at $Q \to 1.2\,\text{Å}^{-1}$.

The first region from 0 Å to the maximum is called phonon branch; the second one roton branch. The energy and momentum conservation conditions for the creation of a single roton have been studied by Landau[9] and have led to an upper limit for the superflow's velocity

$$\frac{d\epsilon}{dp} \geq \frac{\epsilon}{p}. \tag{1.2}$$

If this velocity is excessed in the case of elementary excitation, multiple rotons are created. The same holds also for the motion of microscopic objects through He II, whereby the velocity is mass-dependent. For infinite masses the Landau-velocity is $v_L \sim 58\,\text{m/s}$. At higher velocities the energy of the moving microscopic object is dissipated by creating a pair of rotons.

The interaction between rare gas atoms can be described with a Tang-Toennies potential model, which characterizes the van der Waals potentials in an accurate way (Fig. 1.3).[17,18] Calculations predict only one weakly bound state for the dimer with a binding energy of $\sim 1.3\,\text{mK}$.[17,19] Due to these low binding energies He dimers and

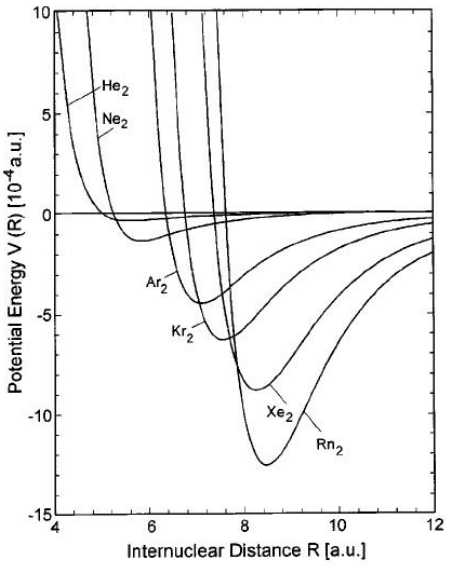

Figure 1.3.: Calculated potentials of the homonuclear noble gas dimers: He_2, Ne_2, Ar_2, Kr_2, Xe_2, and Rn_2. Fig. taken from Ref. 18.

trimers were first observed in a non-destructive way some years ago by Schollköpf and Toennies.[20,21] Nevertheless, He atoms can agglomerate more easily to droplets under certain conditions.

1.2. Helium nanodroplets

He nanodroplets (He_N) are usually produced by a supersonic free-jet expansion of cold gaseous He. The formation of clusters was already observed at the beginning of supersonic beam experiments. With He this was first shown by Becker in 1961.[22] In our days, He nanodroplets are mostly produced by expanding gas or liquid at high stagnation pressure of $p_0 = 20 - 100\,\text{bar}$ and a low temperature of $T_0 \sim 5 - 25\,\text{K}$ through a nozzle or an orifice into vacuum.[23] In the "subcritical" expansion, which is the usual mode, the initial state in the source is gaseous (cf. Fig 1.1 (2)). Expansion from the initially liquid state is called "supercritical" expansion (cf. Fig 1.1 (3)). Let us discuss the production of He droplets by free-jet expansion, their beam velocities, the He_N intensities and sizes, and **HE**lium **N**ano**D**roplet **I**solation spectroscopy (HENDI).

Free-jet expansion and He cluster growth

The structure of a free-jet expansion under continuum conditions has to be derived within the theory of thermodynamics.[23] Fig. 1.4 shows the characteristics of a free-jet expansion. A skimmer extracts the beam centerline. We will discuss the features

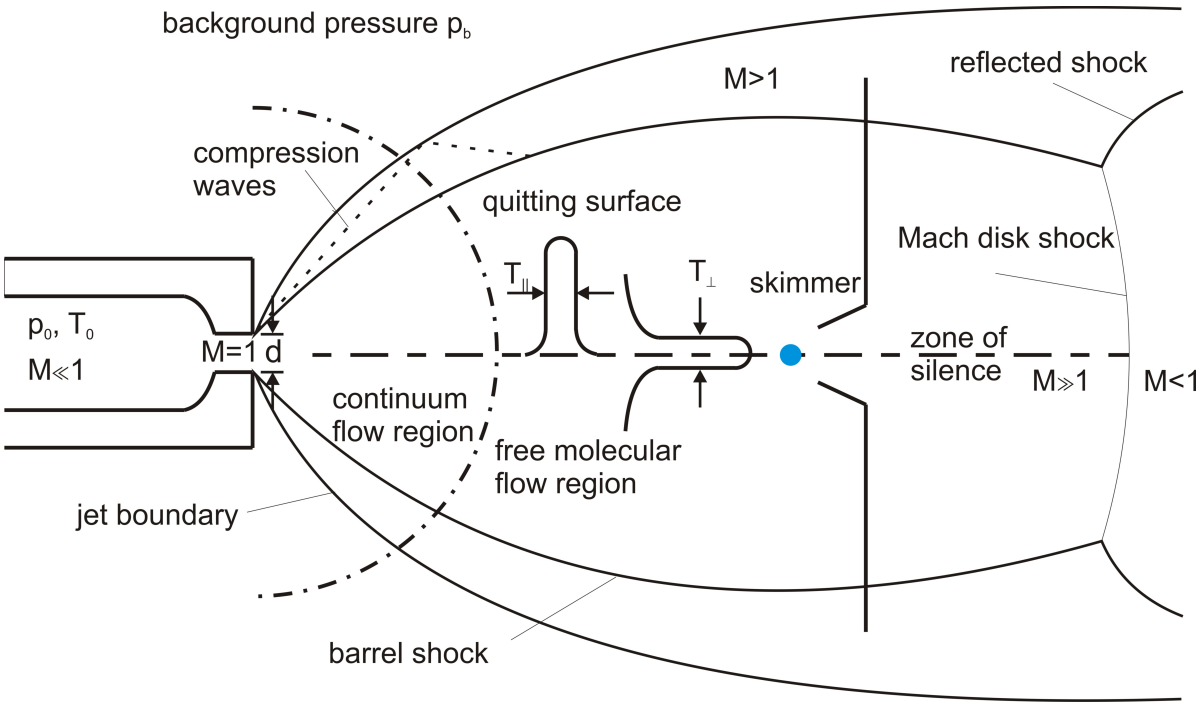

Figure 1.4.: Schematic of a supersonic free-jet expansion. Features are explained in the text.

qualitatively and accomplish this by giving equations of numerical calculations.

He gas is at rest in a reservoir with a stagnation pressure p_0 and a temperature T_0. The ambient pressure p_a outside the gas source is much smaller than p_0.[24] The He gas is accelerated and expanded through the nozzle, because of the significant pressure difference $p_0 - p_a$. The velocity at the orifice reaches sonic velocity ($M = 1$), if the pressure outside the nozzle p_a is low enough. For this the ratio p_0/p_a has to fulfill

$$\frac{p_0}{p_a} \geq G = \left(\frac{\gamma+1}{2}\right)^{\frac{\gamma}{\gamma-1}}, \tag{1.3}$$

with the adiabatic coefficient γ. G is for all gases < 2.1. If equation 1.3 is fulfilled the exit pressure of the beam becomes independent of p_a and is given by

$$p = p_0 \left(\frac{2}{\gamma+1}\right)^{\frac{\gamma}{\gamma-1}}, \tag{1.4}$$

which exceeds p_a in most cases. Consequently the He beam is further expanded toward the ambient pressure p_a. This goes along with expansion waves (cf. Fig. 1.4).[24] Compressing waves are produced by the reflection of the expansion waves at the free-jet boundary, which turn the free-jet boundary into beam direction. Also the flow becomes supersonic ($M > 1$), meaning that the flow is faster than the speed of sound, and M

increases with an increasing distance from the orifice ($M >> 1$).[23] The He gas expands isentropically and overexpands the boundary conditions (e.g. $p = p_a$). A recompression by shock waves takes place: the Mach disk normal to the beam centerline and the barrel shock at the sides (cf. Fig. 1.4).[24] The Mach disk is characterized by the change from $M >> 1$ to $M < 1$ (free molecular region). The distance between orifice and Mach disk location x_m itself was first characterized by Bier and Schmidt[25] and is given by

$$x_m/d = 0.67\sqrt{p_0/p_a} \tag{1.5}$$

with the diameter of the orifice d. The expansion is in its center region isentropic and independent of p_a, which explains the widely used term "zone of silence".[23]

Due to the high stagnation pressure p_0 the mean free path is small compared to the orifice diameter d (here $5\,\mu$m). In a free-jet expansion no external heat dissipation occurs (isentropic), so one has an adiabatic process. The particle density n decreases rapidly with the distance x from the orifice ($n(x) \propto \frac{d}{x}^2$), which leads to an adiabatic cooling of the expanding gas. The internal energy of the gas is mostly transferred into kinetic energy. Near the orifice the particle density is high enough for collisions, leading to a further temperature decrease. Looking at the phase diagram in Fig. 1.1 we see that the expansion follows an isentrope, which cuts the vapor pressure curve. At this point condensation starts and He droplets grow.[26] This continuous flow regime, where the clusters grow, ends slowly with a decreasing collision rate. The "quitting surface" at x_q separates this regime from the following collision-free region. Note, that the quitting surface is a region and not a well defined edge. According to Toennies[26] x_q can be estimated by $\sim 1000/d$. More exactly x_q can be calculated with[23]

$$x_q = d\left(\frac{S_{\parallel,\infty}}{3.232}\right)^{3/2}. \tag{1.6}$$

$S_{\parallel,\infty}$ is the terminal speed ratio and will be derived later, where the speed ratio is generally defined as $S = \frac{v}{\Delta v}$. The cluster is then further cooled by evaporative cooling of outer droplet atoms to a final temperature, which is $T \sim 370\,$mK for ^{4}He.[26] In Fig. 1.5 one can see the different regions: cluster growing and evaporative cooling.

Beam velocity and terminal speed ratio (following Ref. 23)
To determine the velocity of the droplet beam as well as the speed ratio S one has to consider the velocity distribution of the atoms in the He flow. The most used distribution model is a Maxwell distribution, where the velocity is separated into one in flow direction ($v_\parallel$) and one normal to it ($v_\perp$). As a consequence the temperatures have to be separated into $T_\parallel$ and $T_\perp$, too (cf. Fig. 1.4). The anisotropic Maxwell-distribution is given by

$$f(v) = n\left(\frac{m}{2\pi k_B T_\parallel}\right)^{1/2}\left(\frac{m}{2\pi k_B T_\perp}\right) \times \exp\left(-\frac{m}{2k_B T_\parallel}(v_\parallel - \bar{v}_\parallel)^2 - \frac{m}{2k_B T_\perp}v_\perp^2\right), \tag{1.7}$$

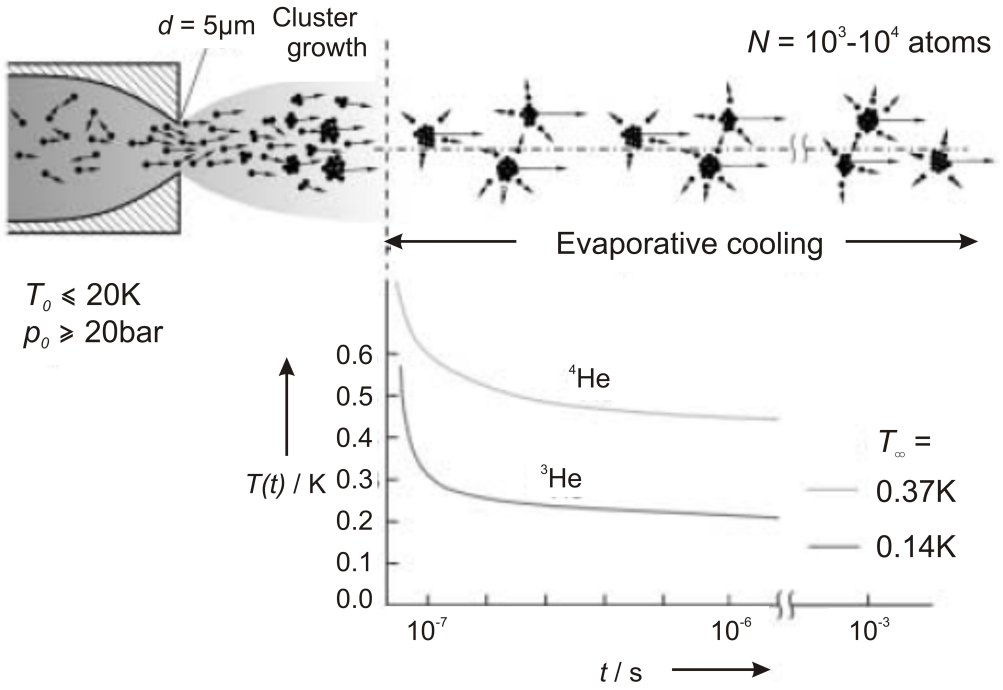

Figure 1.5.: Representative scheme describing the process of cluster formation and subsequent cooling. Subsequent cooling times were calculated in Refs. 27,28. Figure taken from Ref. 26 (modified).

with the mass m, Boltzmann's constant k_B, and the velocity v. The mean velocity in forward direction $\bar{v}_\parallel$ is then

$$\bar{v}_\parallel = \sqrt{\frac{2}{mk_BT_\parallel}} \tag{1.8}$$

and the end velocity $v_{\parallel,\infty}$ is given by

$$v_{\parallel,\infty} = \sqrt{\frac{2k_B}{m}\left(\frac{\gamma}{\gamma-1}\right)T_0}. \tag{1.9}$$

For noble gases ($\gamma = \frac{5}{3}$) it follows

$$v_{\parallel,\infty} = \sqrt{\frac{5k_B}{m}T_0}. \tag{1.10}$$

In supersonic free-jet expansion the velocity distribution becomes narrower, which is expressed by a decreasing temperature. The speed ratios of both $S_\parallel$ and $S_\perp$ behave equally in the continuum flow region. At the quitting surface, when the flow goes over into a molecular flow region, the collision rate decreases. As a consequence the speed

ratio in forward direction does not change anymore and is called terminal speed ratio [23]

$$S_{\parallel,\infty} = A \left[\sqrt{2}\, n_0\, d \left(\frac{53\, C_6}{k_B T_0} \right)^{1/3} \right]^B , \tag{1.11}$$

with the particle density for He $n_0 = 3.22 \times 10^{16} \times p_0 \frac{300}{T_0}$ (p_0 in Torr), the orifice diameter d in cm, $A = 0.527$, $B = 0.545$, and the Leonard-Jones potential parameter $C_6 = 2.1252 \times 10^{-67}\,\mathrm{J/cm^6}$.[23] A more convenient expression with the stagnation pressure p_0 in bar can be derived

$$S_{\parallel,\infty} = A \left[\frac{\sqrt{2}\, p_0\, d}{1000\, k_B\, T_0} \left(\frac{53\, C_6}{k_B T_0} \right)^{1/3} \right]^B . \tag{1.12}$$

The terminal Mach number, which is an often used number, is then given by

$$M_{\parallel,\infty} = \sqrt{2/\gamma}\, S_{\parallel,\infty}. \tag{1.13}$$

In general, a supersonic beam has two specific characteristics: (i) a supersonic beam has increased velocity compared to an effusive beam, (ii) the longitudinal speed ratio $\frac{v}{\Delta v}$ increases.

He_N sizes and intensities

The average He number size of He nanodroplets, which depends on source temperature and stagnation pressure, is shown in Fig. 1.6 for the case of a 5 μm nozzle. One can see that the average number $\bar{N}$ of He atoms varies between several hundred and $\sim 2 \times 10^4$ He atoms, when the droplets are produced in the subcritical expansion mode.[26]

In our experiments it turned out that the size distribution of He_N is of importance, so that we will give here examples and derive an approximation for the total He_N flow. In Ref. 29 the size distribution of He_N was determined for several nozzle temperatures and stagnation pressures. In the subcritical mode (Fig. 1.1, point 2) this follows a log-normal distribution with a width comparable to their mean size

$$P(N) = \frac{1}{\sqrt{2\pi} N \delta} e^{-\frac{(ln N - \mu)^2}{2\delta^2}}, \tag{1.14}$$

μ and δ, are the mean and standard deviation, respectively, of the variable's natural logarithm. In the supercritical regime (lower temperatures) the clusters are formed by the fragmentation of liquid He and are very large consisting of $\sim 2 \times 10^5 - 10^7$ He atoms (Fig. 1.1, point 3). Because of the different formation processes, they follow a linear-exponential distribution.[30] Also even larger droplets can be produced by a Rayleigh break-up. The number of He droplets, which are formed and arrive at the detection

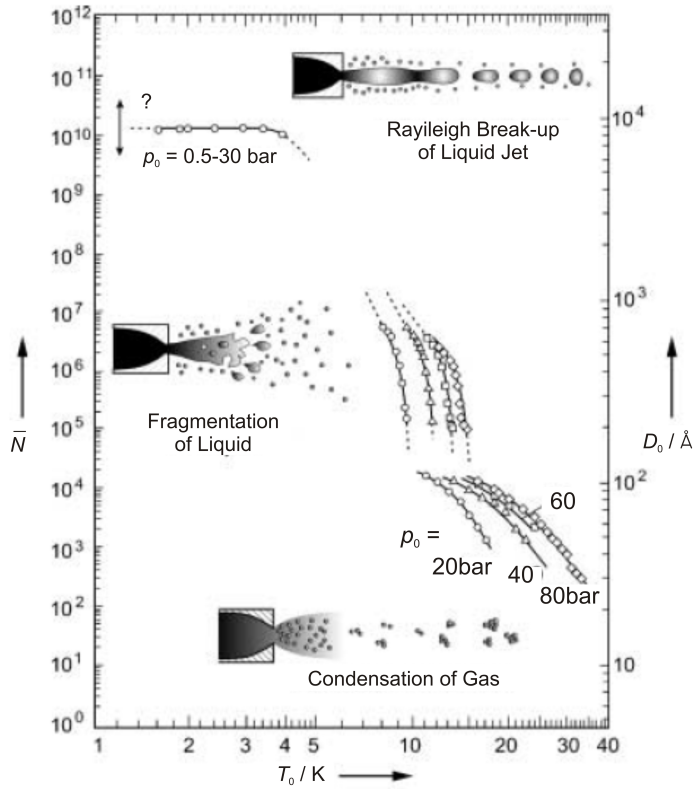

Figure 1.6.: Mean droplet size $\bar{N}$ and diameters D_0 of ^{4}He nanodroplets in different modes of jet operation. Features of the different operation modes are described in the text. Figure taken from Ref. 26 (modified).

area, can be estimated as follows. The total mass flow $\dot{m}$ in g/s of a subsonic expansion is independent of the background pressure p_0 and can be estimated with[23,24]

$$\dot{m} = p_0\, a \sqrt{\frac{\gamma W}{RT_0}\left(\frac{2}{\gamma+1}\right)^{(\gamma+1)/(\gamma-1)}}\,. \tag{1.15}$$

W is the molar mass of He ($\sim 4\,\mathrm{g/mol}$), $a = \pi(d^2)/4$ is the area of the orifice, and $R = 8.314\,\mathrm{J/molK}$ is the gas constant. According to Pauly[24] the centerline intensity in forward direction ($y = 0$) of the beam is given by

$$I(y=0) = \frac{2}{\pi}\dot{m}. \tag{1.16}$$

The intensity is decreased by the presence of the skimmer and the distance between orifice and detector to[23]

$$I = I(y=0) \times \left[1 - \exp\left(-S^2_{\parallel,\infty}(\frac{r}{x_q})^2(\frac{x_d}{x_d - x_s})^2\right)\right]. \tag{1.17}$$

With our conditions this can be estimated as $I \sim I(y = 0)$, because $S_{\parallel,\infty} > 100$. For the conversion from the beam intensity given in g/s to He atoms per second one has to divide the intensity by the molar mass W of He and multiply it with the Avogadro constant $N_A = 6.02214179 \times 10^{23}\,\mathrm{mol}^{-1}$:

$$I[\mathrm{He\,atoms\,sr^{-1}\,s^{-1}}] = \frac{N_A}{W} I[\mathrm{g\,sr^{-1}\,s^{-1}}]. \tag{1.18}$$

Until now we have calculated the number of He atoms per second. With a simple division by the mean droplet size to obtain the number of He droplets in the detector area, one would neglect the formation process of the droplets and assumes that all He atoms in the beam are transformed into droplets. But the droplets start the evaporative cooling process leading to the final temperature of 370 mK at a specific temperature, which depends on the source conditions.[6] The amount of energy, which one He atom takes away when evaporating, before reaching the final temperature is not clear. Only when a temperature of 370 mK is reached, the evaporation of one He atom from the droplet corresponds to an energy release of 7 K.[26] Roughly the number of He atoms, which have to be evaporated, to cool the droplet from the liquid-vapor line down to 370 mK will be of the same magnitude as the surviving He atoms for our source conditions. Therefore the intensity of the beam has to be reduced by this amount:

$$I_{final} \sim \frac{I}{2}. \tag{1.19}$$

Let us assume a stagnation pressure of 20 bar and a nozzle temperature of $T_0 = 9.8$ K. This leads to $\dot{m} \sim 0.2{\times}10^{-3}$ g/s, $I = 0.127{\times}10^{-3}\,\mathrm{g\,sr^{-1}\,s^{-1}} \equiv 1.9{\times}10^{19}\,\mathrm{He\,atoms\,sr^{-1}\,s^{-1}}$, and $I_{final} \sim 0.95 \times 10^{19}\,\mathrm{He\,atoms\,sr^{-1}\,s^{-1}}$. This corresponds to a droplet fluence of $1.9 \times 10^{15}\,\mathrm{droplets\,sr^{-1}\,s^{-1}}$ with an estimated mean size of 5000 He atoms per droplet. This calculated number coincides with experimental data published in Ref. 31, where the fluence of He droplets has been derived from the fluence of transported molecules by a droplet beam.

The radial size of the He droplet is of importance, too. He_N is expected as spherical in the ground state so that its radius can be estimated easily with the equilibrium distance between single He atoms

$$R = r_0 N^{1/3}, \tag{1.20}$$

where r_0 is the unit radius for the rare gas and N is the number of atoms in the cluster. For ^{4}He this is $r_0 = 2.22$ Å.[32]

He nanodroplet isolation spectroscopy (HENDI)

He nanodroplets are widely used as powerful tool to isolate small compounds and observe their properties in an ultracold environment. A whole special issue of the Journal of

Chemical Physics is dedicated to this topic: J. Chem. Phys. **115**, 22 (2001). Since then several review articles (cf. Ref. 6,26,33–35) have been published concentrating on He droplets and its applications. We want to name some of them. Chemical reactions[36–38] on an atomic scale in a low-temperature environment have been monitored. Also the formation of high-spin alkali-metal clusters has been observed for the first time.[39] In recent experiments large protein ions were trapped in a He_N consisting of $\bar{N} \sim 10^{10} - 10^{12}$ He atoms.[40] The main advantage of HENDI over other matrix isolation methods is the low interaction between dopant and superfluid He[26], so that one can use the droplet as a cooling agent without having a strong influence on the dopant and often speaks of a *nanocryostat*.

The droplets can be easily doped with molecules (or atoms) by passing through vapor of the dopant. The vapor can be created with several techniques. A pick-up cell filled with a solid can be heated (sublimation), which is simple if the needed vapor pressure can be reached with temperatures below $\sim 500\,^{\circ}\mathrm{C}$. Laser ablation[41] as well as electron bombardment[42] are used for high temperature evaporation, too. For liquid or gaseous molecules a gas pick-up is favorable, where the molecules are carried into the pick-up region already in gaseous form. For the experiments described in this thesis only a heated pick-up cell filled with the dopant was used. This doping method was introduced by Scoles and co-workers for a different type of noble-gas clusters[43] and was adapted later by Toennies *et al.* for He droplets.[44]

One can imagine the nanodroplet as a ballistic bullet, which collides with atoms or molecules on its flight way. The pick-up cross-section is close to the size of the droplet, so that a vapor pressure of $\sim 10^{-5}\,\mathrm{mbar}$ is enough for picking up single particles. The pick-up itself leads to a decrease of the droplets' size. The kinetic and the internal energy of the impacting particle as well as chemical potentials are transferred to the nanodroplet. Subsequently He atoms evaporate and the droplet shrinks in size. For ^4He_N an excess energy of $\sim 5\,\mathrm{cm}^{-1}$ corresponds to the evaporation of one He atom.[26] Usually every pick-up of an atom evaporates several hundred He atoms.[45] In chapter 7 the pick-up of Ak atoms and the subsequent formation of large Ak clusters on He droplets is described. Here, the energy release of Ak clusters in different spin states can be compared with the proposed shrinking size of the droplet and its initial size. The number of particles picked-up follows a Poisson distribution

$$P_k(z) = \frac{z^k}{k!}\mathrm{e}^{-z} \tag{1.21}$$

with the number of particles k and the average number of collisions z as given in Ref. 46, which is slightly modified in the case of surface-located dopants like alkali-metal atoms.[30,47]

Most dopants immerse into the droplet. There are only some exceptions, which reside on the surface and form a dimple. In general these are heliophobic particles as ^{3}He[48], alkali-metal atoms[49] and their small clusters[50]. Alkaline earth-metals are a marginal case.[51] Ancilotto and co-workers[52] introduced a dimensionless parameter, which proposes the solvation of a dopant in the droplet

$$\lambda = \frac{\rho \epsilon R_m}{2^{1/6}\sigma}. \tag{1.22}$$

σ is the surface tension, ρ is the number density, ϵ is the well depth of a dopant-He pair potential, and R_m is the equilibrium distance. Dopants with $\lambda < 1.9$ reside on the surface. Molecules with values > 1.9 immerse.[26] In general, the attractive interaction between the impurity and the He atoms has to be stronger than between ^{4}He-^{4}He that the particle immerses.

The temperature of He droplets has been determined by the observation of rotational spectra of OCS molecules embedded in He droplets. As the line intensities follow a Boltzmann distribution the temperatures of the He droplets could be derived to $T \sim 370\,\mathrm{mK}$ (^{4}He) and $T \sim 150\,\mathrm{mK}$ (^{3}He).[53,54]

1.3. Motivation

This work is mainly motivated by fundamental research interests. He nanodroplets provide the unique possibility to study atoms or molecules at low temperature ($\sim 370\,\mathrm{mK}$) in a superfluid environment. The interaction between excited alkali-metal (Ak) atoms and superfluid helium has found tremendous interest in the past. Takahashi *et al.* examined D_1- and D_2-line fluorescence spectra of Rb and Cs in superfluid He and explained their results in terms of the spherical bubble model.[55] Alkali-metal atoms on He nanodroplets have been studied in various experiments (cf. Refs. 39,49,56–58), where it turned out that the Ak atom in its electronic ground state ($n^2S_{1/2}$) resides in a dimple on the surface of the droplet. Due to the surface location of the Ak atom the system can be described with a pseudo-diatomic model, where one atom is the He_N and the other is the Ak atom. Usually, the Ak atom leaves the surface of the He nanodroplet when electronically excited due to the strong Pauli repulsion between electron and helium. Until now, the only known exception for this are the $5^2P_{1/2}$ state of Rb[59,60] and Cs.[4] For several reasons the examination of higher electronic states and of the ionization of single Ak atoms has been neglected so far. At the beginning of this work only excitations of Ak atoms to their $(n+1)^2$P (K, Rb, Cs) and n^2D (Rb only) states were known to us, which have been reported meanwhile.[61]

On the other end of the energy scale, positively charged ions strongly attract helium, which has been predicted in theoretical calculations (cf. Refs. 62–69) and found in experimental works (cf. Refs. 70–72). Highly excited Rydberg states could close the gap between low excited states, desorbing from the nanodroplet, and positively charged alkali-metal ions, which have been investigated in this work, too. As the mean distance between alkali-metal core and valence electron can exceed the nanodroplet size, the repulsive part of the pseudo-diatomic potential, where the He nanodroplet is treated as a fictitious atom, should change dramatically. A situation could occur, where the Ak^+ core immerses and the electron surrounds the whole He nanodroplet. In this case one could speak of an artificial supersized atom. Also, a perturbation of the Ak atom induced by the presence of the He droplet should have an influence on the ionization threshold of the Ak atom and may lower this.

In addition, electrostriction is of general interest in various scientific fields. The strong attractive forces between positively charged alkali-metal ions and He atoms lead to solid-like structures. A first solid-like shell of He atoms surrounds the Ak^+ ion. For several Ak^+ ions a second layer, most probably bubble-like, can be identified in theory.[65] The experimental examination of this effect can be probed by ionization experiments of He nanodroplets loaded with Ak.

Furthermore, in modern material science the design of nanoscaled materials is of huge interest, as they can combine well understood properties of single atoms with those of bulk material. The observation of small cluster formation can help to fill the knowledge gap between single atoms and bulk material. Especially alkali-metal clusters are worthwhile to be observed as the bonding character of high- and low-spin Ak_n differs strongly with large magnetic moments in the first case[73] and delocalization of valence electrons in the second[74] In contradiction to other experimental techniques, the formation process of alkali-metal clusters on He nanodroplets favors the formation of such clusters in their high-spin configuration. Nevertheless also the creation of low-spin clusters is possible.

In this work we try to illuminate these aspects using HENDI.

2. Experimental

This chapter provides a description of our experimental setup, which includes the vacuum setup (Section 2.1). Specifications of the measurement equipment and the theoretical background of the analyzing methods are given and explained (Section 2.2). These are laser-induced fluorescence (LIF) measurements, dispersed emission spectroscopy, beam depletion (BD) spectroscopy with a Langmuir-Taylor detector, ZEro Kinetic Energy (ZEKE) electron spectroscopy, mass spectrometry with a time-of-flight (TOF) mass spectrometer and a quadrupol mass spectrometer (QMS). After first fruitless ionization experiments of Rb on He nanodroplets the equipment for ZEKE spectroscopy has been self-developed and the one for TOF has been set up. Therefore both are described in more detail.

2.1. Vacuum system

Figure 2.1 provides a schematic setup of the vacuum chamber including the different detectors. The used vacuum system consists of two separately evacuated chambers: the source and the detector chamber. Both chambers are connected to each other with a bypass, to avoid contamination of the detector chamber when not measuring. In the source chamber the He nanodroplet beam is produced.

The source chamber is pumped by an oil diffusion pump (Leybold DI6000/10B) with a pump rate of $\sim 6000\,\mathrm{l/s}$ and an operating range of $10^{-2} - 10^{-7}\,\mathrm{torr}$, which is provided by mechanical rough pumps (Edwards EH 1200, Edwards E2M80). The high pump rate assures a low pressure in the source chamber as the nozzle pressure is high. We already described the production of He nanodroplets in chapter 1.2. Therefore we only want to give here typical conditions of nozzle temperature T_0 and nozzle pressure p_0 together with cluster sizes for the different experiments (cf. Tab. 2.1). Between source chamber and measurement chamber is a skimmer with a diameter of $400\,\mu\mathrm{m}$ so that only the centerline beam enters the detector chamber. This reduces the background He pressure in the detector chamber significantly.

The measurement chamber is separated into two parts: the pick-up area and the detec-

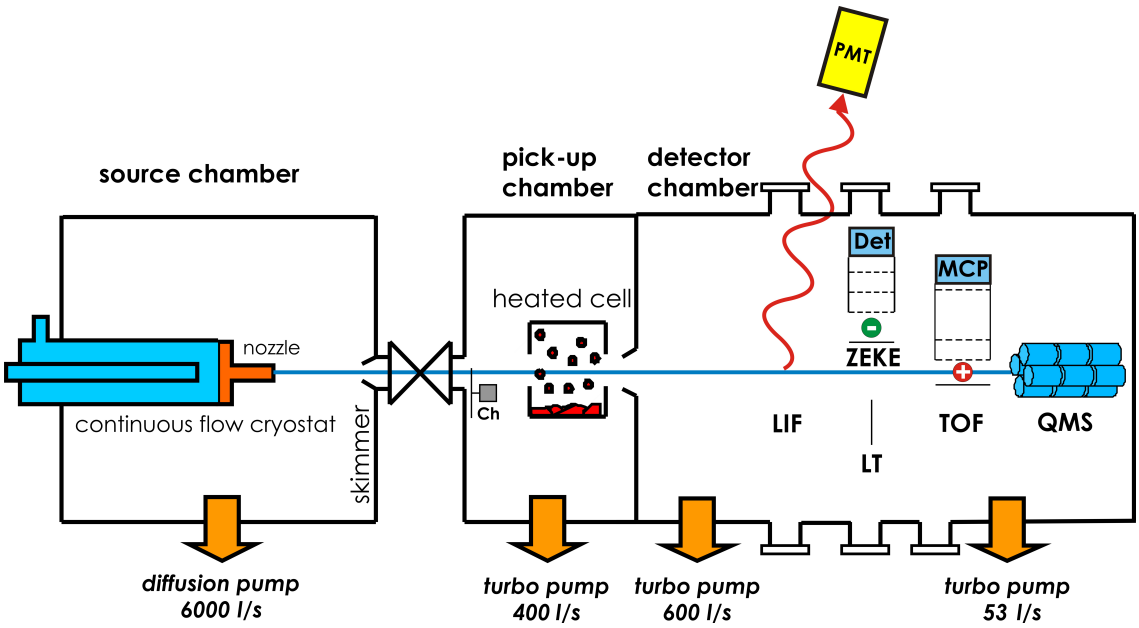

Figure 2.1.: Schematic of the experimental setup (Ch: chopper, LIF: laser-induced fluorescence, PMT: photomultiplier tube, LT: Langmuir-Taylor detector, ZEKE: zero kinetic energy electrons, Det: channeltron detector, TOF: time-of-flight, MCP: multichannel plate, QMS: quadrupole mass spectrometer). The PMT can be replaced by a grating spectrograph with a CCD camera. The apparatus for ZEKE spectroscopy can be replaced with the LT.

tion area. In the pick-up area the nanodroplet beam is doped with atoms or molecules. The detection area is used for all kinds of analyzing methods. The detector chamber is pumped by three separate turbo pumps. The first one (Alcatel TMP 5400: pump rate of $\sim 400\,\mathrm{l/s}$, fore pump: Leybold Trivac D10BHV) is situated in the pick-up area. The second one (Leybold Turbovac 600C: $\sim 600\,\mathrm{l/s}$, fore pump: Leybold Trivac D16B) is placed in the detection area. The last one sits next to the drift zone of the time-off-flight apparatus (Pfeiffer Vacuum TMU 064: $\sim 53\,\mathrm{l/s}$, fore pump: Varian 949-9452). The first element of the pick-up area is a chopper, to select between signals with and without cluster beam. The pick-up area then consists of two separate stainless steel pick-up cells, which can both be heated separately to set up the wanted vapor pressure of the dopant molecules (only one shown in Fig. 2.1). This allows to steer the ratio of nanodroplets doped with monomers, dimers, trimers etc. The entrance and exit holes for the nanodroplet beam have both a diameter of 5 mm. Between pick-up area and detection area is another hole with a diameter of 5 mm to avoid dirt in the detection area.

Table 2.1.: Typical conditions of nozzle temperature T_0, nozzle pressure p_0, and mean droplet sizes $\bar{N}$ for the different experiments. RS means Rydberg states.

chapter	main experiment	T_0 /K	p_0 /bar	$\bar{N}$
3	Two-step excitation of Rb	14.0	60	15×10^3
4	Ionization of single Rb atoms	9.0-15.0	30	$> 10^5 - 5 \times 10^3$
5	Cs on He_N	12.0-17.0	40	$15 - 3.1 \times 10^3$
6	ionization threshold	13.5-18.0	40	$13 - 4.7 \times 10^3$
	and RS lifetime	14.0-20.0	60	$15 - 4.7 \times 10^3$
7	Ionization Rb and Cs clusters	11.5-15.5	40	$21 - 8.4 \times 10^3$

2.2. Detection

The determination of the ionization threshold of alkali-metal atoms on He nanodroplets by monitoring Rb^+ (Cs^+) ions did not work using a self-built detector. In these experiments Rb has been ionized in an one-photon ionization scheme and the Rb^+-ions have been detected using a channeltron. We could not distinguish the ion current with and without the presence of a He nanodroplet beam. Moreover, as we will see later the Ak^+ immerses into the droplet and cannot be detected directly anymore. The experimental setup as well as our results of these experiments are described in great detail in the diploma thesis of F. Lackner (Ref. 75). To overcome the low resolution and the influence of parasitic molecules (e.g. ionized pump oil) in our setup we set up a commercial time-of-flight mass spectrometer (Jordan D-850 AREF) and developed a detector for *ZE*ro *K*inetic *E*energy (ZEKE) spectroscopy.

Several different measurement techniques with different detectors, placed in series along the He nanodroplet beam axis, can be used:

(1) Absorption spectra: laser-induced fluorescence (LIF) spectra are measured in the interaction zone between laser and He_N beam by recording the fluorescence light emitted from an excited state with a Peltier-cooled photomultiplier tube (PMT, housing: Product for Research, TE210TS-RF; tube: Hamamatsu R943-01 with GaAs photocathode). In general, atoms or molecules are excited by a laser from a given state to an excited state. Fluorescence light is emitted by the decay of this state and can be collected. A lens system built by others is used before the light enters the detector to maximize the efficiency. Details of this detector can be found in the diploma thesis of J. Nagl (cf. Ref. 76).

(2) Emission spectra: a grating spectrograph (McPherson EU-700) in combination with a CCD-camera (LOT-Andor iDUS DU401A BR-DD) is used to monitor fluorescence spectra of Cs monomers upon excitation. The dispersed fluorescence spectra can be monitored by exchanging the photomultiplier tube with the grating spectrograph. The disadvantage of the combination is the extremely low sensitivity. In other words, the combination only worked well, if (i) the absorption probability is rather high and/or (ii) the emitted fluorescence light (different decay channels) is rather intensive (e.g. D-lines of the alkali-metals).

(3) Beam depletion (BD) spectra: a Langmuir-Tailor surface ionization detector is used for measuring the amount of Ak atoms transported by the He nanodroplet beam [77]. Ak atoms are usually spontaneously ionized upon hitting a hot metallic filament with a high work function (e.g. rhenium). The arising ions can be measured as charge flow, which directly reflects the transported Ak atoms. The ion signal decreases due to the desorption of Ak atoms, which usually happens by exciting Ak atoms into higher electronic states, because they are only weakly bound to the surface of He nanodroplets ($\sim 10\,\mathrm{cm}^{-1}$). The BD signals are recorded with a lock-in-amplifier (Stanford Research SR510) and the background coming from free Ak atoms is suppressed by chopping the droplet beam and performing phase-sensitive detection. [78] Details of this detector can be found in the diploma thesis of J. Nagl (cf. Ref. 76).

(4) *ZE*ro *K*inetic *E*nergy (ZEKE) spectroscopy: ZEKE spectroscopy is a high resolution spectroscopy for molecular ions, which has been invented by Müller-Dethlefs in 1984. [79] The basic principle is to excite electrons into Rydberg states, the potential of which is close to the ionization threshold, and to ionize and detect the electrons afterwards. We are also able to detect the positively charged ions, which will be described later.

We give an overview of ZEKE spectroscopy and explain the difference of ZEKE spectroscopy in comparison to photo-electron spectroscopy (PES). Afterwards we give the features of the self developed setup as well as the test experiments. Unfortunately there was no time during this PhD thesis to use this self-build apparatus for He_N related experiments.

If a photon exceeds the ionization potential of a molecule, normally a photoelectron is emitted and leaves a positively charged ion behind, whereby the focus of this chapter lies on the detection of the electron. In PES all electrons are detected, which are emitted by the photo-ionized molecules. Conclusions about the energy states are made either by the energy of the photoelectrons, if the photon energy is constant, or by the electron current, if the photon energy is variable.

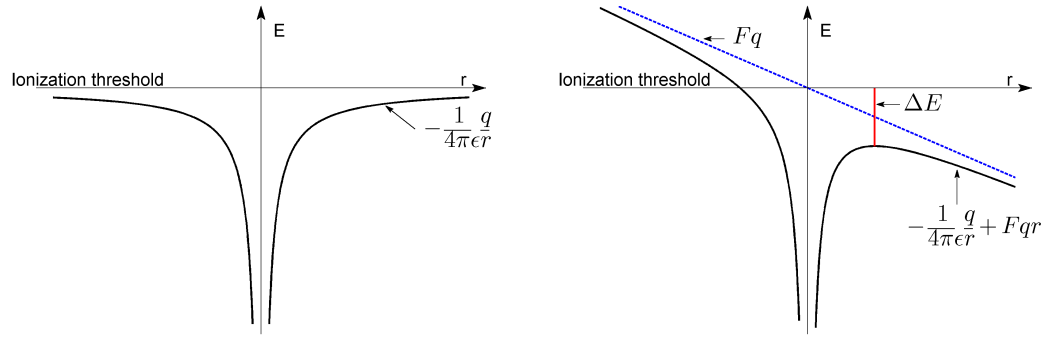

(a) (b)

Figure 2.2.: In (a) is the Coulomb potential of the H-atom shown. In (b) the Coulomb potential is modified by an additional electrical field F

To understand the principles of PES and ZEKE we assume a hydrogen atom, the potential of which is given by

$$\mathrm{V}(r) = -\frac{1}{4\pi\epsilon_0}\frac{q}{r} \tag{2.1}$$

where ϵ_0 is the dielectric permeability of vacuum, q is the charge and r is the distance between electron and ion (cf. Fig. 2.2(a)). In the case of an external electrical field with the strength F the potential is modified to

$$\mathrm{V}(r) = -\frac{1}{4\pi\epsilon_0}\frac{q}{r} + Fqr \tag{2.2}$$

which leads to a saddle point (cf. Fig. 2.2(b)). The energy difference between the saddle point and the ionization threshold provided by the Coulomb potential in eq. 2.1 can be derived by fundamental laws as

$$\Delta E = 6.1215\,\sqrt{F} \tag{2.3}$$

where F is given in V/cm.

We give some scaling properties of Rydberg atoms with the principal quantum number n in Tab. 2.2).

In the case of the hydrogen potential the energy states scale as

$$\Delta\mathrm{E}_n = -\frac{Ry}{n^2} \tag{2.4}$$

with $Ry = 109737\,\mathrm{cm}^{-1}$. High Rydberg states ($n > 100$) have several features. As their energy state is close to the ionization threshold ($\sim 10\,\mathrm{cm}^{-1}$) they are easily ionized by

Table 2.2.: Properties of Rydberg atoms and their dependence on the main quantum number n according to Refs. 80 and 81.

property	Rydberg states
binding energy	n^{-2}
energy between adjacent n states	n^{-3}
orbital radius	n^2
radiative lifetime	n^3 (n^5 for ZEKE states[81])

an external field.[82] Another feature of Rydberg states is their long radiative lifetime. In the case of ZEKE states, which have non-core penetrating character, the lifetime scales as n^5, while the lifetime usually scales as n^3.[83]

The lifetime of low orbital angular momentum Rydberg states, which are core penetrating, should be proportional to their electron density in the core region ($\propto n^{-3}$). Therefore the lifetime should scale as n^3, which is on the microsecond timescale. The enhancement of the lifetime beyond this scale of ZEKE states can be explained by a non-core penetrating character, which is acquired and comes from state l, m-state mixing mainly due to electric stray fields.[83,84]

The long lifetime can be used in ZEKE spectroscopy. In short, the electrons are either (i) excited to HR states, (ii) ionized just above the ionization threshold or (iii) ionized with higher energy. In the first two cases the electrons do not have a kinetic energy component in addition to their movement with the molecule, which explains the name ZEKE electrons. In the latter case the electron will receive most of the energy difference between the ionization threshold and the photon energy, which leads to a new velocity component of the electron. These electrons can be called non-ZEKE electrons. After photo-excitation or -ionization a pulsed electric field is applied to direct the electrons into a detector. If the time between excitation and pulsed field is long enough ($\sim 1\,\mu$s), the non-ZEKE electrons can be discriminated from ZEKE electrons. The non-ZEKE electrons will be separated spatially from the ZEKE-electrons. The separation depends on their velocity, which is equivalent to their kinetic energy, and the delay time between photo-excitation/-ionization and the pulsed field. Moreover, a pre-loaded field, which has to be small, can be used to direct the electrons of (ii) and (iii) into the repeller plate and eliminate them.

As can be seen by eq. 2.3 the applied field has to be strong enough to overcome the energy difference between HR state and ionization threshold. A schematic setup of

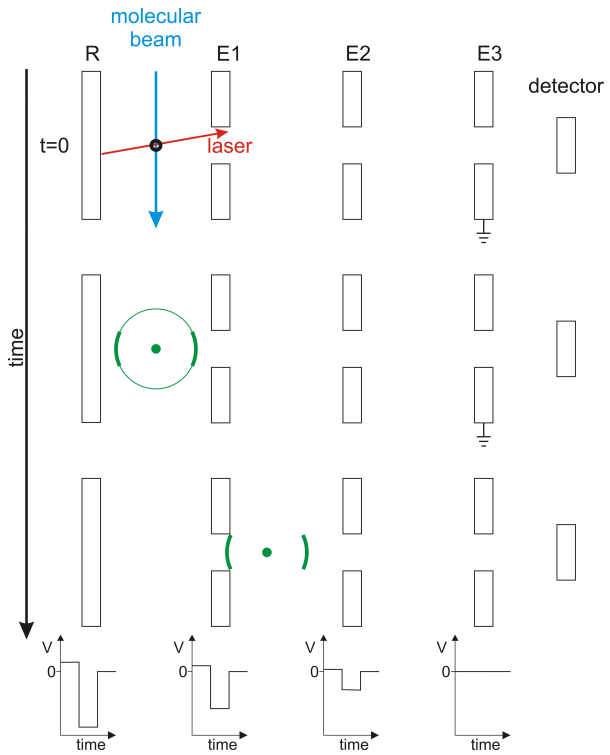

Figure 2.3.: Schematic representation of the ZEKE process. At $t = 0$ the laser beam generates ZEKE electrons as well as fast photoelectrons. The latter ones will have moved away from the ionization point after a suitable delay time. A pulsed field between repeller (R) and extraction plates (E1, E2, E3) will direct the ZEKE electrons and some of the fast photoelectrons to the detector, whereby the fast photoelectrons can be discriminated by the flight times as well as by a pre-loaded field.

ZEKE spectroscopy including the delayed pulsed electric field is shown in Fig. 2.3.

The ionization threshold can also be examined by varying the excitation energy and detecting the photoelectrons under field-free conditions, which will yield a step-wise ion production in the case of molecules. When reaching a new ionization threshold the ion production increases. By taking the derivative of the ion yield versus excitation energy a peak will occur at threshold energies (2.4). A ZEKE spectrum is therefore the derivative of an ion yield spectrum.[81]

The applied setup for ZEKE spectroscopy (Fig. 2.5) was constructed by ourselves, whereby one of the main difficulties was to include the setup into the given vacuum chamber and avoid the influence of other detectors and electric stray fields. In total, there are four electrical field plates: one repeller plate (R) and three extraction plates E1-E3. The plates are stacked, where the distance between all plates is the same (aper-

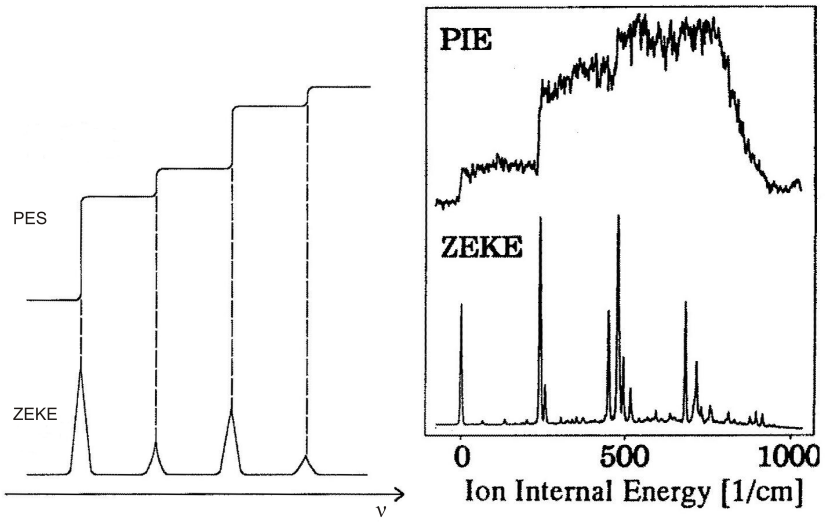

(a) PES spectrum vs. ZEKE spectrum

(b) phenol-water complex

Figure 2.4.: (a) A Simulated photoelectron spectrum (PES) is compared with its ZEKE spectrum. In (b) the photo-ionization efficiency (PIE) of the phenol-water complex is compared with the ZEKE spectrum. Figures taken from Ref. 81

ture diameter of plates E1-E3 7 mm, distance between plates 16 mm, stainless steel). The voltages applied to the plates are: R = U, E1 = $\frac{2}{3}U$, E2 = $\frac{1}{3}U$, E3 = 0, so that the electrical fields between the four plates are the same. The traveling way for the electrons is shielded by (i) the plates themselves (cf. Fig. 2.5) and (ii) μ-metal to reduce magnetic field effects, which influence the flight direction. In addition, the pulsed field source has been constructed.

The resolution ΔE is given by the field strength. Classically ΔE is the distance between the saddle point in Fig. 2.2(b) and the ionization threshold, which is $\Delta E = 6.1215\sqrt{F}$. When considering tunneling effects it turns to be

$$\Delta E = 4.6\sqrt{F} \tag{2.5}$$

where ΔE is given in cm^{-1} and F in V/cm.[85] For all estimations in ZEKE experiments as well as in TOF experiments we use the classical expression. For convenience the used voltages with the best signal and the achieved energy resolution for ZEKE experiments with our used setup are given: repeller voltage 12.3 V, resolution 9.8 cm^{-1}. In Fig. 2.6 the ZEKE signal of Rb atoms is shown.

(4) Time-of-flight mass spectrometry: mass spectrometry is a widely used tool to examine the mass-to-charge ratio (m/q) and abundance of ions. In time-of-flight (TOF) mass spectrometry (MS) this is done by monitoring the time between ion production

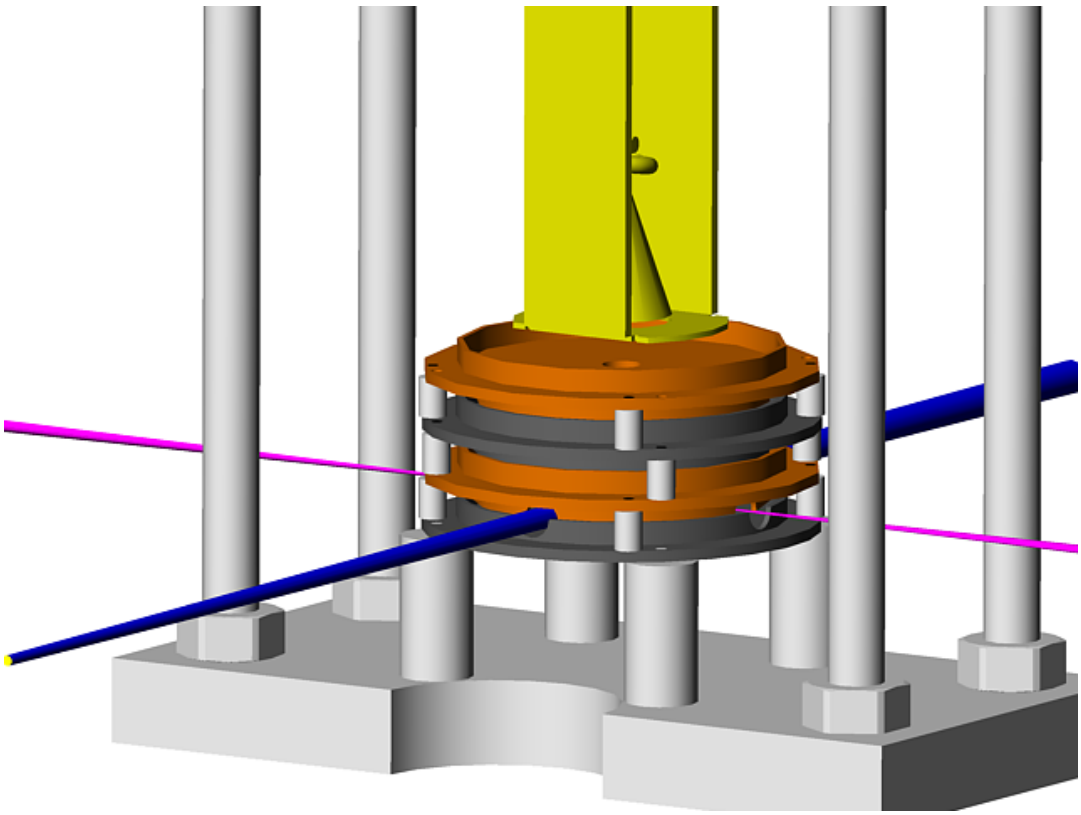

Figure 2.5.: AutoCAD drawing of the self-constructed ZEKE apparatus. The different plates (R, E1-E3) are colored dark gray and orange. A channeltron (yellow) serves as detector. The He droplet beam and the laser beam are indicated in blue and red, respectively.

and detection. TOF-MS is based on a fairly simple principle: from a measurement of the time required for an ion to travel a given distance the mass-to-charge ratio of the particle is determined.[24] In most cases positively charged ions are created from neutral molecules or atoms by a pulsed laser. These ions are then accelerated by an electrostatic field, which is usually applied between a repeller plate and an acceleration plate with a grid. After passing the grid the ions move in a field-free drift tube and are afterwards detected.[86] Several review articles (cf. Refs. 87–89) concentrate on TOF-MS. Here, we briefly explain the basics of this kind of mass spectrometry, where we use the same nomenclature as given in Refs. 88,90.

Let us assume that the ions with mass m and charge q are accelerated by an electrostatic field with the electrical field strength E_s in the ionization regime, from where they start at rest and from the same spatial plane (Fig. 2.7). After passing the first grid the

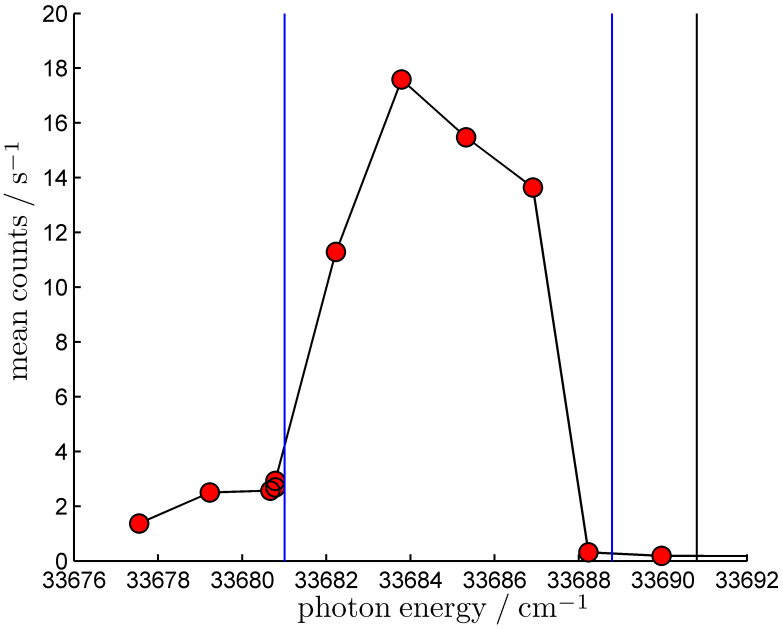

Figure 2.6.: ZEKE signal of Rb recorded with our setup. The connecting line is to guide the eye, only. Laser source is the frequency tripled pulsed Ti:Sapphire laser (one-photon ionization). The vertical black line shows the ionization threshold of Rb. The blue lines indicate the ionization regime with $\sim 300\,\mathrm{mV/cm}$ as pre-loaded field and $\sim 2.6\,\mathrm{V/cm}$ as pulsed field.

kinetic energy $U_{s,\mathrm{kin}}$ is then given by

$$qE_s = \frac{mu^2}{2} \tag{2.6}$$

so that the velocity u is inversely proportional to the square root of m/q. To increase the mass resolution a second field (E_d) is placed behind the first one (double-field source).[90] Then a field-free drift tube with length D is built in. If we assume uniform electric fields ($E_1 = U1 - U2$, $E_2 = U2 - 0$) we can calculate the time T, the ions need to reach the drift zone and to pass it[88,90] (as well as to hit afterwards the detector)

$$T = T_s + T_d + T_D + T_r \tag{2.7}$$

$$T_s = \sqrt{\frac{2s}{E_s}}\sqrt{\frac{m}{q}} \tag{2.8}$$

$$T_d = \sqrt{\frac{2s}{E_d}}\sqrt{\frac{m}{q}}\left(\sqrt{\frac{E_s + E_d}{E_d} - \frac{E_s}{E_d}}\right) \tag{2.9}$$

$$T_D = \frac{D}{u_D} = \frac{D}{\sqrt{2sE_s + 2dE_d}}\frac{m}{q} \tag{2.10}$$

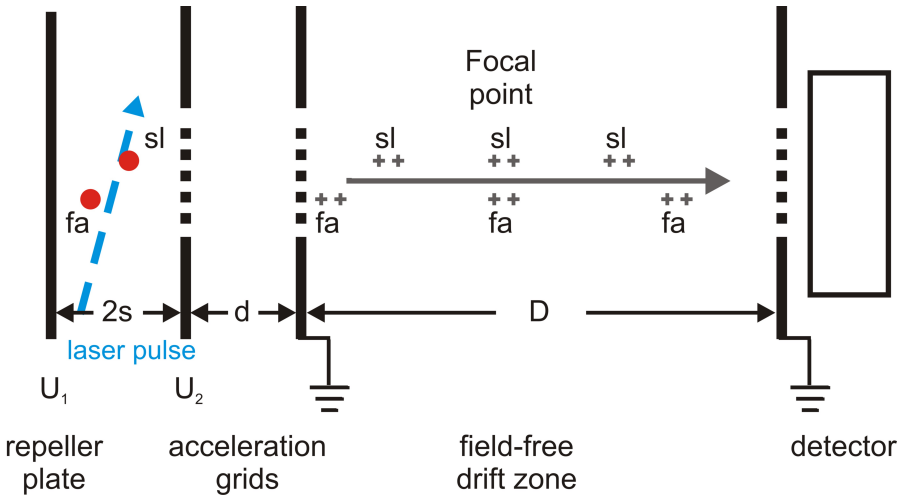

Figure 2.7.: Principle of TOF measurement: positively charged ions are created and are accelerated by two different electrostatic fields ($E_s = \frac{U_1 - U_2}{2s}$, $E_d = \frac{U_2}{d}$) into a field-free drift zone. By measuring the travel time one receives q/m. Due to different ionization points ions are accelerated longer (fa) or shorter (sl). The displayed setup is based on the one explained in Ref. 90.

where T_s and T_d are the accelerating times, T_D is the time in the drift zone with the constant velocity u_D, and T_r is the response time of the detecting system. By these equations we can see that the travel time is proportional to $\sqrt{m/q}$ and one can distinguish between different ion products:

$$m/q = c\,t^2 \tag{2.11}$$

with the calibration factor c (c can be determined experimentally from t with two known m/q-ratios).

The starting time is given either by a pulsed laser or a pulsed electric field. For our TOF apparatus (Jordan D-850 AREF) the detection works with a Multi-Channel Plate (MCP), where incoming ions are converted into voltage pulses. Afterwards they are amplified and detected by a fast counter (Stanford Research SR 400 or a homemade counter being able to handle differently timed ions at once without scanning time gates).

In order to increase the mass resolution this simple setup is further modified. There are several reasons, which have a negative influence on $\Delta m/m \propto \Delta t/t$: (i) the starting time depends on the pulse duration of the laser (here for both pulsed lasers $\sim 30\,\mathrm{ns}$) or of the build-up time of a pulsed electric field (here $\sim 20\,\mathrm{ns}$). As ions are produced during the whole time of the laser pulse, the starting time smears out and the resolution decreases. This effect can be compensated with a longer flight time. (ii) The starting velocity u_0 of the ions may differ, which can be neglected in our case due to the sharp ve-

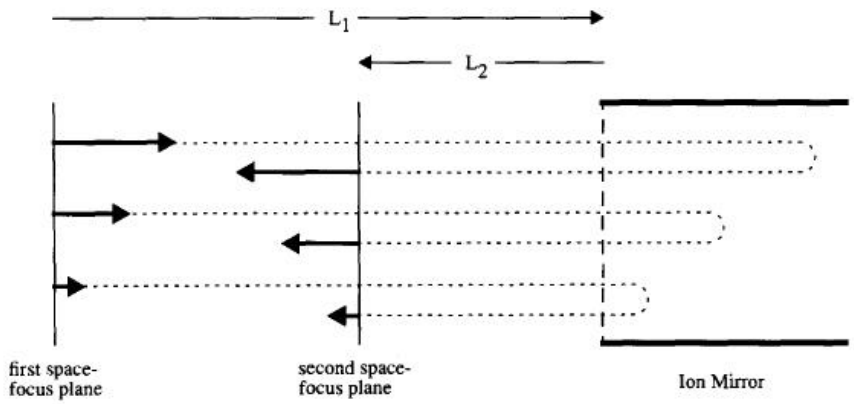

Figure 2.8.: Idealized representation of the one-dimensional ion mirror. The arrows represent the initial velocities of the individual ions. Figure taken from Ref. 92.

locity distribution of the He droplet beam.[6] (iii) The ions have different starting points, because the laser pulse has a spatial elongation. In relation to their starting positions the ions have different velocities after passing the grids.[90]

In general, there are two ways to increase the mass resolution: (a) a longer flight time reduces temporary effects, (b) ion optics focus the ions spatially.[91] Ions are accelerated by the potential differences ($U1-U2$, $U2-0$) and travel on with u_D in the drift region. If the ions are produced closer to the first acceleration grid (Fig. 2.7) they are shorter accelerated than ions produced further away leading to different kinetic energies. The faster ions (labeled with fa), which start further away from the acceleration grid, will get ahead of the slower ones (labeled with sl) at a certain focal point F. For a good mass (or energy) resolution the focal point should be at the point of the detector in a linear TOF apparatus. According to Wiley and McLaren[90] this can be calculated with a doubled field-source to

$$F = 2s_0 k_0^{3/2} \left(1 - \frac{1}{k_0^{3/2}} \frac{d}{s}\right) \tag{2.12}$$

with s_0 as average distance and $k_0 = \frac{s_0 E_s + dE_d}{s_o E_s}$.

With usual voltage settings the focal point in our TOF apparatus is not far away from the second grid ($\sim 13\,\mathrm{cm}$[75]), so that one wants to make the flight time independent of the ion's energy. The faster ions are sent on a detour as compared to the slower ones,[87] which can be done with a reflectron, where the ion beam is sent into an electrostatic repeller field.[93] The faster ions penetrate deeper into the field and receive the desired detour (cf. Fig. 2.8).

The potential in the repeller region can be chosen to generate a second focal point F_2,

leading to the condition that the flight time for all ions between the first focal point F and the second F_2 must then be identical and is given with[92]

$$t = L/u_z + \delta(u_z) = \frac{L}{u_z} + \frac{1}{\sqrt{2m}} \int_0^{z_f} \frac{dz'}{\sqrt{\frac{mu_z^2}{2} - eV(z')}}. \tag{2.13}$$

Note, that z defines here the direction, in which the electric fields are effective. The first term describes the flight time in the drift region starting from F and ending at F_2 (L is the mirror focal length $L = L_1 + L_2$); the second one describes the flight time difference in the repeller region for ions with the same mass-to-charge ratio and different kinetic energies. $V(z)$ is then the desired potential. z_f describes the turning point of the ions, which is given when the potential energy equals the kinetic energy. A solution for this equation is given in Ref. 92, too.

Our TOF apparatus (Jordan D-850 AREF) has been well characterized, where the results are described in the diploma thesis of F. Lackner.[75] For the reflectron mode the mass resolution was measured (K: $m/\Delta m = 280$, Rb: 500), which is large enough to distinguish between single alkali-metal ions and small ionized exciplexes (e.g. Rb-He, Rb-He_2). The main advantages of TOF-MS are that the ions arrive in a rapid sequence, that all ions arrive at the detector in contrast to QMS or sector-field mass analyzers, and that one needs only a short time for a complete mass spectrum.[87]

One goal in our group is to examine highly excited states of Ak atoms on He_N and their dynamics. Therefore it was necessary to install a good working detection mechanism, where we use a scheme similar to the detection of ZEKE electrons. Molecules (or atoms) are excited into an electronic state close to the ionization threshold under field-free conditions. The excited molecules are then ionized by a pulsed electrical field, which is delayed with respect to the laser pulse. The mass resolution itself is limited to the one of TOF spectroscopy using a constant field. Mostly the resolution is slightly altered due to the turn-on procedure of the field (here $\sim 20\,\mathrm{ns}$), which is not instantaneous. In our experiments the mass resolution was high enough to distinguish between Ak^+ and Ak^+-He. The energy resolution of this technique itself is the same as in ZEKE experiments.

The turn-on of the electric field was solved in the following way. Repeller plate and extraction grid have the same voltage (V1), which is similar to field-free conditions, when the pulsed laser is active. After a typical delay time of $\sim 1\,\mu\mathrm{s}$ the repeller plate voltage is increased to V2, so that the excited states are ionized (cf. Fig. 2.9). The used voltages are the same as in static electrical field experiments.

The setup was tested on bare Rb with the frequency tripled Ti:Sapphire pulsed laser (Coherent Indigo-S). The linewidth of the laser is $\sim 0.75\,\mathrm{cm}^{-1}$, so that Rydberg states lying closer together cannot be resolved anymore (cf. Fig. 2.10). One can further see

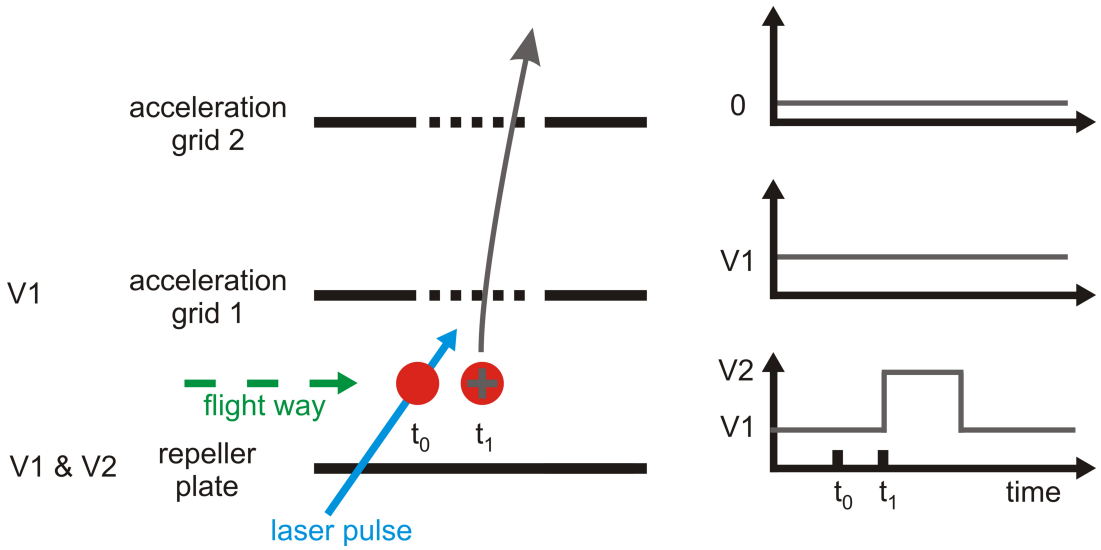

Figure 2.9.: Schematic of the used principle. First, the laser excites the molecule into a Rydberg state close to the ionization threshold at time t_0). Within the lifetime of this state an external field is switched on, which ionizes the molecule and directs the ion into the detector (t_1). Here, the voltages between repeller plate and acceleration grid 1 are set to the same voltage V1. By increasing the voltage of the repeller plate to V2 the electrical field is generated.

that the lifetime of the 38^2P state must be much longer than 1.65 μs, because the signal at Rb masses (85 amu, 87 amu) does not decrease by varying the delay time. This is in good agreement with given lifetimes for Rydberg states.[94]

(5) quadrupol mass spectrometry (QMS): quadrupole mass spectrometers are used to detect ionized particles according to their mass-to-charge ratio m/q. In general, the particles are (i) ionized, (ii) pass an analyzer, where they are separated according to their mass-to-charge ratio, (iii) and are subsequently detected. Here, we used an Extrel C50 QMS with a mass resolution being able to distinguish between neighboring m/q-ratios and limited to $m/q < 500$ amu. The QMS here serves mainly for optimizing the direction of the He nanodroplet beam by observing the signal at 8 amu (He_2). In addition, it can be used to monitor the ratio of doped monomers, dimers and trimers in the case of Rb- and Cs-doped He nanodroplets, so that the temperature can be optimized. Also absorption spectra can be monitored with a depletion technique.[95,96] Another application is to monitor the quality of our vacuum.

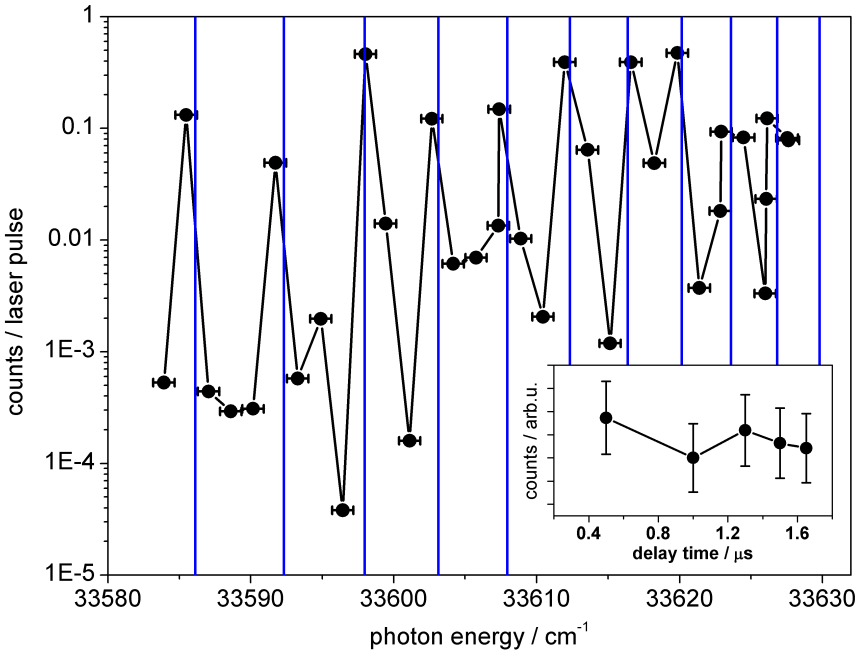

Figure 2.10.: Absorption spectrum of bare Rb monitored by the excitation of Rb atoms into a n^2P-state with a laser pulse (pulse fluence $\sim 0.7\,\mathrm{mJ/cm^2}$, linewidth $\sim 0.75\,\mathrm{cm^{-1}}$) and applying a pulsed electrical field of $430\,\mathrm{V/cm}$ with a delay of $1.65\,\mu\mathrm{s}$. The black dots show the signals per laser pulse, where the connecting line is only to guide the eye. The vertical blue lines indicate the n^2P-states ($n = 35-45$). Note the logarithmic scale. Inset: The graph shows the signal at different delay times of the electrical field recorded at $33602.67\,\mathrm{cm^{-1}}$, which is close to the 38^2P state. Error bars are calculated as standard deviation.

3. Two-step excitation of Rb atoms on He droplets

In this chapter we present the results of the first two-step excitations of single alkali-metal (Ak) doped He nanodroplets. Rubidium atoms in their $5^2S_{1/2}$ ($^2\Sigma_{1/2}$) electronic ground state reside on the surface of the droplet, where they tend to form a dimple.[57] If an Ak atom is excited into higher electronic states, it usually desorbs from there. For Rb this is not the case, when the atom is excited with photon energies close to the D_1-line of the bare Rb atom.[60] The Rb atom can still reside on the surface of the nanodroplet in its $5^2P_{1/2}$ ($^2\Pi_{1/2}$) state and decays from there into its ground state.[60] We use the $5^2P_{1/2}$ ($^2\Pi_{1/2}$) state as an intermediate state for a two-step excitation scheme, where the Rb atom is excited by a cw laser into the intermediate state, from where it is further excited. As detection serves the fluorescence light coming from one of the upper states. Here, the first two-step excitation of alkali-metal doped helium nanodroplets is presented, namely $5^2D \leftarrow 5^2P_{1/2} \leftarrow 5^2S_{1/2}$. Whenever the alkali-metal atom is excited into the intermediate state it stays bound to the helium droplets surface. In addition, results of theoretical calculations for Rb-He_N are presented. Most of the results in this chapter have been published in Eur. Phys. J. D ***61*** *(2011) 403-408 (Ref. 1).*

3.1. Introduction

Helium nanodroplets (He_N) are an ideal substrate to isolate atoms or molecules for spectroscopic investigations.[26] Alkali-metal (Ak) atoms, such as rubidium studied here, are an excellent probe to examine basic principles of this kind of matrix spectroscopy, because of a simple, easily accessible visible spectrum.[57,59] In comparison to other atoms, their Rydberg states and the ionization limit are at low-energy, thus easily reachable, and the associated transition probabilities are reasonably high.

Usually an alkali-metal atom photo-detaches from the surface of the He nanodroplet upon electronic excitation; the Rb D_1-line is an exception in that the atom almost always remains on He_N and relaxes back into the $5^2S_{1/2}$ state.[60] This has been exploited

to achieve repeated excitations, and optical pumping.[60] Here we demonstrate that this also allows sequential excitation of Ak-doped He_N, which, on the one hand can help to reach high-lying ^{2}S- and ^{2}D-states, on the other hand can give insight into the dynamics of the $5^2P_{1/2}$ state.

We measure the spectrum of the $5^2D \leftarrow 5^2P_{1/2}$ transition of Rb atoms on He droplets. The $5^2P_{1/2}$ state is reached from the ground electronic state $5^2S_{1/2}$ with a continuous-wave (cw) pump laser and the transition of interest is excited with a pulsed laser. This specific two-color two-photon excitation will be named two-step excitation, due to the bound character of its intermediate state, which allows the excited atom to stay at the nanodroplet surface.

The direct one-color two-photon transition has been measured in Ref. 61, where we also introduced the notations used here. For the sake of convenience we use three different notations to label the electronic states of the Rb atom. (i) The first notation is that of the bare atom in the LS coupling scheme; He_N is treated as a perturbation and defines the quantization axis as normal to the nanodroplet surface. (ii) The second notation is that of a diatomic molecule, where the whole He nanodroplet is treated as a fictitious atom;[57] in this case the quantization axis is also the molecular axis. We choose a Hund's case (a) coupling scheme, and the standard associated notation: $^{2S+1}\Lambda_\Omega$, where S is the spin of the system, Λ is the projection of the electronic orbital angular momentum on the quantization axis and Ω is the projection of the total electronic angular momentum on the quantization axis. (iii) The third notation is the one of a diatomic molecule with neglected spin-orbit coupling: $^{2S+1}\Lambda$. This corresponds to a shift of free-atom levels by the perturbation of the droplet and a possible state mixing. The quantization axis z is the same as the molecular axis in (ii). The correlation between the different notations can be seen in a diagram (Fig. 3.1). The $5^2S_{1/2}$ ground state correlates to the diatomic $^2\Sigma_{1/2}$ state. The $5^2P_{1/2,3/2}$ multiplet correlates to three molecular states: $^2\Pi_{1/2}$, $^2\Pi_{3/2}$, and $^2\Sigma_{1/2}$, whereby only upon excitation into the $^2\Pi_{1/2}$ state does the Rb atom remain bound and can be used for our purpose.[60] For the 5^2D state, spin-orbit coupling is much weaker (energy splitting: $3.04\,\mathrm{cm}^{-1}$, Ref. 97) than the perturbation by He_N, and can be neglected, so that three distinct diatomic states exist: $^2\Sigma$, $^2\Pi$, and $^2\Delta$, with orbital degeneracy 1, 2, 2, respectively. Electric-dipole transition rules allow an one-photon transition from the $5^2P_{1/2}$ ($^2\Pi_{1/2}$) state to all 5^2D states ($^2\Sigma$, $^2\Pi$, $^2\Delta$).

We compare the experimental spectrum first with the experimental spectrum of the direct one-color two-photon $5^2D \leftarrow 5^2S_{1/2}$ excitation, second, with the calculated Franck-Condon factors for the potential energy curves of the diatomic representation.

This chapter is organized as follows. In Sec. 3.2, we present the experimental set-up,

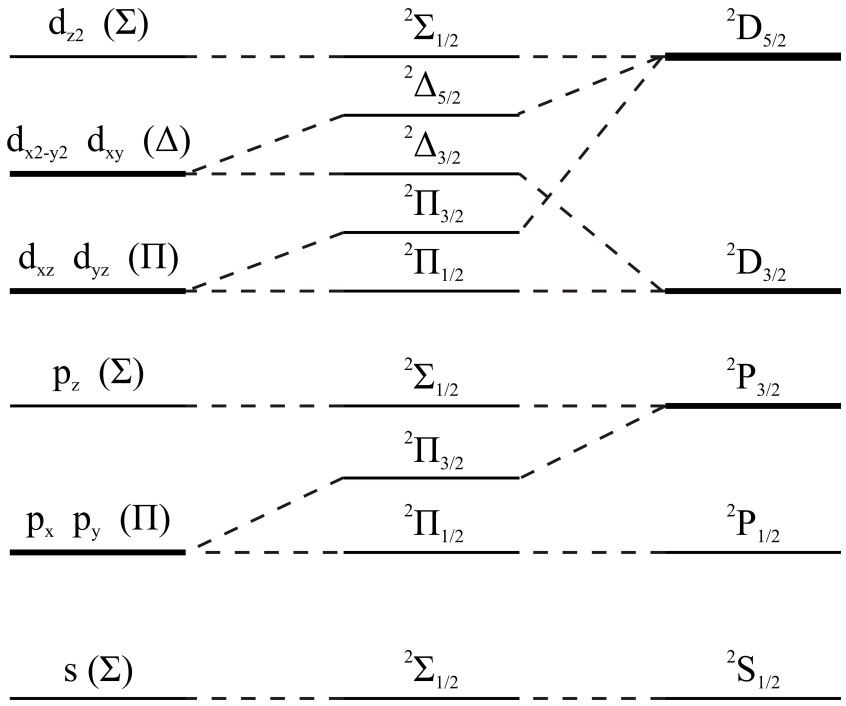

Figure 3.1.: Correlation diagram between the different pictures (from right to left): (i) spin-orbit-coupled atomic orbitals, (ii) diatomic Hund's case (a) states, and (iii) atomic orbitals with strong axial perturbation in the direction of the molecular axis z with the spinless molecular states in parenthesis according to Ref. 61. Note that the energies are not to scale.

in Sec. 3.3 the laser-induced fluorescence (LIF) spectra; in Sec. 3.4, we show evidence for a two-step excitation by comparison with an one-color two-photon experiment, and we show how the experimental data are consistent with expected excitation cross-sections (Sec. 3.4.1). We corroborate this with model calculations (Sec. 3.4.2), which adequately reproduce the experimental spectra. Sec. 3.5 contains a brief summary and conclusions.

3.2. Experimental

General principles of excitation and emission spectroscopy of alkali-metal atoms on He nanodroplets have been described in Refs. 57 and 59. The nanodroplet beam apparatus used here has been described in detail in Ref. 46. A schematic of the setup is shown in Fig. 3.2.

In short, He_N with an average size $\bar{N} = 10^4$ atoms are formed in a free-jet expansion of He gas (Air Liquide, Alphagaz 2, grade 6.0) with a stagnation pressure of 60 bar through a 5 μm nozzle cooled to 14 K.[98] The He nanodroplet beam passes through a pick-up cell,

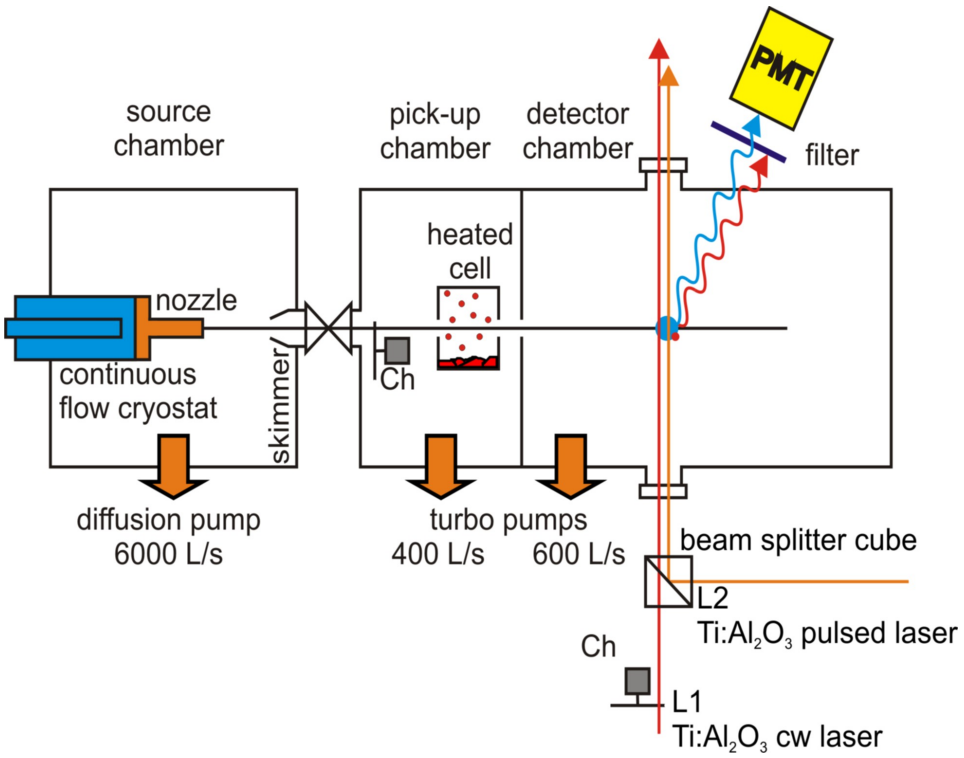

Figure 3.2.: Schematic of experimental setup (Ch:chopper, PMT: photomultiplier tube).

filled with Rb, and picks up atoms with a probability that depends on the Rb vapor pressure in the cell. The ratio of nanodroplets doped with monomers, dimers, trimers, etc., can thus be controlled through the temperature of the cell (and through the nozzle temperature and the stagnation pressure). We therefore measure the intensity of the D_1 line for Rb and Cs monomers at a fixed wavelength and vary stagnation pressure and oven temperature. The intensity is directly measured with LIF, where the signal is given in cts./s (Fig. 3.4) and represents the abundance of monomer doped nanodroplets. One can directly see that the best pick-up conditions for Rb monomers are at pick-up cell temperatures ranging from 110 °C to 120 °C for small cluster sizes and $100 - 110$ °C for large clusters sizes. The temperature in this experiment is set to 110 °C to maximize the production of single doped nanodroplets.

Two Ti:Sapphire lasers (L1 cw; L2 pulsed) are used for sequential excitation. Their specifications are as follow:

- L1 is a cw Ti:Sapphire laser (Coherent 899-01) kept at a fixed wavenumber (12601, 12605, and 12611 cm^{-1} are used in this experiment) and a power of 2.5 W. It excites the Rb atom on the nanodroplet from the $5^2S_{1/2}$ ($^2\Sigma_{1/2}$) state to the $5^2P_{1/2}$ ($^2\Pi_{1/2}$) state.

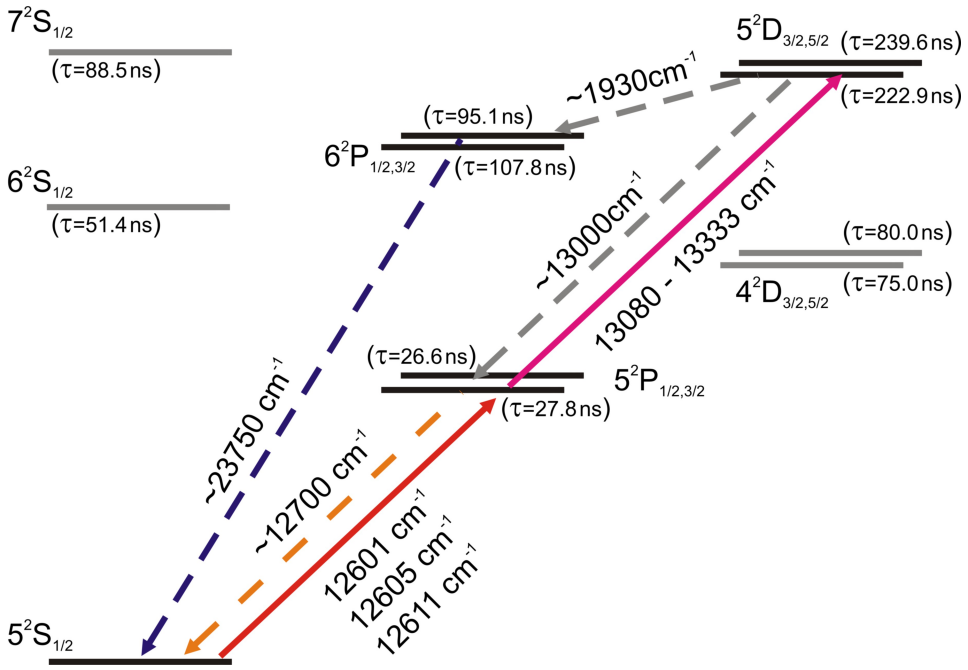

Figure 3.3.: Level diagram of the Rb atom. Solid and dashed arrows indicate excitation and decay routes, respectively. The lifetimes τ refer to the bare atom and are calculated as the inverse of the Einstein coefficients from Ref. 99. In Ref. 61, 6^2P and 5^2D states of Rb-He$_N$ could be reliably assigned by measuring time-dependent LIF signals and comparing these with calculated lifetimes for the bare Rb atom. Also, it is known that the lifetime of Ak-He excimers is not significantly different from that of the free atom [100], so that the lifetimes of Rb*-He$_N$ should not differ strongly from the given τ values. In addition, the influence of superfluid He on the lifetime of the $5^2P_{1/2}$ state itself has been examined in Ref. 101, where no significant lowering of the lifetime has been found when using low He pressure. The red arrows show the excitation scheme used in this experiment. The emission via the blue arrow serves for detection.

- L2 is a tunable pulsed Ti:Sapphire laser (Coherent Indigo S: pulse energy $\sim 200\,\mu$J, repetition rate 5 kHz, pulse duration 30 ns) with a scanning range from 10807 cm^{-1} (920 nm) to 13333 cm^{-1} (750 nm). L2 excites the Rb-atom from the $5^2P_{1/2}$ ($^2\Pi_{1/2}$) state to the 5^2D state manifold.

The excitation and detection scheme is shown in Fig. 3.3. Both laser beams run perpendicular to the cluster beam; they must spatially overlap at the intersection with the nanodroplet beam, because the distance traveled by a nanodroplet over the lifetime of the $5^2P_{1/2}$ ($^2\Pi_{1/2}$) state is negligible (few μm). In order to discriminate against one-color two-photon processes, excited by the pulsed laser L2, the cw laser L1 is chopped: the difference signal represents the sequential excitation.

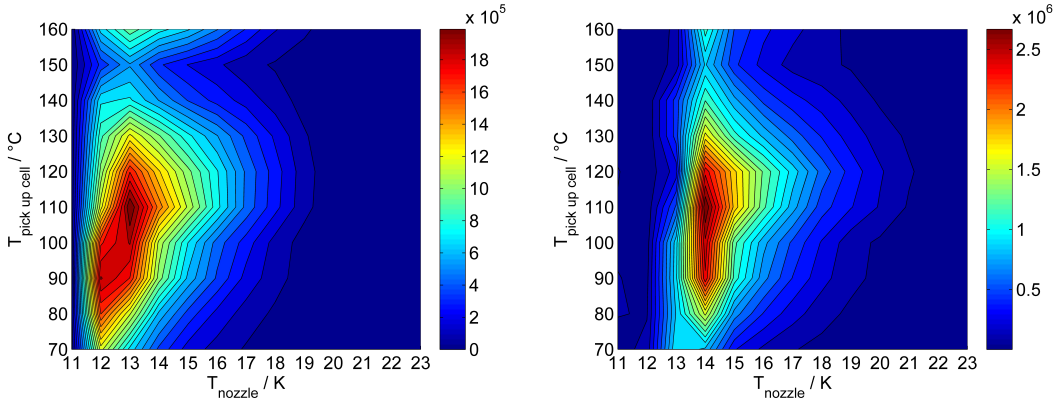

(a) Rb, 40bar (b) Rb, 60bar

Figure 3.4.: LIF signal for Rb monomers **(a, b)** recorded at 12607 cm^{-1} with a laser power of $\sim$ 850 mW at different pick-up conditions (oven temperature, nozzle temperature). The stagnation pressure was either 40 bar **(a)** or 60 bar **(b)**. The colorbars indicate the signal strength.

Laser-induced fluorescence is measured with a Peltier-cooled photomultiplier (housing: Product for Research, TE210TS-RF; tube: Hamamatsu R943-01 with GaAs photocathode). There are several decay routes from the 5^2D states, which can be used for fluorescence light detection. We have chosen to detect fluorescence from the $6^2P \rightarrow 5^2S_{1/2}$ transition at 23750 cm^{-1} (Fig. 3.3). This has the advantage that stray light from both lasers, as well as spontaneous emission from the intermediate state, can be easily suppressed with a colored filter (Schott BG39). We further suppressed stray light by gated photon counting (counter: Stanford Research SR400, triggered by L2). For the measurements presented here the gate width was set as 1000 ns, that is, much longer than the lifetimes of the levels involved, and much shorter than the interval between two laser pulses.

3.3. Results

The LIF signal was recorded with L1 fixed at one of three different photon wavenumbers (12601 , 12605 , and 12611 cm^{-1}) and L2 scanned between 13080 cm^{-1} and 13333 cm^{-1}. When L1 is absent only one-color two-photon processes excited by L2 and stray light from L2 are measured. With both L1 and L2 active, additional signal derives from the desired two-step excitation and from stray light due to L1. The latter can be neglected as it amounts to $0.1 - 0.2$ counts per second with gating ($20 - 40$ counts per second without gating). The difference signal represents the two-step excitation spectrum which we show in Fig. 3.5 and Fig. 3.6 as counts per second (i.e., counts per 5000 laser pulses).

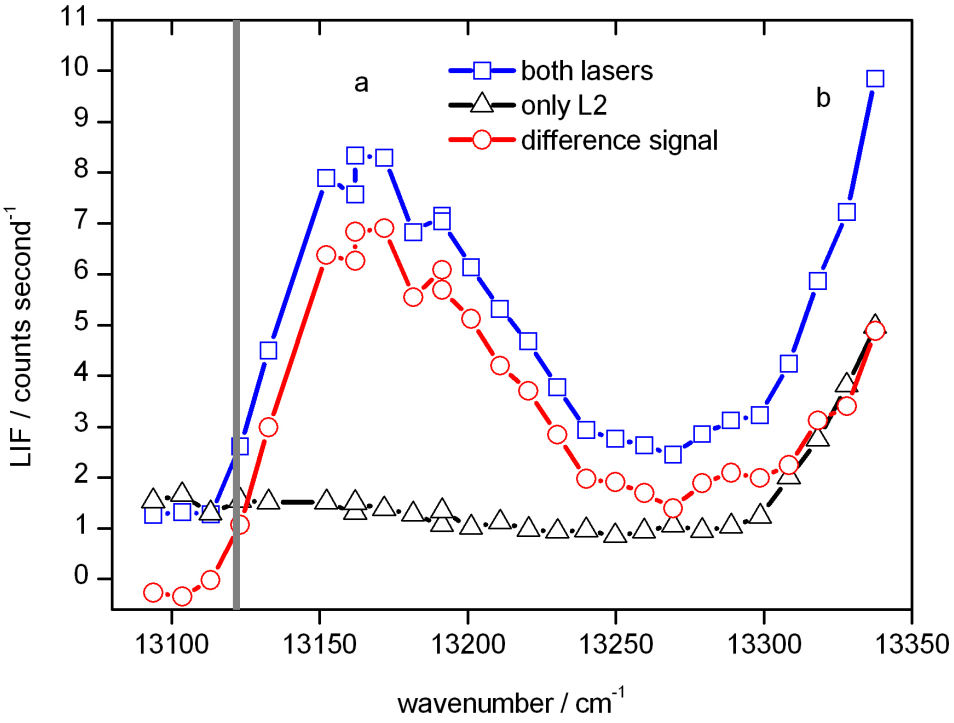

Figure 3.5.: LIF signal with L2 laser only, and with L1+L2. The photon energy of L1 is fixed: $E/(\mathrm{hc})$=12611 cm^{-1}. The vertical line shows the position of the $5^2\mathrm{D} \leftarrow 5^2\mathrm{P}_{1/2}$ transition in the bare Rb atom. Features **a** and **b** are discussed in the text.

The two-step excitation has one broad peak (peak **a**) extending from 13120 cm^{-1} to 13250 cm^{-1}, with maximum at 13183 cm^{-1}. Another broad shoulder (shoulder **b**) starts at 13300 cm^{-1}, and shows no maximum up to the higher end of the scanning range of L2, 13340 cm^{-1}. Peak **a** only shows a slight variation with photon energy of L1, whereas the variation of shoulder **b** is much more pronounced.

The stronger variation of shoulder **b** can be explained as follows. Statistics dictates that a significant fraction of the droplets be doped with *two* Rb atoms, which form a triplet dimer. The one-photon $(1)^3\Pi_g \leftarrow a^3\Sigma_u^+$ transition of Rb_2-He_N falls in this wavenumber range and can be excited by L2.[98,102] Furthermore, for specific excitation energies a spin-flip occurs and the dimer changes from a triplet to a singlet state. Fluorescence emission from the singlet dimer occurs at higher wavenumber than the exciting laser (because the $X^1\Sigma_g^+$ singlet ground state is much lower in energy than the $a^3\Sigma_u^+$ triplet state[102]) and will not be suppressed by the filter. This leads to a signal increase

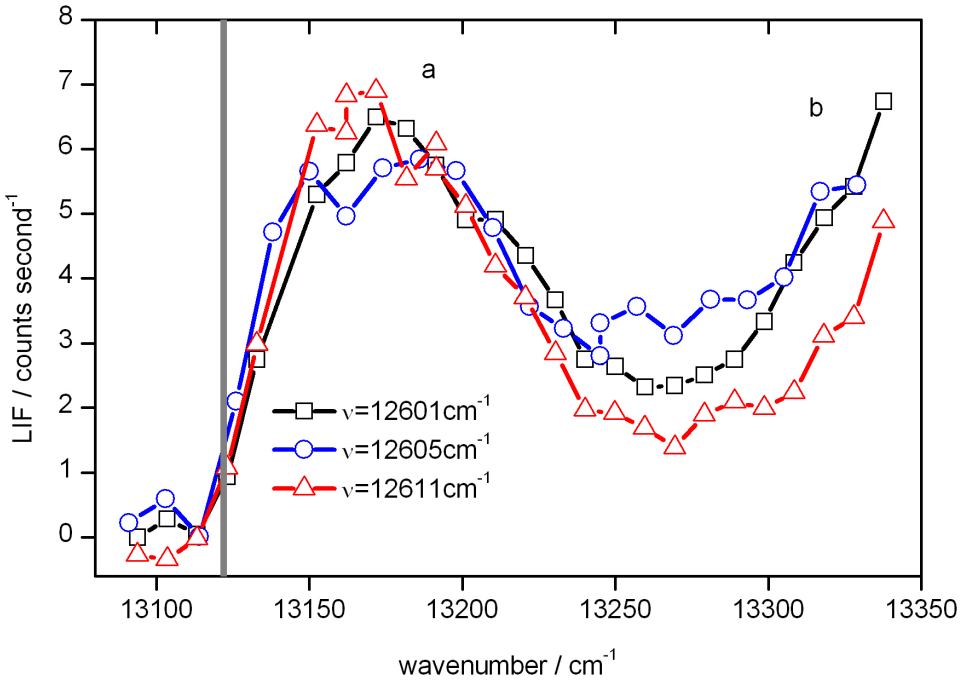

Figure 3.6.: Two-step excitation LIF spectra for the $5^2D_{1/2,3/2} \leftarrow 5^2P_{1/2} \leftarrow 5^2S_{1/2}$ excitation at different photon wavenumbers ν of laser L1, as indicated. All signals are difference signals as described in the text. The vertical line shows the position of the $5^2D \leftarrow 5^2P_{1/2}$ transition in the bare Rb atom. The abscissa shows the photon wavenumber of laser L2. Features **a** and **b** are discussed in the text.

in both cases (L2 only, L1 and L2). The recorded LIF signals, when both lasers (L1 and L2) and only L2 are used, as well as their difference signal are shown in Fig. 3.5 for a pump wavenumber of 12611 cm^{-1}. We conclude that after subtraction, the remaining portion of **b** represents the true contribution of the 5^2D excitation.

No spin-orbit structure can be resolved in peak **a**, nor will it be included in the calculations of Sec. 3.4.2. This is simply due to the much smaller spin-orbit splitting of the 5^2D state, which is completely overcome by the line broadening due to the perturbing influence of He_N.

3.4. Discussion

We now discuss the evidence that we see a genuine two-step excitation of Rb atoms that remain attached to a He nanodroplet after being excited into their first excited state.

The fluence of L1 Φ_1 ($7.5\,\mu J/cm^2$ in 30 ns) at the given wavelength is not sufficient to excite an one-color two-photon transition, and it is also obvious from Fig. 3.5 that L2 alone causes a flat response across its scanning range. Peak **a** and shoulder **b** in the difference signal are due to the combined action of both lasers. In Sec. 3.4.1 we compare our experimental data with those of earlier measurements, where the 5^2D state was excited directly.[61]

Then we compare our data with the Franck-Condon factors obtained from calculated pseudo-diatomic potential energy curves (Sec. 3.4.2). We further argue that in the 5^2P ($^2\Pi_{1/2}$) state the Rb-He_N relaxes vibrationally in a time much shorter than the natural lifetime of the electronic state.

3.4.1. Comparison to direct two-photon excitation $5^2D \leftarrow 5^2S_{1/2}$

The LIF spectrum and the lifetime of the 5^2D state were measured, and reliably assigned, by one-color two-photon excitation from the ground state.[61] We have repeated the experiment and in Fig. 3.7 we compare the corresponding LIF spectrum with our results from Sec. 3.3. Time-resolved fluorescence decays for the two excitation schemes do not show any significant difference. In conclusion, the 5^2D state is excited in both cases, but some differences are evident upon close inspection.

i) The photon-energy threshold of the two-step excitation is lower. With the calculated potential curves this can be explained easily, so that we foreclose some of those results. The Rb atom excited into the $5^2P_{1/2}$ ($^2\Pi_{1/2}$) state not only stays on the nanodroplet, but also adjusts its position to a longer distance.[60] The excitation from the $5^2P_{1/2}$ ($^2\Pi_{1/2}$) into the 5^2D state manifold takes now place at a distance where the upper potential is closer in energy. The reason for this will be discussed in Sec. 3.4.2. In total, less energy is needed, as compared to the one-color two-photon excitation, to excite into the 5^2D state manifold.

ii) The two-photon two-step spectrum exhibits a sharper structure than the one-color two-photon spectrum; as we will see, this is also consistent with vibrational relaxation within the $5^2P_{1/2}$ ($^2\Pi_{1/2}$) state.

The cross-section for the one-color two-photon excitation $5^2D \leftarrow 5^2S_{1/2}$ is high in comparison to analogous ones in other members of the Ak atom family, because the virtual intermediate state is very close to the $5^2P_{3/2}$ state. Indeed, for this very reason this specific excitation scheme has also been used for bare Rb atoms.[103] Let us remember that the cross-section for two-photon processes is inversely proportional to the square of the detuning between the virtual intermediate state and real intermediate state(s).[104]

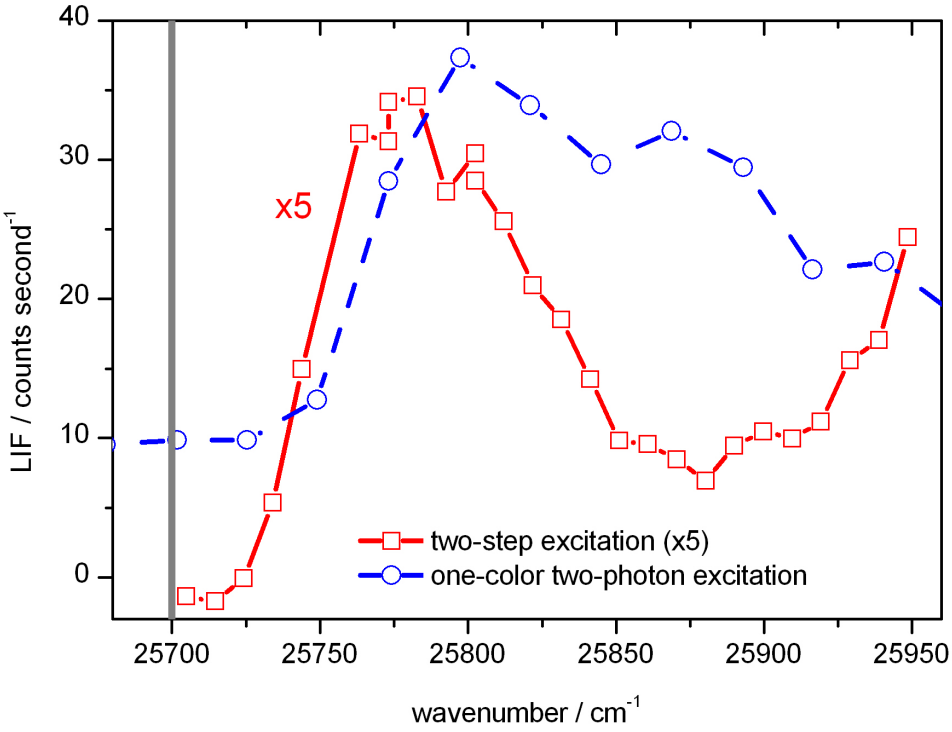

Figure 3.7.: Comparison between two-step excitation, where L1 has been kept fixed at 12611 cm^{-1}, and one-color two-photon excitation of Rb atoms on He nanodroplets. The vertical line shows the position of the $5^2D \leftarrow 5^2S_{1/2}$ transition of the bare Rb atom.

For other ^2S and ^2D states and/or other Ak atoms there are no states this close to half the excitation energy[97], so that there is no significant enhancement of the one-color two-photon excitation.[94]

In terms of one-color two-photon excitation, the 5^2D state studied here is thus a rather favorable exception. We clearly see it, if we compare the experimental LIF signals for the two different excitation schemes:

- 5^2D ($^2\Sigma$, $^2\Pi$, $^2\Delta$) $\leftarrow 5^2S_{1/2}$ ($^2\Sigma_{1/2}$): ~ 35 count/s after subtracting dark counts at the maximum of peak **a** (fluence $\Phi_{(2)}$ of L2 $\sim 26\,mJ/cm^2$)
- 5^2D ($^2\Sigma$, $^2\Pi$, $^2\Delta$) $\leftarrow 5^2P_{1/2}$ ($^2\Pi_{1/2}$) $\leftarrow 5^2S_{1/2}$ ($^2\Sigma_{1/2}$): ~ 7 count/s (fluence Φ_2 of L2 $\sim 16\,mJ/cm^2$)

Let us note, however, that even for this favorable case the advantage of the one-color two-photon scheme is only a factor of ~ 5. If a pulsed laser were also used for the first

of the two-step excitation, the efficiency of the scheme would be greatly improved. The fluence Φ_1 of our cw L1 over the pulse duration of L2 (30 ns) is $\sim 7.5\,\mu\mathrm{J/cm^2}$, i.e., $\sim 10^3$ times smaller than Φ_2.

Let B_{01} and B_{12} be the Einstein coefficients for absorption from the ground $|0\rangle$ to the intermediate $|1\rangle$ state and from the intermediate $|1\rangle$ to the final $|2\rangle$ state, respectively, and N_0 the population of the ground state, Φ_1 the laser fluence of the first step, Φ_2 of the second step, and $\Phi_{(2)}$ for the two-photon excitation. $B_{(2)}$ shall be a two-photon absorption rate coefficient that depends on the energy mismatch of intermediate levels. With these, we get a total population of the final state for the case of the two-step excitation

$$N_2 \sim B_{01} B_{12} N_0 \Phi_1 \Phi_2$$

and for the case of direct two-photon excitation

$$N_2 \sim B_{(2)} N_0 \Phi_{(2)}^2.$$

With $\Phi_1\Phi_2$ being more than 3 orders of magnitude smaller than $\Phi_{(2)}^2$ in our case and the signals of similar magnitude, one can easily see that the two-step excitation is by far favorable.

3.4.2. Potential curves and Franck-Condon factors

The potential energy curves, versus distance R from the center of the nanodroplet, of Rb atoms have been calculated and are shown in Fig. 3.8 for the relevant states: $5^2\mathrm{S}_{1/2}$ ($^2\Sigma_{1/2}$), $5^2\mathrm{P}_{1/2}$ ($^2\Pi_{1/2}$) and $5^2\mathrm{D}$ ($^2\Sigma_{1/2}$, $^2\Pi_{1/2}$, $^2\Delta_{1/2}$). For the calculation, the static helium density distribution of $\mathrm{He_N}$ calculated for $N = 2000$ at equilibrium with a ground-state Rb atom was used. The details of this approach are published separately by C. Callegari and F. Ancilotto.[105] Spin-orbit effects for the $5^2\mathrm{P}_{1/2,3/2}$ states were taken into account through the introduction of a perturbation not dependent on R. This was done in analogy to Takami and co-workers[106] and Reho et al.[107] It can be seen that at large R the influence of $\mathrm{He_N}$ weakens and the energy of the states converges to the one of a bare Rb atom. Given these curves, we calculated the Franck-Condon factors between the electronic states of interest, using the BCONT 2.2 code for bound-free transitions by R. J. LeRoy.[108].

As described, L1 pumps the $5^2\mathrm{P}_{1/2}$ ($^2\Pi_{1/2}$) state, whereby we assume the Born-Oppenheimer approximation, so that the most likely transition from the ground state to the $5^2\mathrm{P}_{1/2}$ state occurs at a fixed R. Measured $5^2\mathrm{P}_{1/2} \leftarrow 5^2\mathrm{S}_{1/2}$ excitation spectra and the fluorescence emission back to the Rb-$\mathrm{He_N}$ ground state imply relaxation of the Rb*-$\mathrm{He_N}$ distance to a new equilibrium position, presumably accompanied by a He density relaxation (Rb* indicates the electronically excited Rb atom).[60] A small amount

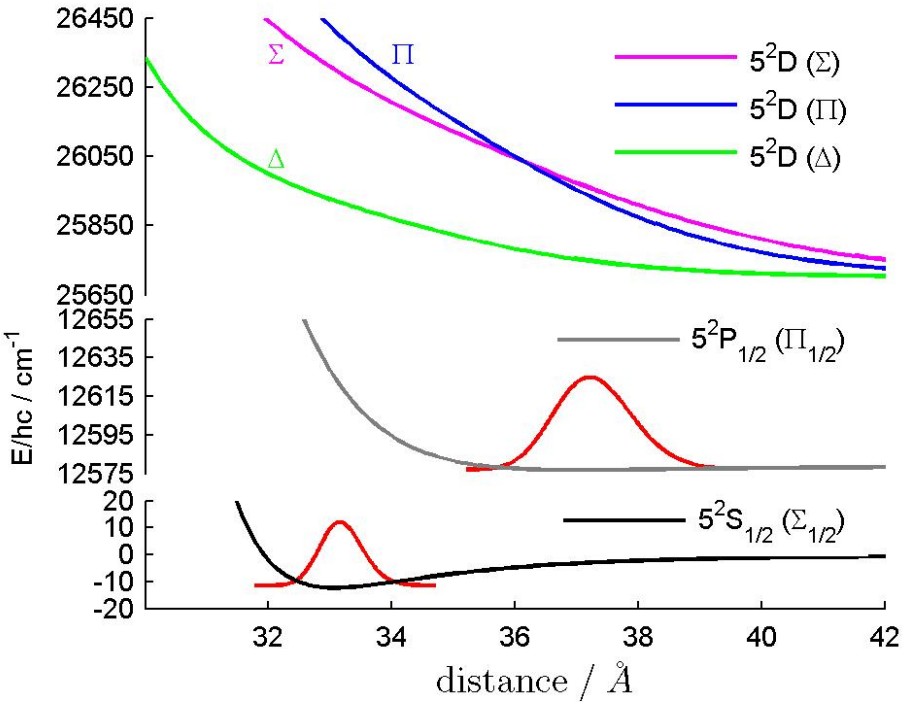

Figure 3.8.: Calculated potential curves of one Rb atom on the He nanodroplet for the $5^2S_{1/2}$ ($^2\Sigma_{1/2}$), $5^2P_{1/2}$ ($^2\Pi_{1/2}$) and 5^2D ($^2\Sigma_{1/2}$, $^2\Pi_{1/2}$, $^2\Delta_{1/2}$) states. The given distance is between the center of the He nanodroplet and the Rb atom. The red curves show the squares of the nuclear wavefunctions of the lowest vibronic states.

of energy is absorbed in each pump cycle, which consists of excitation and fluorescence emission. This is most likely dissipated by evaporation of He atoms, which leads to smaller nanodroplet sizes during each relaxation process.

The potential minimum of the excited $5^2P_{1/2}$ ($^2\Pi_{1/2}$) state lies at larger R, and in principle all its several vibrational levels can be populated; the shape of the two-step excitation spectrum directly reflects which ones effectively are. The Franck-Condon factors from the $v'' = 0$ ($^2\Pi_{1/2}$) state alone reproduce well the experimental spectra, although they do miss some of the intensity of peak **a** at high photon wavenumber. The population of higher vibronic states ($v'' > 0$) would shift the calculated envelope closer to the transition of the bare atom, so to the accuracy of our calculated potential energy curves, our conclusion is that thermal equilibrium at the temperature of the droplet (370 mK) has been reached; there, the population of the vibronic ground state is $\sim 80\%$.

In Fig. 3.9 we show the corresponding Franck-Condon factors to the three different diatomic states which correlate to 5^2D: $^2\Sigma_{1/2}$, $^2\Pi_{1/2}$, $^2\Delta_{1/2}$, and we compare those with the experimental data. As can be seen peak **a** belongs to the transition to the $^2\Delta_{1/2}$

state, while peak **b** is a mixture of the transitions to the $^2\Sigma_{1/2}$ and $^2\Pi_{1/2}$ states. Because we cannot record peak **b** in full, we cannot further analyze it. The transition probabilities from specific vibronic states ($v'' = 0$–11) to the three different final electronic states were also calculated separately. As said population distributions other than the one at thermal equilibrium do not show any better agreement with the experimental data.

Accounting for helium density relaxation would lead to a change in the $5^2P_{1/2}$ and 5^2D potential curves. This effect is rather small compared to the change in energy difference between $5^2P_{1/2}$ and 5^2D caused by the increased distance between Rb atom and He nanodroplet. Nevertheless, the agreement may get better with a relaxed He density.

With the interpretation that our LIF spectra represent a thermal equilibrium, we can infer that the vibronic states relax faster than the electronic excitation, thus on a few ns (or faster) timescale. By extrapolating what is known for Ak-He excimers,[100] we presume that the lifetime of Rb in its bound $5^2P_{1/2}$ ($^2\Pi_{1/2}$) state is not significantly altered by the influence of the droplet, so that after the relaxation into the vibronic ground state one has practically the full lifetime of the electronic state to further excite the Rb atom.

3.5. Conclusions

We have observed the first sequential excitation of atom-doped helium nanodroplets (here Rb atoms), where the atom in the intermediate state stays bound to the nanodroplet. The LIF spectrum was measured for different photon energies of the pump laser and compared to the spectrum of an one-color two-photon excitation. The differences between these spectra indicate a dynamic process in the intermediate state. We further see that the two-step excitation process yields sharper spectra. The dynamic process in the intermediate state can be interpreted as a relaxation from high vibronic states into a thermal equilibrium. Under this assumption, the calculated Franck-Condon factors between the involved states adequately match our experimental data. A comparison of the one-color two-photon excitation and the two-step excitation shows that only by a fortunate coincidence the one-color two-photon transition into the 5^2D states looks favorable. This means that in general the $5^2P_{1/2}$ ($^2\Pi_{1/2}$) state is advantageous as springboard to reach highly excited states.

Regarding other alkali-metals, we expect, and have evidence, that cesium (Cs) also stays bound on a He nanodroplet upon excitation to its $6^2P_{1/2}$ ($^2\Pi_{1/2}$) state. The barrier in the $6^2P_{1/2}$ state of the Cs-He pair potential as given in Ref. 109 lets us predict that the desorption channel associated to Ak*-He exciplex formation is closed too, as it is for

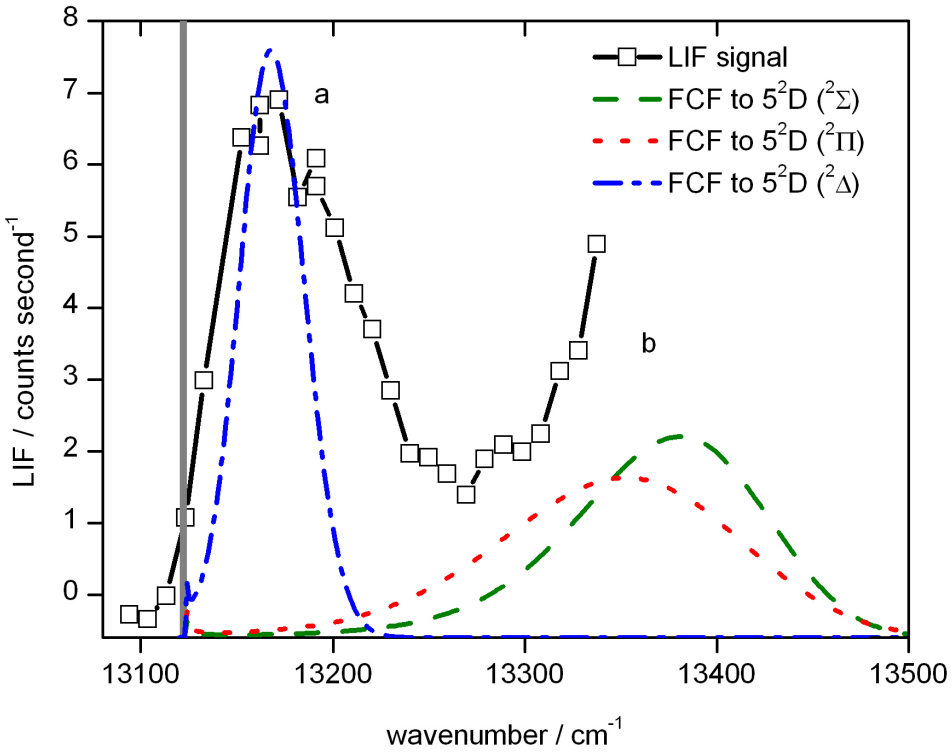

Figure 3.9.: Comparison of the measured LIF spectrum and the calculated Franck-Condon factors (FCF) for the transition from the $5^2P_{1/2}$ ($^2\Pi_{1/2}$) state to the 5^2D states: $^2\Sigma$, $^2\Pi$, $^2\Delta$.

Rb^{60}. This question will be discussed in chapter 5.

We consider the demonstrated two-step excitation to be the beginning of a detailed investigation of higher ns and nd states of Rb and Cs on He_N. The $5^2P_{1/2}$ ($^2\Pi_{1/2}$) state as springboard, will enhance the total excitation cross-section over an one-color two-photon scheme from the ground state. Due to their larger orbital angular momentum, higher nd orbitals should interact less with the He_N-Rb^+ or He_N-Cs^+ core than np states and converge to the situation of a single electron orbiting around a positively charged alkali-helium nanodroplet complex. In order to gain the most polarization energy, the alkali ion will be drawn to the center of the nanodroplet.

The creation of such large artificial atoms is of fundamental interest. Rydberg states provide a sensitive measure of the electronic structure of the core and in this case, will test some predictions that were recently published.[110]

4. Ionization of Rubidium atoms and clusters on He nanodroplets

In this chapter we present the ionization of single rubidium (Rb) atoms and small Rb clusters on the surface of He droplets. Attractive forces between positively charged alkali-metal (Ak) ions and superfluid He are much stronger than the one between neutral Ak atoms and He. In several theoretical works the Ak^+ ion is therefore encircled by He atoms, unlike the Ak atom being surface located. Due to the strong interaction between Ak^+ ion and He the He atoms may be frozen around the ion, so that one can speak of a snowball. The observation of prominent Ak^+-He_n sizes upon ionization helps to find stable structures, which goes along with He shell closings around the Ak ion. We further find that after ionization of Rb atoms and small clusters the resulting Rb^+ ions immerse into the droplet subsequently, so that the ionization threshold of the Rb-He_N system cannot be identified by varying the photon energy of the ionizing laser and monitoring Rb^+. One has to observe heavy masses: Rb^+-He_N. Here, we describe our experimental results to form Rb^+-He_n snowballs in the center of a He droplet, which have been published in Phys. Chem. Chem. Phys ***12*** *(2010) 14861 as cover article (Ref. 2). In addition, our former findings of small Rb^+ clusters as well as theoretical considerations regarding snowballs are presented.*

4.1. Ionization products of He nanodroplets doped with Rb atoms and small clusters

The energy levels of Rydberg states at the surface of liquid He are shifted only by a small amount.[111] Therefore the influence of superfluid He on the ionization threshold (IT) of Ak atoms should be small, too. We expect, that the IT is lowered, because of the strong attractive potential between Ak^+ and He.

Rb atoms and small Rb clusters (Rb_n) are either ionized in an one-photon or in a multi-photon ionization scheme with a pulsed Ti:Sapphire laser (Coherent, Indigo S, repetition rate 5 kHz, frequency doubling and tripling available). A time-of-flight (TOF) mass spec-

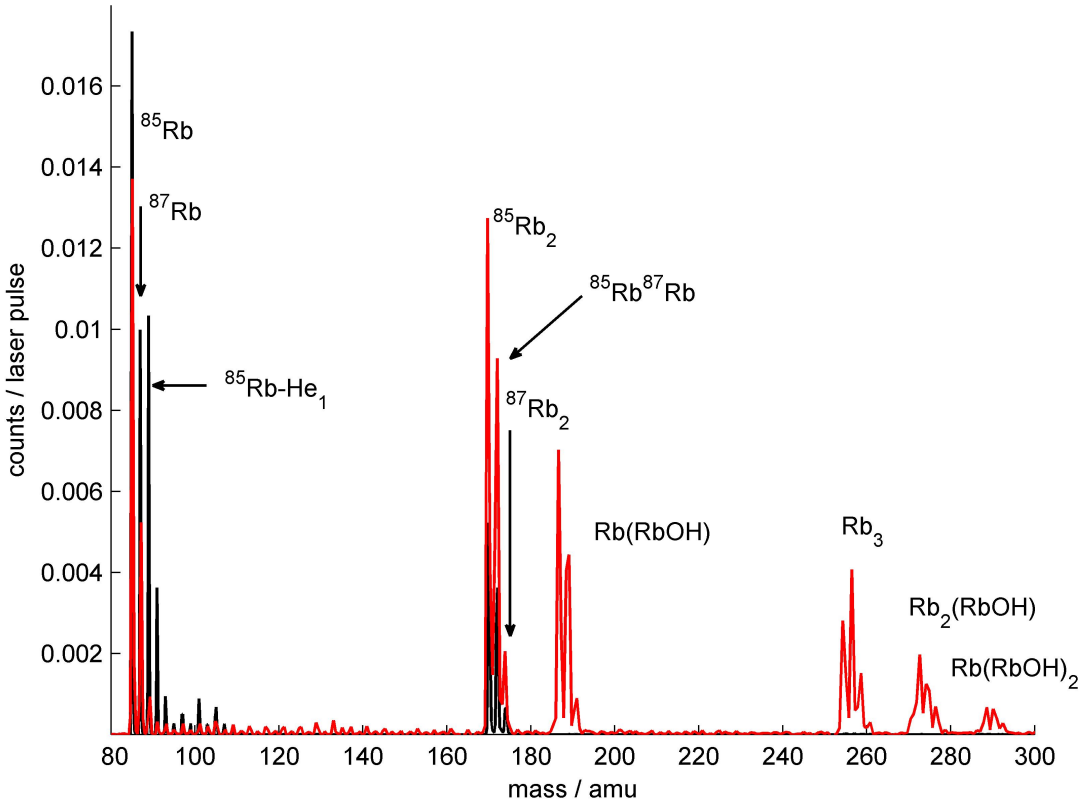

Figure 4.1.: TOF spectra of Rb-doped He droplets obtained with photon energies of $\tilde{\nu} = 33430$ (red), $21911\,\mathrm{cm}^{-1}$ (black). The signal strength is given in counts per laser pulse. Mainly due to different pulse energies, cross sections, and Rb_n cluster sizes the signals are different in heights. The abscissa scale is given in amu. Features of the signals and of different ionization products are explained in the text.

trometer is placed along the beam axis. In Fig. 4.1 the different ionization products for two ionization processes with different photon energies (one-photon: $\tilde{\nu} = 33430\,\mathrm{cm}^{-1}$ and REMPI: 12830 (cw laser) and $21911\,\mathrm{cm}^{-1}$) are displayed. Note, that the constant electrical field between the extraction plates lowers the ionization threshold by a small amount $\Delta E\,[\mathrm{cm}^{-1}] \sim 6.1215 \times \sqrt{F\,[\mathrm{V/cm}]}$ (here $\sim\ 110\,\mathrm{cm}^{-1}$).

One can identify the different isotopes of Rb (^{85}Rb and ^{87}Rb), the existence of oligomers (here Rb_m, $m = 1 - 3$) as well as the formation of Rb^+-He_n, Rb_2^+-He_n and several compounds with water. Because of the nanodroplet size distribution and the vapor pressure of Rb gas in the pick-up cell, Rb oligomer doped $\mathrm{He_N}$ will always be present in the nanodroplet beam beside monomer doped $\mathrm{He_N}$. Also, the pick-up of

H_2O coming from residual water in the chamber is possible. The reactions of Ak atoms with water on He_N were investigated in Ref. 37, so that we only name the here identified products: Rb(RbH), Rb(RbOH), Rb_2(RbOH), Rb$(RbOH)_2$. The presence of Rb_n ($n > 2$) as well as reactions with water strongly depend on the ionization scheme. Whit a REMPI scheme, where the first photon energy is set to a monomer transition of Rb-He_N ($^2P_{3/2} \leftarrow^2 5S_{1/2}$) and the second photon energy belongs to a dimer transition (Fig. 4.1, black signal), we see that only Rb and Rb_2 are ionized. Besides, the droplet size is kept low ($\bar{N} \sim 5 \times 10^3$), so that Rb monomers and dimers are preferably formed on the droplet. This is in contrast to the red signal of Fig. 4.1, where the droplet size is rather large $\bar{N} \sim 2 \times 10^4$ and the photon energy is sufficient to ionize at least dimers in an one-photon process. From this, we think that cold reactions between Rb and water are only possible with at least a Rb_3 and six H_2O molecules similar to reactions between sodium and water in cross-beam experiments.[112,113] There, doping of one Na atom leads to a non-reactive solvation in the water cluster. These Na atoms can now react with Na dimers to different products. Here, He droplets as carrier need to have at least Ak trimers to allow the reaction with water. The ionization energy should be sufficient to trigger the reaction as one reaction step is limited by the production of AkH (activation energy for NaH is 0.6 eV[114]). Note, that the activation energy decreases from Li to Cs. The stability of Ak^+-He_n and the one of Ak_2^+-He_n complexes as well as the formation of Rb^+-He_n snowballs will be described in Sec. 4.2. Experimental results regarding the ionization of single cesium atoms on He_N will be discussed in chapters 5 and 6.

The ionization threshold of Rb is given as 33690.81 cm^{-1}.[115] The one for Rb_2 depends on the spin configuration. We can find only values of the singlet ground state with a calculated vertical ionization energy of 3.89 eV $\equiv$ 31375 cm^{-1} (Ref. 116). According to Ref. 117 the experimental ionization energies are between 3.44 and 3.95 eV, which should be related to different spin states (triplet, singlet). By trend, the ionization threshold decreases with the Rb_n cluster size down to the bulk value, which is equivalent to the work function (Ref. 118: $\sim$ 2.1 eV $\equiv$ 17000 cm^{-1}). Therefore photon energies sufficient to ionize Rb monomer doped He droplets will always ionize Rb clusters on droplets or more general Ak clusters, too.

In a first approach we tried to find the ionization threshold of Rb atoms on He droplets by monitoring photo-ionized Rb^+ ions with our TOF apparatus. The photon energy in an one-photon ionization scheme was scanned to see an influence on the ion yield and find the ionization threshold of Rb atoms on the surface of He_N. In Fig. 4.2 we show the ion count rate of Rb^+ and Rb_2^+ for different photon energies, where we can see that the ion yields of Rb^+ and Rb_2^+ follow the same trend. The influence of the photon energy on the ion yield is also not as significant as one would expect from measurements of the bare atom. Also the ion yields of Rb^+ and Rb_2^+ follow the same trend. At photon

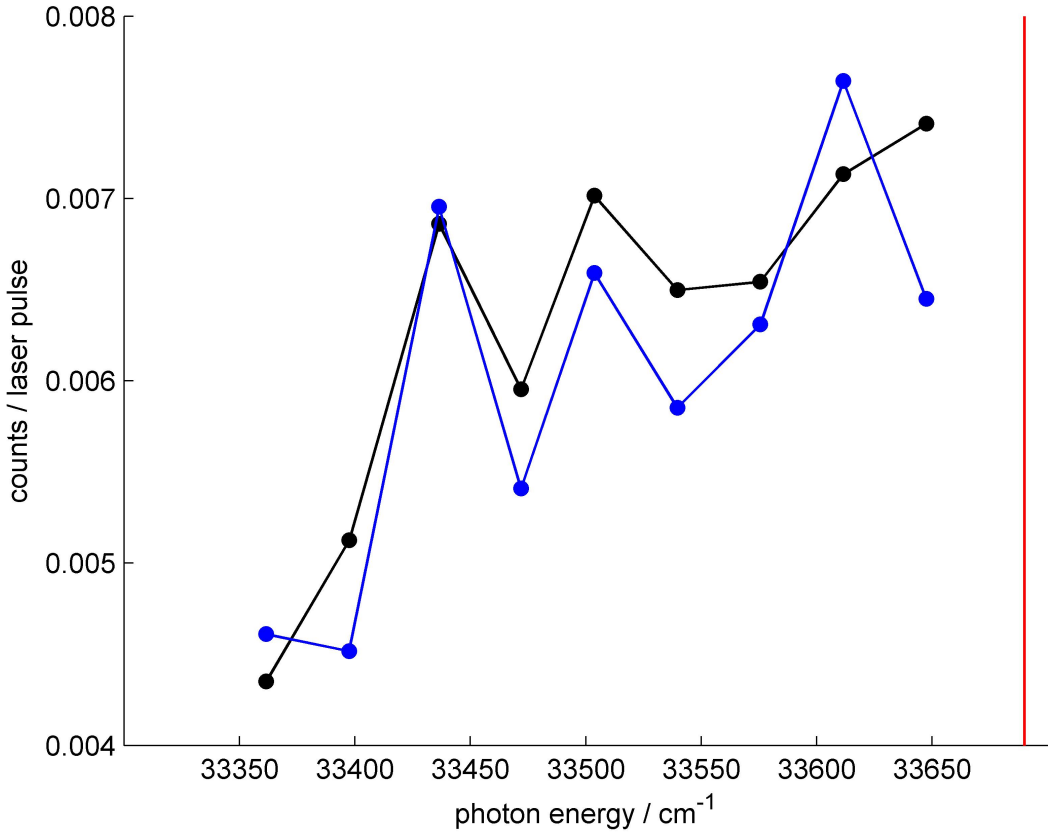

Figure 4.2.: Ion yield of Rb^+ (black) and Rb_2^+ (blue) after excitation and/or ionization with a pulsed laser. The abscissa shows the photon energy of the laser pulse. The vertical red line indicates the ionization energy of free Rb atoms. Mean droplet size $\bar{N}$ is $\sim 2 \times 10^4$ He atoms ($T_n = 12\,\mathrm{K}$, $p_n = 40\,\mathrm{bar}$). The connecting line is to guide the eye.

energies much below the ionization threshold of the bare Rb atom we identify Rb^+, too. The abundance of Rb^+ is (i) connected to the fragmentation of small Rb clusters upon ionization, which clearly goes along with results of others.[30] A main fraction of the fragmented ions are Rb^+ and Rb_2^+, which are at the end of fragmentation processes. (ii) The excitation of Rb-He_N into Rydberg states with a first photon of the laser pulse and the subsequent ionization with a second photon (REMPI) leads to single Rb ions, too. In conclusion, an one-photon excitation (ionization) of Rb-He_N and the detection of Rb^+ does not help to find the ionization threshold of Rb doped He nanodroplets. Let us think about what happens after ionization in order to explain this.

4.2. Theoretical considerations on cation-induced He snowballs and measured Rb^+-He_n structures

The interaction between ions and neutral particles is of general interest, especially in ion-induced processes. The structure of the droplet itself is influenced by the presence of charged particles. The inhomogeneous field of the charged particle polarizes the surrounding He atoms, so that they can be strictly bound to the ion. This structure can be called *snowball*.[119] The He density exceeds the one of solid He and solidifies therefore; in other words the He-He pair distance penetrates into its repulsive region. This solidification can proceed over several shells. Several theoretical and experimental works have concentrated on this phenomenon:

The first theoretical suggestions on this electrostrictive effect were done by Atkins in 1959. He compared the mobility of an ion in liquid ^{4}He (lower) with the one in ^{3}He (higher) and explains this with an electrostrictive effect, by which the ion in ^{4}He drags more He mass with it.[119] Newer theoretical considerations try to find stable structures either deriving from He shell closings or from preferred geometrical structures in a He shell. Theory mainly concentrates on alkali-metal (Ak^+) or alkaline earth metal ions (Ae^+) as they are rather easy to model. One can see from calculated pair-potentials that the attractive forces between Ak^+ and He are much stronger than in the case of Ak-He or He-He (Fig. 4.3).

Calculations using shadow-wave functions show an increase of the He density around Li, Na, K and Cs ions.[62] Here, a non-snowball fluctuating structure in the case of Li^+ and Cs^+ is proposed due to their readily exchange with the He surrounding. Simulations show that the formation of He atoms around Na^+ and K^+ in a cluster He environment is quite distinct from bulk He.[122] The change from bulk He to He clusters goes along with a more clear structuring, too. Another theoretical study enlightens Na^+ doped He clusters and finds a triple-layer structure for $N \geq 100$ at low temperatures ($T \leq 1\,\mathrm{K}$), whereby at least the 3rd layer stays liquid.[66] Also, the formation of solid-like Ak^+-He_n snowballs surrounded by a liquid-like environment is theoretically predicted as given in Ref. 123.

More recent calculations of Reatto and co-workers[65] of several Ak^+-He_{64} (Ae^+-He_{64}) clusters show at least two shells before the He density goes down to zero (Fig. 4.4). By integrating over the He density one can find a distinct number of He atoms for each shell. For the first shell these are for Na^+: 12, K^+: 15, Cs^+: 17-18, Be^+: 15, and Mg^+: 19 atoms. Recently published theoretical results show a similar number of He atoms in the first shell and propose that in the case of Na the 2nd shell is rigid, too.[69] The different

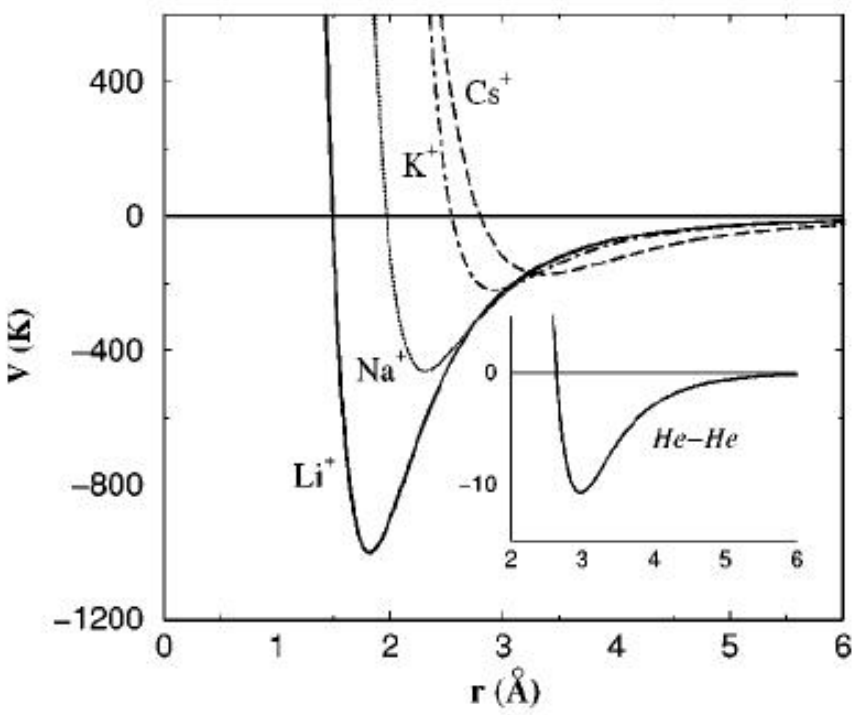

Figure 4.3.: The Ak^+-He pair potentials were calculated in Refs. 120 and 121. The interaction potentials are compared with the He-He pair potential. The figure is taken from Ref. 62.

numbers of He atoms, which arise from different density distributions, are connected to the pair-potentials (cf. Fig. 4.3). The equilibrium distance between Ak^+ (Ae^+) and He varies with the size of the ionic core. With an increasing radius the He density decreases. This can be explained by the interaction of an electric monopole with an induced dipole, which leads to the following electrostrictive potential:

$$V(r) = \frac{e^2}{2\epsilon_0 r^4} \tag{4.1}$$

This simple approach is modified by taking the He-He distance into account. The He-He equilibrium distance is slightly changed by the interaction of the ionic core with the He atoms. Therefore the number of He atoms in the first shell is increased, when the modified He-He distance equals the Ak^+ (Ae^+)-He distance (cf. Fig. 4.4).

Experimentally, closed shells and preferred structures were examined by different groups (e.g. Tiggesbäumker and co-workers). In the case of Cs^+ a first solid-like shell is calculated with $n = 17 - 18$[65], where the number of He atoms was experimentally verified.[70] For Rb no theoretical data are available neither for closed shells nor for magic numbers. Experimentally a first shell closing with $n = 14$ was found recently.[70]

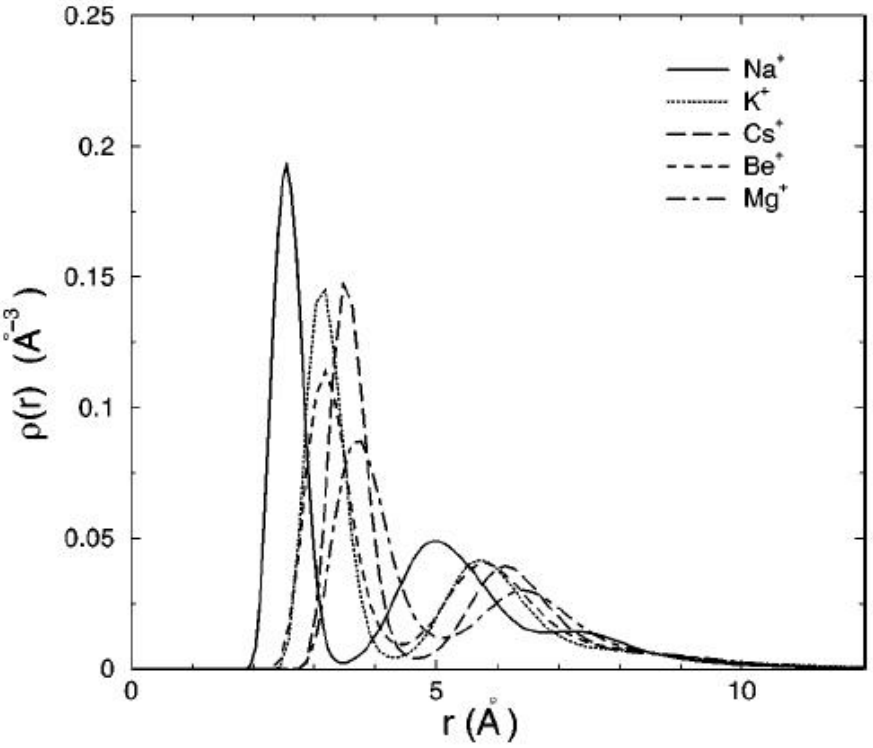

Figure 4.4.: Density of He_{64} clusters around positively charged Ak (=Na, K, Cs) and Ae (=Be, Mg) ions. The figure is taken from Ref. 65.

We monitored Rb-He snowballs by recording mass spectra with our TOF apparatus upon photo-ionization (Fig. 4.5). The formation process of Ak^+-He_n is enhanced, if the initial droplet sizes are large[70] (here: $\bar{N}_i \sim 2 \times 10^4$, $p_0 = 40\,\mathrm{bar}$, $T_n = 12\,\mathrm{K}$). The photon energy was set to $22407\,\mathrm{cm}^{-1}$. Note, that the signal height in the TOF spectra does not represent the signal strength in full. This is because the channel width of our counter was kept fix at 50 ns, so that the signal of one ion species can appear in one or more channels. Therefore the spectra were fitted using Gaussian distributions to obtain the abundance at different masses:

$$f(x) = \frac{A}{\sqrt{2\pi\sigma^2}}\, e^{-\frac{(x-x_c)^2}{2\sigma^2}} \tag{4.2}$$

with area A, center position x_c of the peak, and variance σ^2.

The intensity decrease in the mass regime $85 - 143\,\mathrm{amu}$ (^{85,87}Rb-He_n, $n = 4...14$) is by trend exponentially (note the logarithmic scale). The slightly stronger decrease at $n = 1...4$ is most probably connected to the formation of small exciplexes, which are favorable created. Beyond 141 amu, respectively 143 amu, one can see a strong decrease

Table 4.1.: Shell closings and magic numbers of cations in He as found in different experimental (red bold) and theoretical works (black). "Shell closing" means a filled shell of n He atoms around the cation. "Magic number" means a stable He configuration without filling a shell.

cation	shell closing	magic number	Reference
Li^+	8, 29		62
	10		63
Li_2^+	6	14, 16,18	64
Na^+	12		65,69
	15		63
	16, 51		66
	10, 38		62
Na_2^+	6	20	64
K^+	12, 43		67
	14-15		69
	15		63,65
	12, 40		62
K_2^+		6, 12, 17, 24	64
Rb^+	**14**		70
	14	**12**	this work
Cs^+	**13...19**		70
	17-18	**12, ∼50**	this work (chapter 5)
	17-18		65,69
Cs_2^+		**8**	this work (chapter 5)
Be^+	15		65,69
Mg^+	19		65
	18-19		69
	20		68
	7, 10, 16		71
Mg^{2+}	9		68
	11 ± 1		71
Ag^+	**10, 12, 32, 44**		71
Zn^+	**12**		71
Cd^+	11 ± 1		71
Pb^+	**17**		72
Pb^{2+}	**12**		71
SF_6^+	20		67

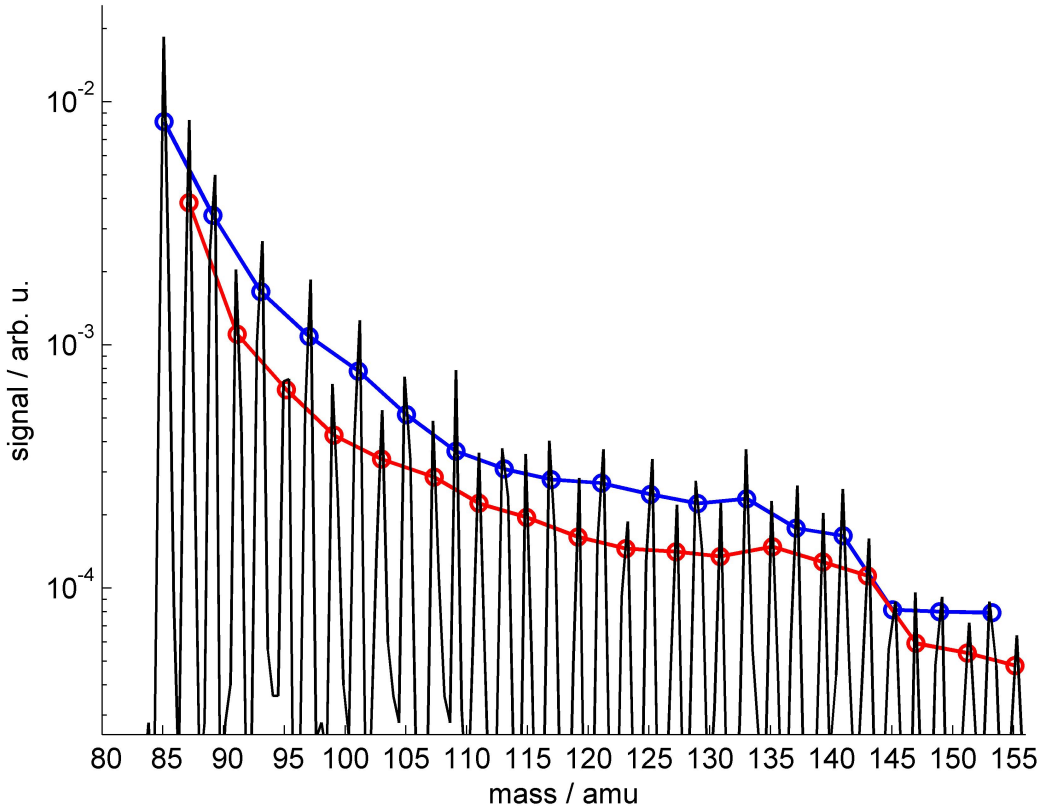

Figure 4.5.: TOF spectra of Rb-He_N upon photoionization with a photon energy of 22407 cm^{-1} in the range of 80 – 156 amu. The blue and red circles represent the area A of each ^{85,87}Rb-He_n peak using a normalized Gaussian distribution. The line between the circles is to guide the eye. Note the logarithmic scale of the ordinate.

of the intensity. This corresponds to a preferred snowball structure of Rb-He_{14}. In Ref. 70 this size was already identified as a closed shell, which we identify, too. Abundance ratios of next-neighboring signals were formed to identify more stable structures in this mass regime: A_n/A_{n-1}. As Cs is always contaminating Rb in our pick-up cell, ^{87}Rb should be used for this. Note, that the mass of Cs (133 amu) coincides with the one of Rb-He_{12}. The abundance ratio is displayed in Fig. 4.6. Values below 1 represent a signal decrease; values above 1 vice versa. The decrease of the snowball abundance from $n = 0$ to 14 can be identified by the abundance ratios. Also the significant drop in intensity at $n = 15$, which is connected to a shell closure, can be seen. By studying the ratios one finds a slight increase ($A_n/A_{n-1} \sim 1.1$) at $n = 12$. We interpret this as a stable structure below a shell closing, which is predicted for Na^+-He_{12} and K^+-He_{12}.[124]. No theoretical data for Rb are available, but this behavior is also similar to experimental data of Cs^+-He_{12}.

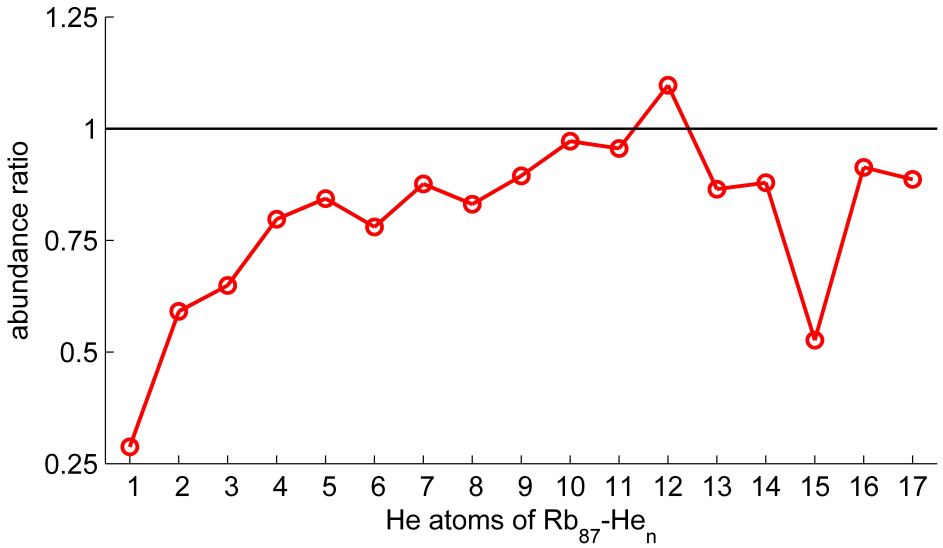

Figure 4.6.: Abundance ratio of ^{87}Rb-He$_n$: A_n/A_{n-1}. The line between the circles is to guide the eye. Signals at $n = 12$ and 14 are discussed in the text.

In conclusion, we could verify the stable structure with $n = 14$, which is most probably a He shell closing, and found another pronounced structure at $n = 12$, by monitoring the intensities of Rb$^+$-He$_n$. In Tab. 4.1 shell closings and magic numbers of different cations are presented.

4.3. Measurements of immersed Rb_n^+

The position of any positively charged ion is most preferable in the center of a He atom surrounding.[125] This is due to the inhomogeneous field, which polarizes the He atoms. As mentioned, the observation of Rb$^+$ does not help to find the ionization threshold of Rb atoms on He$_N$. Because of the highly attractive interaction between Rb$^+$ and He$_N$, the positively charged ions should therefore immerse into the droplet upon photoionization. There are mainly two reasons for the observed Rb$^+$: i) fragmented Rb clusters, ii) too much excess energy of Rb ions, which is converted into kinetic energy, so that they eject from the droplet's surface. We will call the immersed Ak$^+$ ion in the He droplet Ak$^+$-He$_N$.

The immersion of the Ak_n^+ can be monitored with a TOF mass spectrometer, whereby the high mass of the droplet itself has to be considered. In general, the electric field has too be strong enough to direct the positively charged droplet into the detector. For the detection of immersed ions the TOF is preferably used in its linear mode with rather

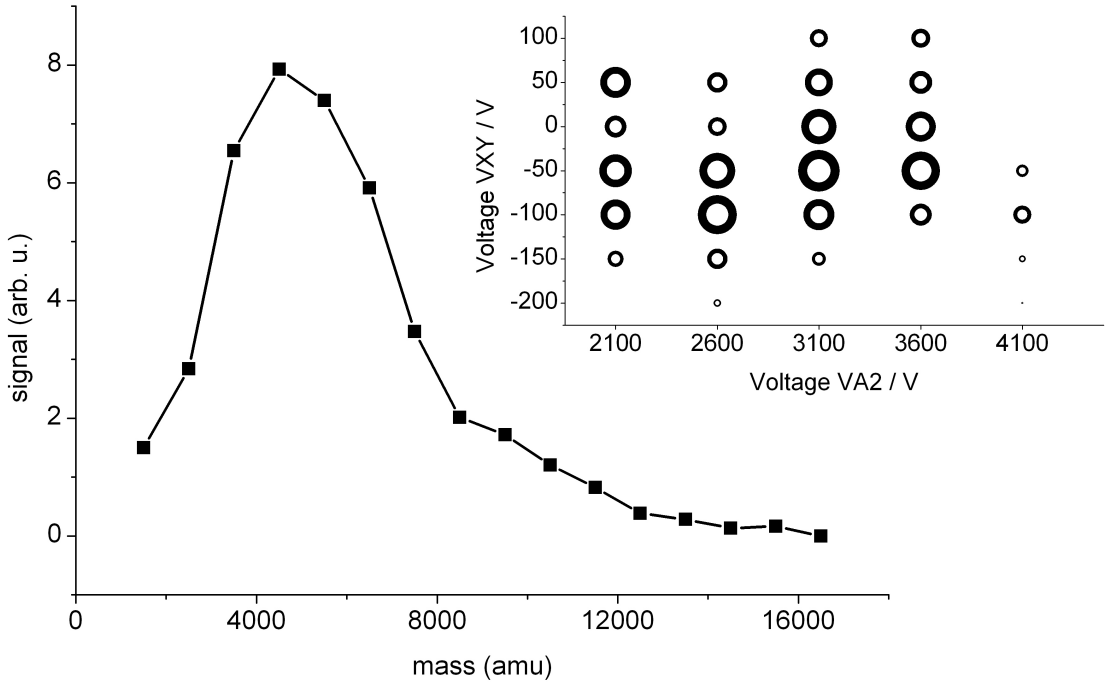

Figure 4.7.: Difference mass spectrum of photo-ionized Rb doped He droplets with a photon energy of 33587 cm^{-1}. The signals have been binned with a bin width of 1000 amu. Voltage settings are: VA2= 3100 V (extraction grid) and VXY= −50 V (acceleration field in beam direction). Inset: integrated difference signal for different voltage settings. The bubble size represents the signal strength in the range of 1000 − 15000 amu.

small initial droplet sizes (e.g. $\bar{N}_i \sim 5 \times 10^3$, $p_n = 30\,\mathrm{bar}$, $T_n = 15\,\mathrm{K}$). The calculation of optimal voltages is difficult mainly due to the size distribution of the droplets. With an one-photon ionization scheme we tested several voltage alignments to find an optimal setting (Fig. 4.7). The repeller plate voltage was kept fixed at its maximum voltage: VA1=4550 V. The voltages of the first extraction grid (VA2) and of a further electrical field, which accelerates in droplet beam direction (VXY) were varied. The signals were binned with a bin width of 1000 amu to obtain a reliable signal-to-noise ratio. From the spectra one can clearly identify a distribution similar to a log-normal distribution, which describes the He droplet size distribution under our source conditions (Fig. 4.7). Integrated signals in the range 1000 − 15000 amu measured with different voltage settings are displayed in the inset of Fig. 4.7. With our source conditions the highest ion yield in this mass regime is obtained with VA2= 3100 V (extraction grid) and VXY= −50 V.

The integrated signals were recorded at different photon energies, which are in the range of the ionization threshold of Rb atoms ($\tilde{\nu} = 33690.81\,\mathrm{cm}^{-1}$). We cannot find any significant influence of the photon energy on the Rb^+-He_N ion yield in an one-photon ionization process (Fig. 4.8). With the goal in mind to ionize single Rb atoms on the He droplet a depletion laser was used, which is placed in front of the ionizing laser. The photon energies of the depletion laser (cw, Ti:Sapphire) were set either to $12830\,\mathrm{cm}^{-1}$, which is at the maximum of the D_2 line, or to $13425\,\mathrm{cm}^{-1}$, which is a strong dimer transition of Rb_2 on He_N ($(1)^3\Pi_g \leftarrow a^3\Sigma_u^+$)[102]. In both cases excited Rb (Rb_2) will eject from the surface of the He droplet, so that less Rb-He_N (Rb_2-He_N) will enter the ionizing regime of the second laser and the ion yield should be influenced by this technique. The integrated ion signals are displayed in the inset of Fig. 4.8, where "ON" means that the depletion laser is active and "OFF" that it is inactive. One can see, that we ionize Rb_2 directly, which immerses into the droplet. The depletion laser has no influence on the monomer part, so that we use a non-destructive **R**esonance-**E**nhanced-**M**ulti-**P**hoton-**I**onization (REMPI) technique, which is described in Sec. 4.4.

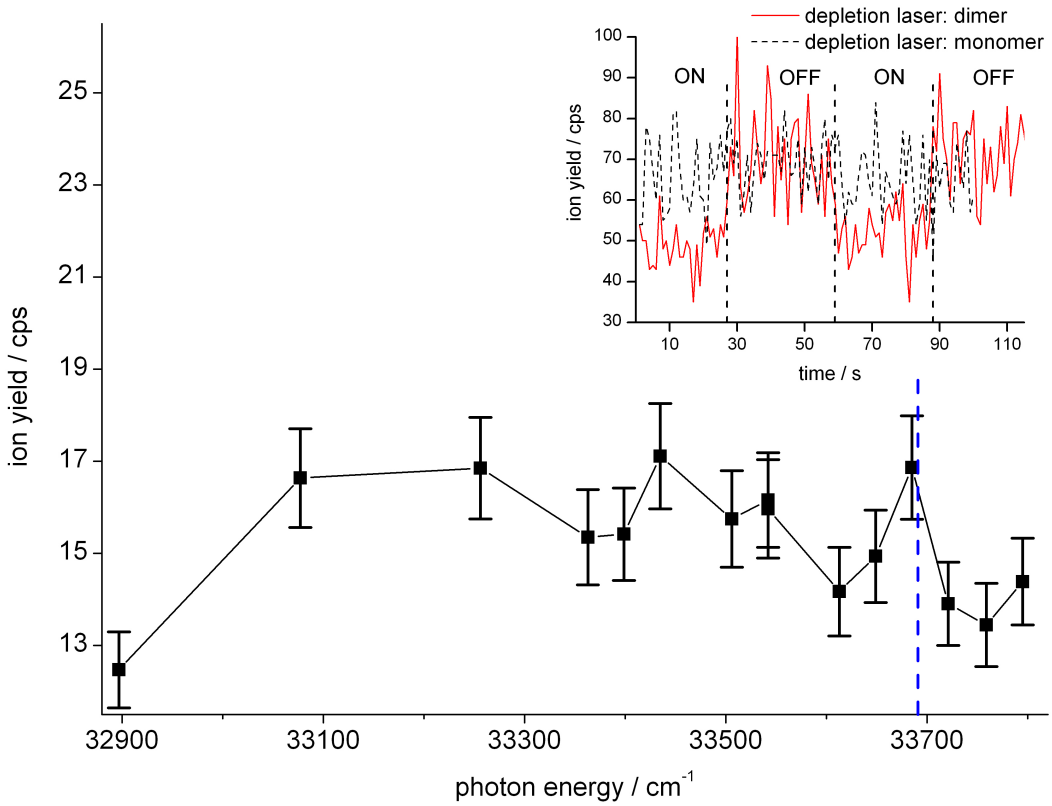

Figure 4.8.: Integrated difference signal of ionized Rb doped He droplets with masses > 1000 amu at different photon energies (the lowering of the IT due to the electrical field has been added). The vertical dashed line represents the ionization threshold of the free Rb atom. The error bars represent the standard deviation of the ion yield in our experiment. The connecting line is only to guide the eye. Inset: Integrated difference signal with/without a depletion laser set to a monomer/dimer transition. Details are explained in the text.

4.4. Forming Rb^+ snowballs in the center of He nanodroplets

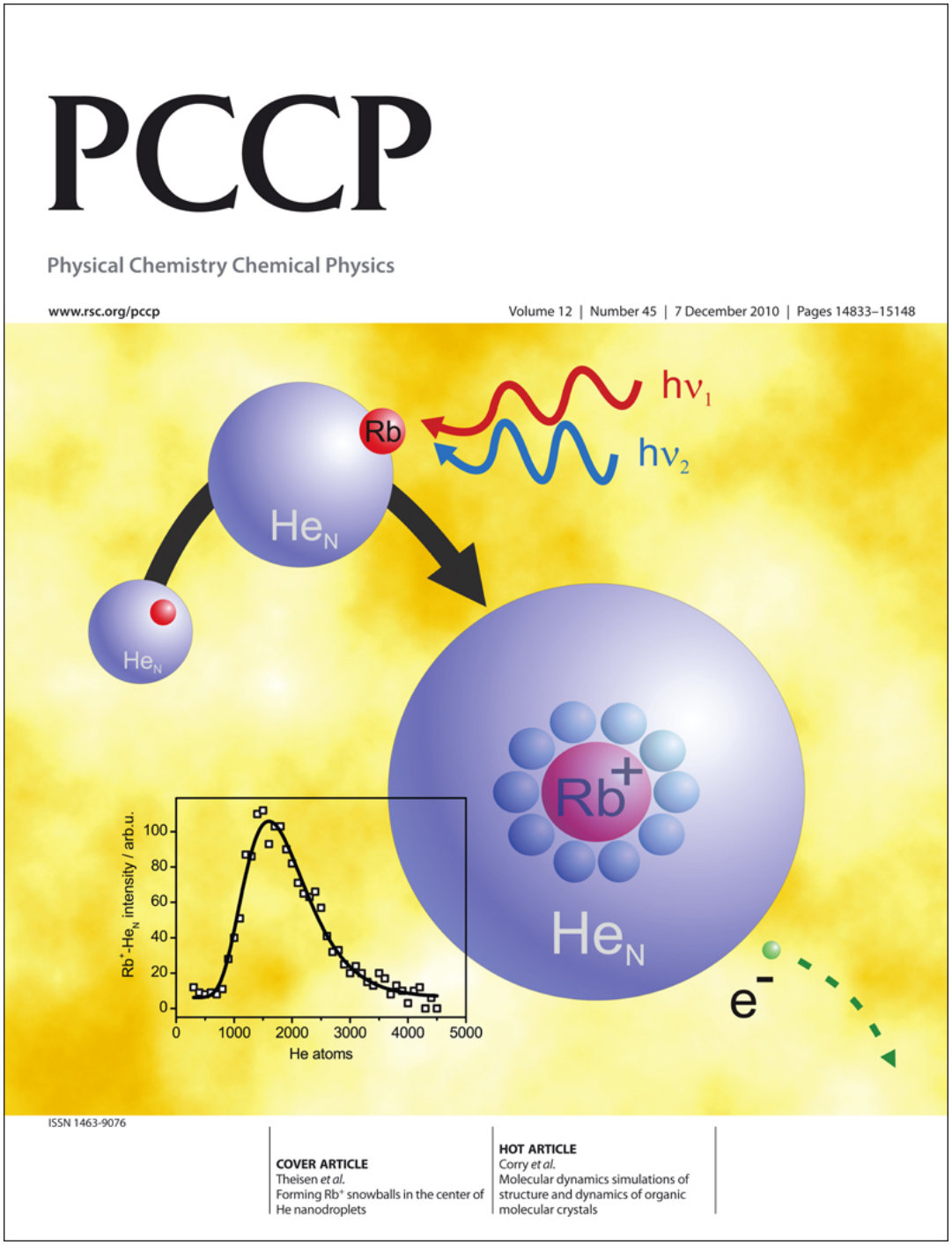

Helium nanodroplets (He_N) provide a unique matrix to isolate and study atoms or molecules in a low-temperature environment at $T = 370\,\mathrm{mK}$. Alkali-metal (Ak) atoms, such as rubidium (Rb), are an excellent probe to examine basic principles of this kind

of cluster spectroscopy. The ionization threshold as well as Rydberg states of Ak atoms lie at low energy in comparison to other atoms. Besides, the associated transition probabilities for ionization and excitation into Rydberg states are high. Moreover, Ak atoms reside on the surface of the He nanodroplet in their ground state due to a weak Vander-Waals interaction and do not migrate into the nanodroplet, as most other atoms or molecules do.[57]

Usually an Ak atom photo-detaches from the surface of the He nanodroplet upon electronic excitation; the Rb D_1-line is an exception in that the atom remains on the nanodroplet surface and relaxes back into the $5^2S_{1/2}$ state.[60] This has been exploited to achieve repeated excitations and optical pumping.[60] Here we demonstrate that this greatly enhances sequential ionization of Rb doped He nanodroplets, which leads to an immersion of the positively charged ion into the He nanodroplet.

General principles of excitation and emission spectroscopy of Ak atoms on He nanodroplets have been described in Ref. 60. In the group of Stienkemeier the ionization of Ak atoms as well as the formation of small Ak snowballs has been observed with a quadrupole mass spectrometer, which allows only to monitor small masses.[70] The nanodroplet beam apparatus used here has been described in detail in Ref. 46. In short, He nanodroplets are formed in a free-jet expansion of He gas and are afterwards doped with Rb atoms. The nanodroplet size is varied by changing the nozzle temperature ($T_N = 9 - 15\,K$), where the nozzle pressure is kept fixed ($p_N = 30\,bar$). The Rb vapor pressure was set to maximize monomer pick-up. In a first step a cw laser pumps Rb atoms either into the surface-stable $5^2P_{1/2}$ or into the $5^2P_{3/2}$ state, that desorbs from the surface of the nanodroplet. With a frequency doubled Ti:Sapphire laser of 30 ns pulse duration the excited atoms are then ionized, whereby the photon energy of the 2^{nd} laser was kept fixed at $21911\,cm^{-1}$. The photon energy of the 1^{st} laser was set to three different values, which allows to explain the different reaction products depending on the configuration of the intermediate state. The ions are detected with a time-of-flight (TOF) mass spectrometer (Jordan D-850 AREF). The He nanodroplet beam was chopped and all signals are given as difference signals, to clearly identify only ionization products coming from Ak atoms on nanodroplets.

The ionization products of Rb doped nanodroplets with an average number of $\bar{N} \approx 6 \times 10^3$ atoms ($T_N = 15\,K$, $p_N = 30\,bar$) are shown in Fig. 4.9 and Fig. 4.10.

At small masses (Fig. 4.9) Rb^+, $Rb^+{-}He_n$ with ($n < 20$) and Rb_2^+ can be identified. The signal obtained at different masses taken with different pump photon energies can be compared to each other. We observed that the Rb dimer signal does not change significantly even without the pump laser, because a two-photon one-color ionization with

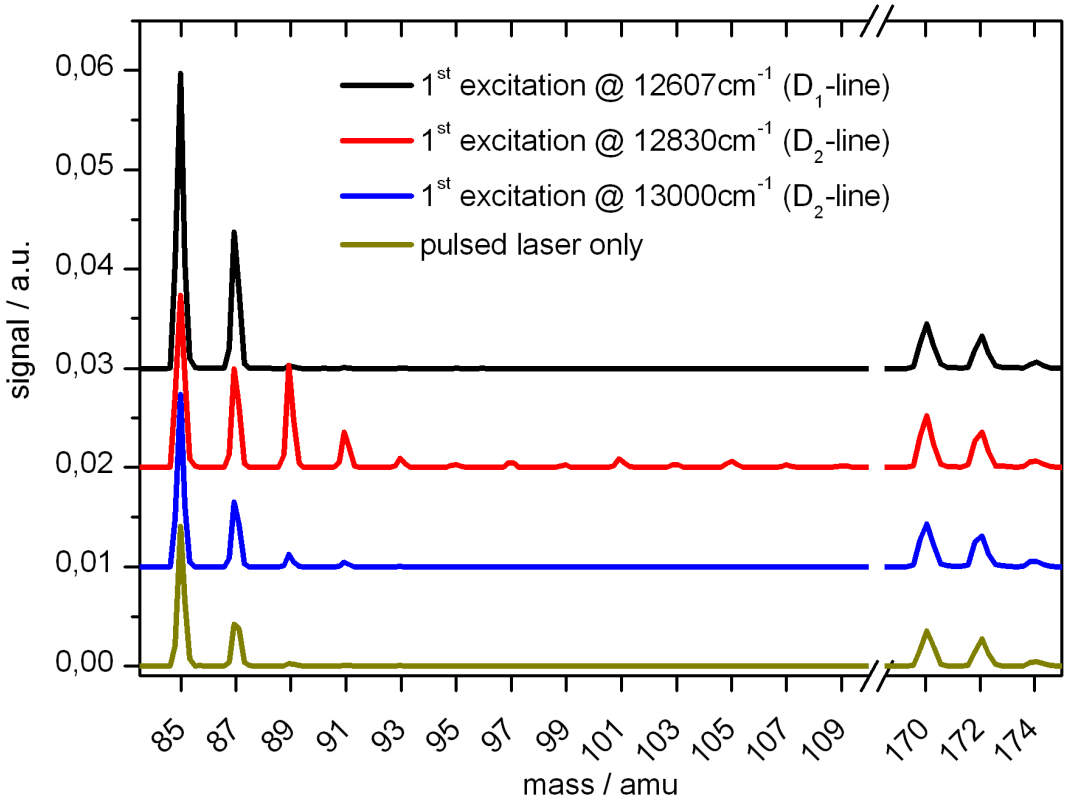

Figure 4.9.: TOF spectra in the range from 85 to 174 amu. The signals are given in counts per laser pulse of the second laser. The ionization products were monitored with three different photon energies of the first laser (12607 , 12830 , 13000 cm^{-1}) and without the first laser. Vertical offsets of 0.01 are used to better distinguish the different signals.

the probe laser only is possible. Dimers are ionized from their triplet ground state $a^3\Sigma_u^+$, which is the most stable one on He nanodroplets, resonantly enhanced by the presence of various excited states.[126] As they can fragment, also Rb^+ products can be observed. In contrast, Rb monomers in their ground state are not resonantly excited by the pulsed laser only, so that the ion yield in the lowest trace of Fig. 4.9 is attributed primarily to fragmentation products.

The formation of small Rb-He_n ($n < 20$) snowballs can be studied, too. For Rb and other Ak this has been observed experimentally in Ref. 70. Theoretical work is provided in Ref. 127. In a pseudo-diatomic model, where the He nanodroplet is treated as one giant atom and the second atom is the Ak, it is well known that three diatomic states

can be identified for ns $\rightarrow$ np transitions: $^2\Pi_{1/2}$, $^2\Pi_{3/2}$ and $^2\Sigma_{1/2}$.[60] For excitation into the $^2\Sigma_{1/2}$ state, having a maximum at $\sim 13000\,\mathrm{cm}^{-1}$ in the spectrum, exciplex formation is prevented by the repulsive character of the potential curve. At lower energies ($^2\Pi_{3/2}$, $\sim 12830\,\mathrm{cm}^{-1}$) exciplex formation is enhanced due to a minimum in the Rb-He$_n$ potential.[59] For the D_1-line transition ($^2\Pi_{1/2}$) at $\sim 12607\,\mathrm{cm}^{-1}$, where one would also expect exciplexes, the formation is prevented due to a potential barrier in the $A^2\Pi_{1/2}$ state of the Rb-He potential.[59]

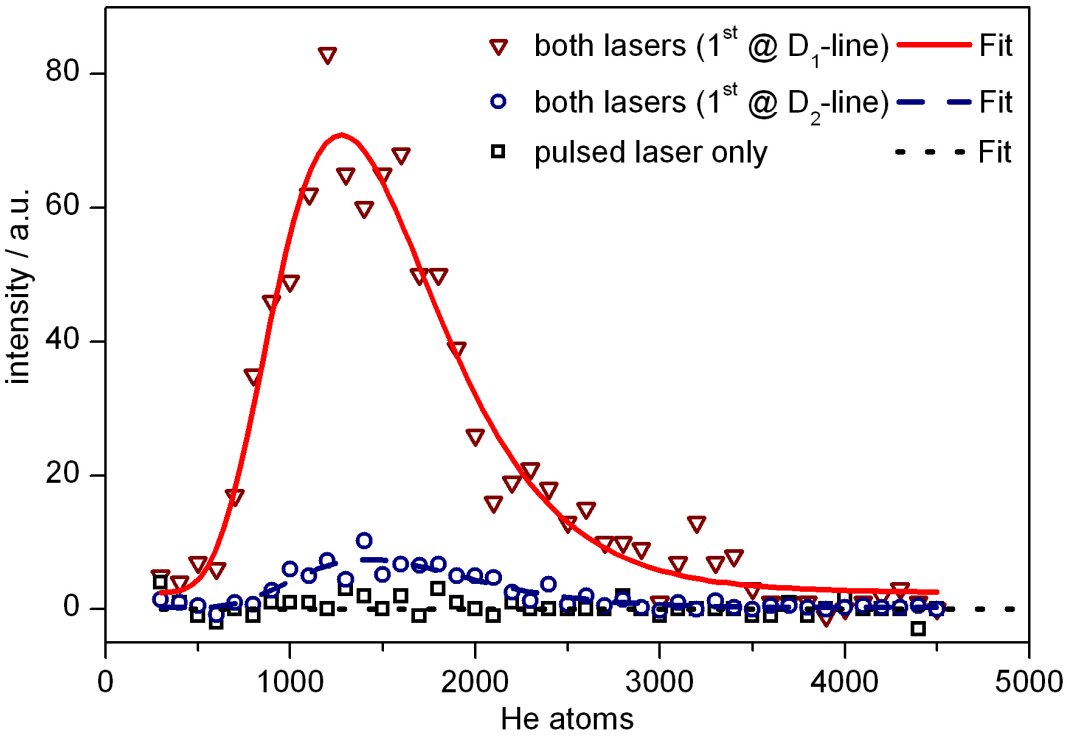

Figure 4.10.: TOF spectra in the range from 1000 to 20000 amu, where the scale is given in numbers of He atoms. The ionization products of Rb doped nanodroplets with an average number of $\bar{N}_i \approx 6 \times 10^3$ atoms ($T_\mathrm{N} = 15\,\mathrm{K}$) have been monitored with and without the first laser. The difference signals have been binned with a bin width of 250 He atoms, where the central atom number is labeled in the graph. We have fitted the signals using a lognormal function, which usually describes the size distribution of He nanodroplets.

At heavy masses (> 2000 amu) we identified large ion signals (Fig. 4.10). We can see that the formation of such ions is strictly connected to the choice of excitation energy of the first transition. As the most stable position for all ions in a He nanodroplet envi-

ronment is the center[125], the Rb atom immerses in the nanodroplet when ionized during its residence at the surface of the nanodroplet. The immersion is, therefore, greatly enhanced if an intermediate excitation into the $5^2P_{1/2}$ ($^2\Pi_{1/2}$) state is applied. The excitation of the D_2-line leads only to an immersion, if the delay time between pump and probe photon absorption is shorter than the time needed for exciplex formation, which is in the ps-range.[128] In contrast, the ionization of Rb-He_N is not resonantly enhanced, if only the pulsed laser is applied, so that no heavy ions are produced. Only excitation of Rb into the $5^2P_{1/2}$ ($^2\Pi_{1/2}$) state provides the very effective springboard for ionization through the laser pulse of 21911 cm^{-1} energy.

As the formation of He shells around Na^+ and K^+ in a He cluster has been theoretically predicted in Ref. 122, it is most likely that Rb^+ forms a snowball in the center of the He nanodroplet. The difference in estimated nanodroplet sizes and observed masses can be explained by five facts: (i) Theoretical calculations using pair-wise potentials show that the ionization threshold for Rb on He nanodroplets is close to the ionization threshold of bare Rb atoms. With an excess energy in the range of $800-1000\,cm^{-1}$ above the ionization threshold an evaporation of about 250 He atoms from the nanodroplet is expected. (ii) The binding energy between the ion and the nanodroplet is transformed into He atom evaporation. The difference in energy for an ion at the center with one near the edge of the He nanodroplets is 151 cm^{-1} as given in Ref. 125. We assume that approximately 30 He atoms will be evaporated due to this process. (iii) The snowball formation itself could also lead to He atom evaporation. According to Ref. 69 the total energy for a K^+-He_{128} is given with 23.53 K per He atom (Cs^+-He_{128}: 22.90 K). For Rb^+ no data are available. If we assume a similar energy per He atom, we deduce a further evaporation of ~ 430 He atoms. (iv) The pick-up process itself lowers the nanodroplet size by approximately 170 He atoms according to Ref. 45. (v) The sensitivity of our multi-channel-plate detector is strongly mass dependent in this regime, so that higher masses will not be recorded well. The recorded masses show therefore only the lower portion of the nanodroplet size distribution. We also note that the observed signals, shown in Fig. 4.10, 4.11, 4.12, may not reflect the actual mass distribution due to voltage limitations of our extraction field.

The Rb ion signal ($5^2S_{1/2} \rightarrow 5^2P_{1/2} \rightarrow Rb^+$) has been studied in detail for nanodroplet sizes in the range of $\bar{N}_i = 6 - 15 \times 10^3$ atoms (Fig. 4.11). Nanodroplet size $\bar{N}_i$ means the average size produced under our stagnation conditions according to the scaling laws of Ref. 29. The measured signals have been fitted with a lognormal function to assign their size distribution. The measured intensities, as well as the fits, correlate clearly with the nanodroplet size, including the mentioned reasons for the size reduction. Under all nozzle conditions given in Fig. 4.11, no ion signals at high masses were detected without the pump laser.

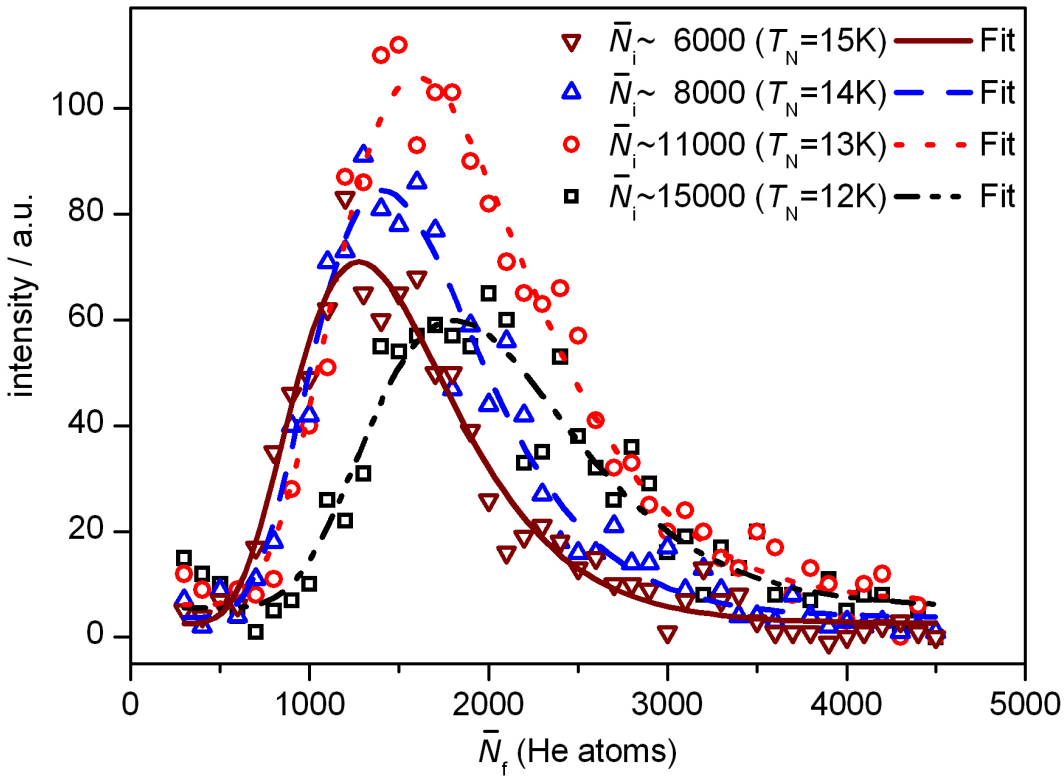

Figure 4.11.: Comparison of TOF spectra obtained with different nanodroplet sizes $\bar{N}_i$. The data are fitted with a lognormal function. The fit values for $\bar{N}_f$, given in ascending order, are 1439, 1569, 1791, 1990.

At nozzle temperatures below $\sim 11\,\mathrm{K}$ one leaves the subcritical regime for producing He nanodroplets and enters the supercritical regime, which leads to nanodroplets with average numbers of $\bar{N} = 10^5 - 10^7$ atoms.[129] In this case the two-step ionization is suppressed as the pick-up probability favors the growing of large Rb oligomers, which show bulk behavior. Besides, the subsequent pick-up of Rb atoms by the nanodroplet leads to strong evaporation of He atoms, because of the pick-up process itself and gained binding energies of the formed Rb clusters. As the ionization threshold (work function $2.1\,\mathrm{eV}$[118]) for the Rb bulk surface is below the photon energy of the pulsed laser ($2.72\,\mathrm{eV}$), one ionizes Rb bulk or large clusters directly by an one-photon process (Fig. 4.12). In this case the resulting ion has masses of $> 20000\,\mathrm{amu}$, which clearly agrees with our explanation. We note again that our detection efficiency for masses beyond 5000 He atoms is negligibly small.

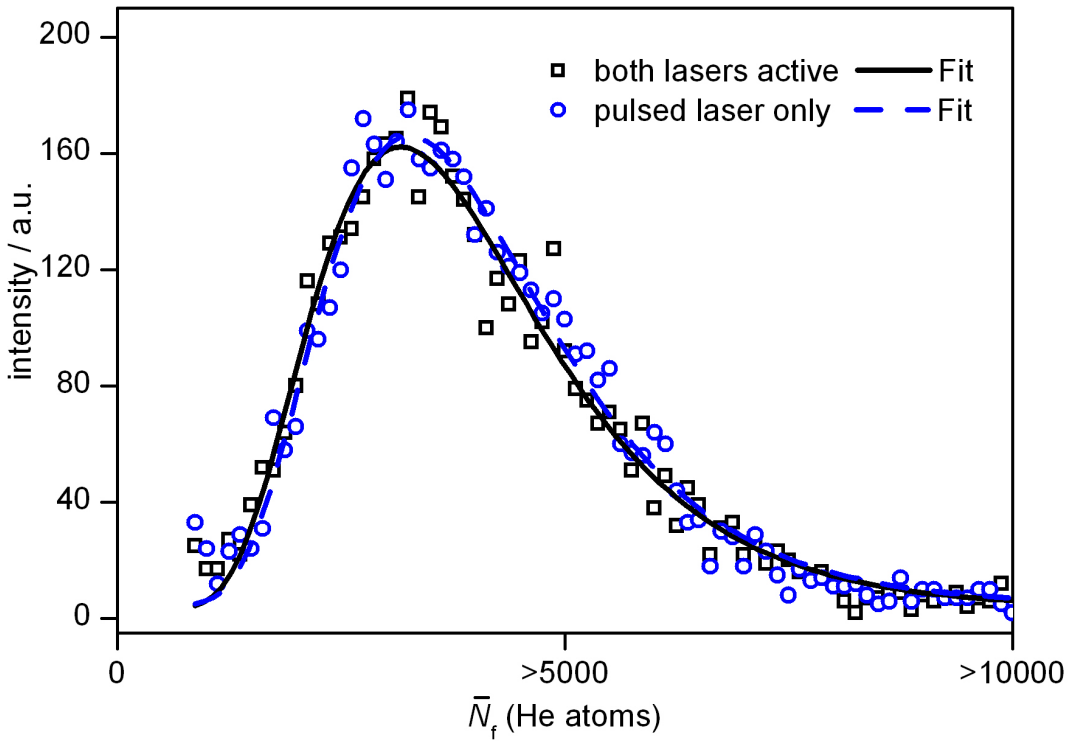

Figure 4.12.: Comparison of TOF signals with and without the pump laser, when the nanodroplets are produced in the supercritical regime ($T_N = 9\,K$). The data are fitted with a lognormal function. Beyond 20000 amu (5000 He atoms) the TOF data cannot be resolved sufficiently.

In conclusion, we have shown that by using our two-step ionization scheme Rb monomers can be selectively ionized on the surface of the nanodroplet, which leads to an immersion of the single alkali ion and most likely the formation of a snowball in the center of the He nanodroplet.

With the knowledge that a positively charge immerses into the droplet we propose an experiment with calcium (Ca), which also resides on the surface of the droplet, and single water molecules, which are inside the droplet.[130] In other words there is a barrier between two reactants. A reaction can be triggered when the Ca atom is ionized and therefore immerses, so that Ca^+ and H_2O can react.[131] The ionization can be achieved with a XeCl-laser. The probe of the reaction can be done in several ways. First, one could simply use the QMS to examine reaction products. The disadvantage would be that the electron impact ionization in front of the QMS destroys the He droplet and one could not distinguish between an ionization of the droplet which triggers the reaction or

the pure ionization of the Ca atom. Remember that the ionization of an alkaline-earth atoms leads to an Ak atom-like electronic structure. We would therefore prefer to excite the Ca^+-H_2O complex from the S0 ground state to a higher electronic state using a counter propagating laser beam. The deposited energy leads to a evaporation and a shrinking of the droplet, so that one can record the transition by the amount of droplets which reach the QMS.

5. Cesium on He nanodroplets

*Cesium (Cs) on helium droplets has been well examined experimentally and theoretically. We report the non-desorption of cesium (Cs) atoms on the surface of helium nanodroplets (He_N) in their $6^2P_{1/2}$ ($^2\Pi_{1/2}$) state upon photo-excitation as well as the immersion of Cs^+ into the He_N upon photo-ionization via the $6^2P_{1/2}$ ($^2\Pi_{1/2}$) state. Cesium atoms on the surface of helium nanodroplets are excited with a laser to their 6^2P states. We compare laser-induced fluorescence (LIF) spectra with a desorption-sensitive method (Langmuir-Taylor detection) for different excitation energies. Dispersed fluorescence spectra show a broadening of the emission spectrum only when Cs-He_N is excited with photon energies close to the atomic D_1-line, which implies an attractive character of the excited state system (Cs^*-He_N) potential energy curve. The experimental data are compared with a calculation of the potential energy curves of the Cs atom as a function of its distance R from the center of the He_N in a pseudo-diatomic model. Calculated Franck-Condon factors for emission from the $6^2P_{1/2}$ ($^2\Pi_{1/2}$) to the $6^2S_{1/2}$ ($^2\Sigma_{1/2}$) state help to explain the experimental data. The stability of the Cs^*-He_N system allows to form Cs^+ snowballs in the He_N, where we use the non-desorbing $6^2P_{1/2}$ ($^2\Pi_{1/2}$) state as a springboard for ionization in a two-step ionization scheme. Subsequent immersion of positively charged Cs ions is observed in time-of-flight mass spectra, where masses up to several thousand amu were monitored. Only ionization via the $6^2P_{1/2}$ ($^2\Pi_{1/2}$) state gives rise to a very high yield of immersed Cs^+ in contrast to an ionization scheme via the $6^2P_{3/2}$ ($^2\Pi_{3/2}$) state. At the other end of the mass scale one can study small Cs^+-He_n ($n = 1-56$) and Cs_2^+-He_m ($m = 1-23$) complexes, too. When resonant two-photon ionization is applied to cesium dimers on He droplets, Cs_2^+-He_N aggregates are observed in time-of-flight mass spectra. Most results of this chapter have been published in J. Chem. Phys. **135** (2011), 074306 (Ref. 4).*

5.1. Introduction

Ion-induced electrostatic effects are of interest in several fields of physics, biology and chemistry.[132,133] Positively charged ions embedded in superfluid helium (He) enhance the

density of the He surrounding around the ion.[65,69] Locally the He density may exceed the crystallization limit, so that the He atoms form solid shells around the impurity and the complex can be called *snowball*.[119] On the other hand, alkali-metal (Ak) atoms, such as cesium (Cs) studied here, play a key role in fundamental research as their excited electronic states as well as their ionization threshold is rather low, which makes them easily accessible for spectroscopic investigations. As one-electron systems they are rather easy to model, too.

Helium nanodroplets (He_N) have been well established as a spectroscopic matrix for studying properties of atoms, molecules, and clusters in a superfluid environment at low temperature ($T = 370\,\mathrm{mK}$). Fundamental principles of this kind of spectroscopy can be found in Refs. 26,78.

This chapter contains two complementary parts about Cs atoms on He nanodroplets:

1. The re-examination of the D_1- and D_2-line of Cs atoms on the surface of He nanodroplets with special respect to the stability of the excited state system: Cs^*-He_N, meaning the non-desorption of the Cs atom from the surface (* indicates an excited state).

2. The formation of Cs^+ and their subsequent immersion into a He_N, an indication of forming He around the Cs^+ ion, as well as preferred Cs^+-He_n and Cs_2^+-He_m structures.

The stability of the Cs-He_N system in its first excited state can be also used as a springboard in the systematic observation of Rydberg states.[5] Here, the two-step ionization scheme has been first applied and we have monitored the immersion of Cs atoms after ionization, where snowball complexes in the He nanodroplet are most probably formed. Forming Cs ion-molecule complexes inside the helium nanodroplets, which can be probed downstream by spectroscopy, may give new insight into fundamental electrostatic effects in a nanosized superfluid environment.

When picked up, Ak atoms remain on the surface of a He_N and create a dimple, which is unlike most other complexes, that move inside the nanodroplet. When electronically excited, Ak atoms usually detach from the surface of the He_N. Until now, only the excitation into the $5^2P_{1/2}$ ($^2\Pi_{1/2}$) state (D_1-line) of Rb monomers with certain photon energies is known as an exception from this rule.[60] This has been used for optical pumping experiments[60], stepwise excitations[1], ionization experiments[2], and is also an important ingredient for electron spin resonance spectroscopy on He_N.[134]

Excitation of Cs on He nanodroplets followed by its detachment was observed in an earlier work, where it was argued that Cs atoms form exciplexes with helium, which detach from the He nanodroplet, after electronic excitation to the $6^2P_{1/2}$ ($^2\Pi_{1/2}$) state.[135] Also, simulations were presented, where the $6^2P_{1/2}$ ($^2\Pi_{1/2}$) potential of Cs*-He_N has a strictly repulsive character.[136] In contrast to Rb atoms on He_N,[59] no fluorescence spectra were available for the $6^2P_{1/2}$ ($^2\Pi_{1/2}$) $\rightarrow$ $6^2S_{1/2}$ ($^2\Sigma_{1/2}$) transition of Cs. In this work, we show that Cs behaves like Rb, i.e. different from the lighter Ak atoms sodium (Na) and potassium (K).

The formation of snowballs has been studied in various experiments. For Ak^+ (Na, K, Rb, Cs) ions small snowballs (Ak^+-He_n) with a first He shell closure were studied in Ref. 70. The observation of large Rb^+-He_N aggregates ($N > 1000$) with Rb^+ in a He snowball configuration inside a He nanodroplet was recently reported.[2] Other materials like silver (Ag) or magnesium (Mg) have been examined, too. E.g. for Ag^+-He_n a 1st shell closure appears at $n = 10, 12$ and a 2nd closure at $n = 32, 44$.[71] Theoretical aspects concentrating on Ak^+-He_n can be found in several works, e.g. Refs. 62,65,66,122,123,127,137. One of the main theoretical findings is the layer-like He density concentration around Ak ions. For Cs, theoretically at least two layers are characterized by an increase in He density.[65,69]

A special feature of the non-desorption, demonstrated in this work, allows to excite or ionize Cs monomers selectively without addressing nanodroplets with oligomers, which are always present. Our results of monomer-selective ionization experiments indicate strong electrostatic effects between the He nanodroplet and the Cs^+ ion as well as an immersion of the Cs^+ into the He nanodroplet.

The chapter is organized as follows. In Sec. 5.2, we present briefly the experimental set-up. In Sec. 5.3, we demonstrate that a large fraction of excited Cs atoms in their $6^2P_{1/2}$ ($^2\Pi_{1/2}$) state does not desorb from the surface of the droplet. This allows us to demonstrate a stepwise ionization for this species (Sec. 5.4), where we observe the immersion of Cs^+ into the He nanodroplet, most probably with a subsequent formation of snowballs. In Sec. 5.5 we briefly explain the theoretical approach for modeling Ak-He_N potential energy curves. For the sake of convenience we use two different notations to label the electronic states of the Cs atom, as described in previous papers.[1,61] Shortly, the first one is that of the bare atom in the LS coupling scheme (e.g. $6^2P_{1/2}$, $6^2P_{3/2}$); the droplet is treated as a perturbation and also defines the quantization axis, normal to the droplet surface. The second notation is that of a diatomic molecule, where the whole He nanodroplet is treated as a fictitious atom; in this notation we use Hund's *case a* (e.g. $^2\Pi_{1/2}$, $^2\Pi_{3/2}$, $^2\Sigma_{1/2}$). This notation is used for the sake of consistency among all Ak-He_N systems. For specific calculations, one has to use the appropriate Hund's

case that applies to the corresponding states, i.e. depending on the size of the spin-orbit coupling.

5.2. Experimental

He nanodroplets are created using our droplet beam apparatus, which has been described in Chap. 2. General principles of excitation and emission spectroscopy of Ak atoms on He_N can be found in several works (e.g. Refs. 57,59,60). In brief, He nanodroplets are formed in a free-jet expansion of He gas.[26] They are doped by flying through Cs vapor in a heated pick-up cell. In the current experiments monomer pick-up was maximized by keeping the temperature at a rather low value ($\sim$ 370 K), which allows to mainly observe Cs monomers as the probability of picking up two or more Cs atoms is kept low.

Here, $6^2P \leftarrow 6^2S$ transitions and the ionization of Cs atoms attached to He droplets are examined using different methods (LIF, CCD, BD, TOF) and lasers (L1, L2).

Four different detection schemes, placed in series along the He nanodroplet beam axis, were used:

1. Excitation spectra monitored by laser-induced fluorescence (LIF): LIF spectra are measured in the interaction zone between laser and He_N beam by recording the fluorescence light with a Peltier-cooled photomultiplier tube (PMT, housing: Product for Research, TE210TS-RF; tube: Hamamatsu R943-01 with GaAs photocathode). The sensitivity of this PMT strongly decreases below $\sim 11600\,cm^{-1}$ and cuts off at $\sim 11100\,cm^{-1}$. In order to obtain reliable excitation signals the recorded data have been corrected by the wavelength-dependent sensitivity provided by the manufacturer. For lack of knowledge of emission wavelengths we use the excitation wavelengths, which provide no significant mistake as the emission of exciplexes is redshifted (weaker signal at our PMT).

2. Emission spectra: a grating spectrograph (McPherson EU-700) in combination with a CCD-camera (LOT-Andor iDUS DU401A BR-DD) is used to monitor fluorescence spectra of Cs monomers upon excitation.

3. Beam depletion (BD) spectra: a Langmuir-Tailor surface ionization detector is used for measuring the amount of Cs atoms transported by the He nanodroplet beam.[77] The signal decreases due to the desorption of Ak atoms, which usually happens by exciting Ak atoms into higher electronic states as they are only weakly bound to the surface of He nanodroplets ($\sim 10\,cm^{-1}$). The BD signals were recorded with a lock-in-amplifier (Stanford Research SR510).

4. Time-of-flight (TOF) mass spectra: photo-ionized complexes are detected with a time-of-flight (TOF) mass spectrometer (Jordan D-850 AREF).

For photo-excitation and -ionization two lasers (L1, L2) are applied:

1. L1 is a continuous wave (cw) Ti:Sapphire laser (Coherent 899-01) with a maximum power of $\sim 2.5\,\mathrm{W}$.

2. L2 is a frequency-doubled tunable pulsed Ti:Sapphire laser (Coherent Indigo S, repetition rate 5 kHz, pulse duration 30 ns) and is used with fixed photon energies of 22100 and 22204 cm^{-1} (pulse energy $\sim 55\,\mu\mathrm{J}$) in ionization experiments only.

Measurements of D_1- and D_2-lines (LIF, emission, BD) provided in Sec. 5.3 were performed with L1 only. For measurements (TOF) in Sec. 5.4 we used L1 for pumping the $6^2P_{1/2}$ ($^2\Pi_{1/2}$) state (1st excitation) and L2 for the ionization from this state or L2 only to examine Cs^+-He_n complexes at low masses.

5.3. Non-desorption of Cs monomers in their $6^2P_{1/2}$ ($^2\Pi_{1/2}$) state on He droplets

In the case of Rb-He_N no desorption at excitation energies near the $5^2P_{1/2}$ ($^2\Pi_{1/2}$) $\leftarrow$ $5^2S_{1/2}$ ($^2\Sigma_{1/2}$) transition takes place and further excitation is possible.[1,60] The results displayed in Figs. 5.2, 5.3, and 5.4 will show that Cs atoms on He_N exhibit the same behavior.

We compare the LIF signals at different laser powers (20, 600, 1500 mW) in Fig. 5.2. To see saturation effects, the signals are scaled to the height of the D_1-line. The excitation line shape can best be judged at 20 mW power, because saturation effects should not occur. The D_1-line appears as a single peak (**a**) with an asymmetric profile (Fig. 5.2). The D_2-line has a double-peak structure (peaks **b** and **c**), which is similar to mass-resolved photoionization and LIF spectra of Bünermann *et al.*[135] (Fig. 5.1). This structure can be well explained with a pseudo-diatomic model with three diatomic states: $^2\Pi_{1/2}$, $^2\Pi_{3/2}$, and $^2\Sigma_{1/2}$.[57]

By increasing the laser power, the relative amplitude of the D_2-line decreases compared to the one of the D_1-line. Also the double-peak structure of the D_2-line vanishes. By forming exciplexes, which is mostly the case for the second peak of the D_2-line (peak **c**), fluorescence light is strongly redshifted,[135] so that it is neither possible to record this in full nor to evaluate its intensity with our PMT. This redshift has been also observed for other Ak atoms, like Rb.[59] The monitored power dependent-behavior

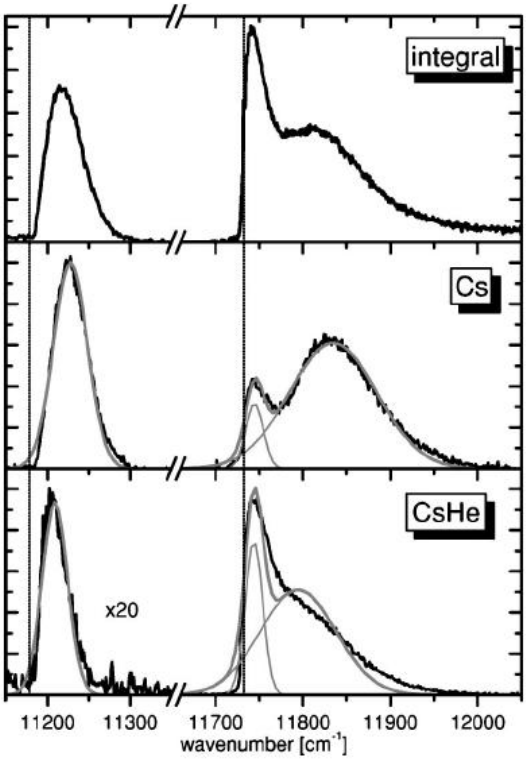

Figure 5.1.: Photoionization spectra of Cs-doped He droplets taken from Ref. 135. The top panel represents the integrated spectrum, meaning the non mass-selective. The lower panels give the intensities of Cs and CsHe. Gaussian fits have been applied by Bünermann *et al.* to the peaks (gray) in order to show the diatomic structure and to explain the different ionization products at different excitation energies.

is an indication for multiple excitation-emission processes, when excited at the D_1-line.[60]

To explain this we also monitored beam depletion. A comparison of both measurements is plotted in Fig. 5.3. The depletion signal has been scaled to the height of the LIF signal on the blue side of the D_1-line ($\sim 11280\,\mathrm{cm}^{-1}$), where direct desorption of Cs atoms and no exciplex formation is expected.[59,135] In the range of the D_2-line also dimer and trimer transitions are present,[135] which should show shifted emission spectra. Therefore LIF and BD behave differently beyond $11730\,\mathrm{cm}^{-1}$.

At low excitation energies ($\sim 11200\,\mathrm{cm}^{-1}$) there is a strong difference between both signals. As fluorescence light is emitted at those excitation energies Cs monomers have to be excited into their $6^2P_{1/2}$ ($^2\Pi_{1/2}$) state. On the other hand no depletion can be observed, meaning that the Cs monomer does not desorb from the surface of the He nanodroplet. At higher excitation energies both methods show a similar behavior, meaning

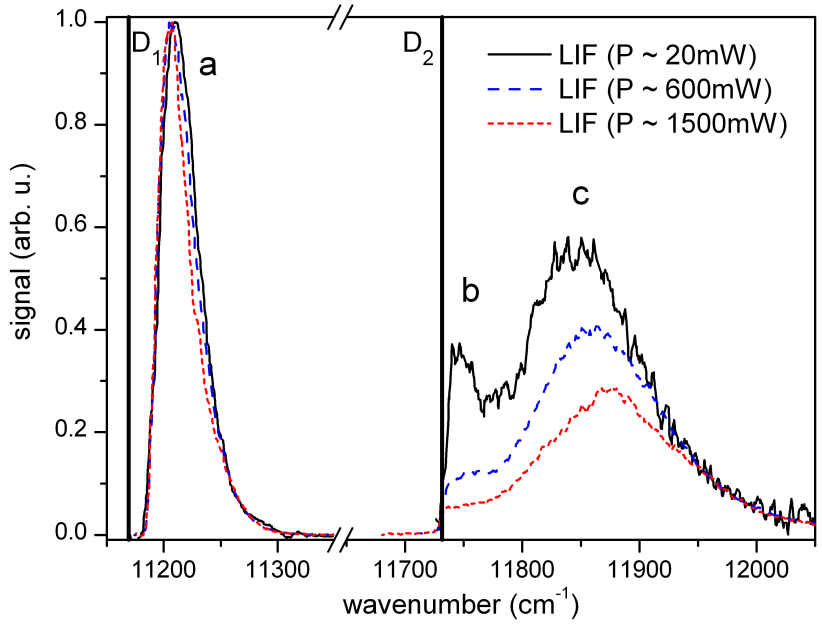

Figure 5.2.: LIF signal of the D_1- and D_2-lines with different laser powers. The signals are scaled to the height of peak **a** and smoothed. The vertical lines show the $6^2P_{1/2,3/2} \leftarrow 6^2S_{1/2}$ transitions of the bare atom. Features **a**, **b** and **c** are discussed in the text.

that the Cs monomer is ejected. The number of excitation-emission cycles on the He_N is limited, however, as also the ratio of the LIF signal amplitudes of D_1- and D_2-lines increases non-linearly with the laser power. We interpret this as a recycling process similar to the one observed for Rb.[60] The same Cs monomer can be excited several times without desorbing from the nanodroplet, which also explains the different ratios of the signals (Fig. 5.2).

The consequences of non-desorption can be further investigated by recording dispersed fluorescence spectra (Fig. 5.4) as it was done for Rb-He_N.[60] At the maximum of the BD signal ($\sim 11240\,\mathrm{cm}^{-1}$) atomic desorption is expected. The atomic line emission appears broadened only due to the instrumental limitations. At lower excitation energies ($\sim 11200\,\mathrm{cm}^{-1}$), where no depletion takes place, the emission line is significantly broader. This is similar to the case of Rb[60] and agrees well with our explanation, where emission from Cs atoms bound to the nanodroplet is expected. The excitation into the $6^2P_{1/2}$ ($^2\Pi_{1/2}$) state implies a new equilibrium density distribution of helium. The decay from the excited state into the ground state, with the Cs atom fully attached to the nanodroplet's surface, leads to a redshift of the emission wavenumbers. In the pseudo-diatomic model this goes along with an emission from the vibronic ground state $v' = 0$

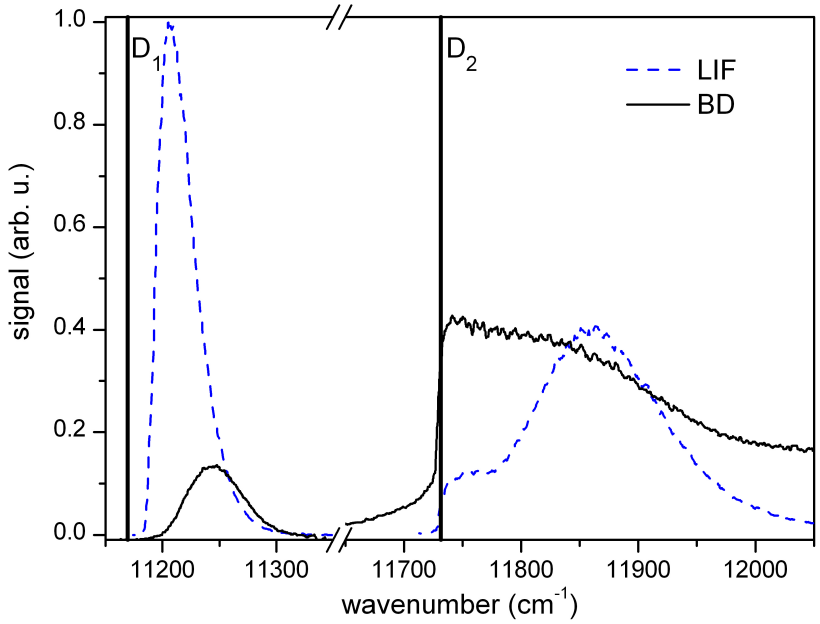

Figure 5.3.: Comparison of excitation LIF and beam depletion (BD) spectra @ 600 mW. The vertical lines show the $6^2P_{1/2,3/2} \leftarrow 6^2S_{1/2}$ transitions of the bare atom. The difference of the peak maxima @ the $6^2P_{1/2}$ ($^2\Pi_{1/2}$) state in the LIF and BD spectrum shows the non-desorbing character of this state when excited with certain photon energies.

of the Cs*-He_N excited state ($6^2P_{1/2}$ ($^2\Pi_{1/2}$)) into several vibrational levels v'' of the Cs-He_N ground state ($6^2S_{1/2}$ ($^2\Sigma_{1/2}$)).

The emission from the Cs atom on the He droplet only differs slightly from the one from the free Cs atom. The small perturbation by the droplet is much less than the spin-orbit splitting of the 6^2P state manifold. The electronic wavefunction can then be described with a Hund's *case c* coupling scheme. Orbital angular momentum L and spin S are coupled to form the total angular momentum J, whose projection on the molecular axis in a pseudo-diatomic model gives Ω. For the relevant state ($L = 1$, $S = 1/2$, $J = 1/2$, $\Omega = 1/2$) the corresponding diatomic CsHe potential energy curve is then given by $V_{|1/2\rangle} = c_\Pi^2 V_\Pi + c_\Sigma^2 V_\Sigma$ with $c_\Pi = -\sqrt{2/3}$ and $c_\Sigma = \sqrt{1/3}$,[96] where we use Pascale's diatomic CsHe potential energy curves for V_Π and V_Σ.[138] $V_{|1/2\rangle}$ is used as an external potential for the calculation of the equilibrium density distribution in DFT calculation. The potential energy curves of the Cs*-He_N system (N=1000) as a function of the distance R between the nanodroplet's center of mass and the position of the Cs atom have been calculated using the DFT code by F. Dalfovo[139] modified by R. Schmied.[140] SO-coupling for the 6^2P states was included in analogy to Takami and

co-workers[106] and Reho *et al.*[100]

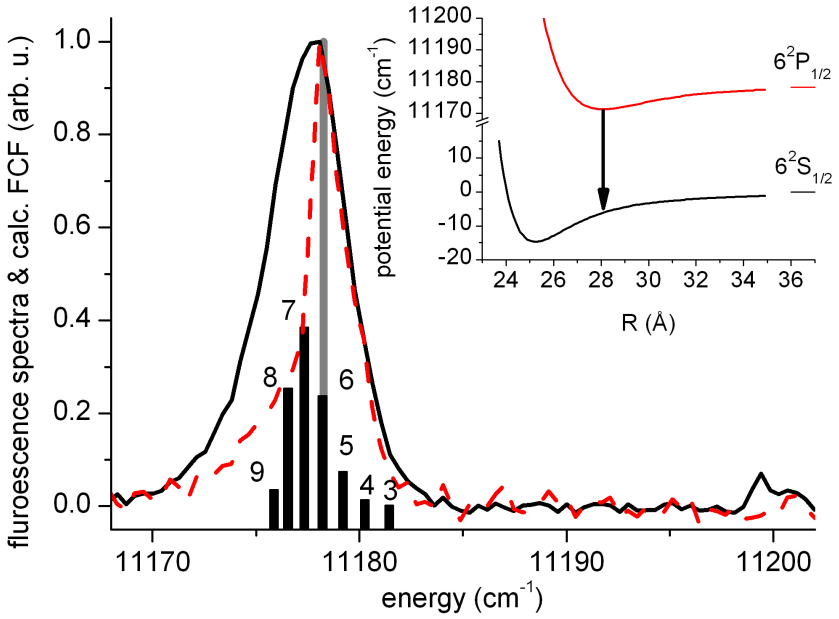

Figure 5.4.: Fluorescence spectra of Cs-He_N at different excitation energies recorded with a laser power of 1500 mW. At photon energies of 11240 cm^{-1} Cs desorbs from the nanodroplet so that atomic fluorescence is observed (red dotted line). At lower photon energies (11200 cm^{-1}) a broader spectrum is monitored, which shows the non-desorbing character (full black line). The black bars show simulated Franck-Condon factors for emission using the LEVEL 8.0 code[141], where the numbers indicate the vibronic levels v'' of the $6^2S_{1/2}$ ($^2\Sigma_{1/2}$) ground state in the pseudo-diatomic model. The vertical gray bar represents the atomic transition $6^2P_{1/2} \rightarrow 6^2S_{1/2}$. Inset: Potential curves of Cs-He_{1000} for different states of Cs. R(Å) is the distance between the center of the nanodroplet and the bare atom. Details of the calculation are given in the text.

Our measurements can be compared with earlier ones from Bünermann *et al.* in Ref. 135, where direct desorption (peak maximum at 11228 cm^{-1}, FWHM 48 cm^{-1}, relative amplitude 1.00) as well as Cs-He exciplex formation (11209 cm^{-1}, 37 cm^{-1}, 0.06) occurs for the Cs D_1-line. After exciplex formation energy is released that causes desorption. This energy release is more than the photon excess energy. For Rb, there is a potential barrier along the $A^2\Pi_{1/2}$ Rb-He potential, so that exciplex formation is foreclosed at small photon excess energies and therefore Rb stays on the surface of the nanodroplet[59,60,100]. As mentioned, for Cs the situation was believed to be different[135], but it was also recognized that the relative amplitudes differ strongly (1.00 to 0.06), which makes exciplex formation unlikely.

Theoretical considerations underline that exciplex formation is improbable. The formation of exciplexes is strictly connected to the potential Cs*-He. The potential barrier in the $A^2\Pi_{1/2}$ state[142–144] has to be overcome to form exciplexes. The barrier height is given as 75 [142] and $\sim 100\,\mathrm{cm}^{-1}$,[144] which can be compared with our measurements. The free atom level is given as $\sim 11178\,\mathrm{cm}^{-1}$) and the binding energy between Cs in its ground state and the He droplet is $\sim 20\,\mathrm{cm}^{-1}$. The Cs atoms begin to eject from the He droplet at excitation energies above $\sim 11200\,\mathrm{cm}^{-1}$, which equals an excess energy of $\sim 42\,\mathrm{cm}^{-1}$ and is lower than the calculated barrier, which prevents exciplex formation. A further investigation would need the discrimination of ejected Cs* atoms from exciplexes. In summary, we conclude from our comparison of LIF and BD measurements that Cs monomers remain on the surface when excited close to the D_1-line of the bare atom, which lets us anticipate excellent chances for stepwise ionization measurements (Sec. 5.4).

5.4. Cs^+ snowballs in He nanodroplets

The non-desorption of the Cs $6^2P_{1/2}$ ($^2\Pi_{1/2}$) state opens the possibility to study the formation of monomer-selective ionization products with a high-yield of Cs^+-He_N complexes.

In our studies, we focused on various aspects: i) Cs^+-He_N formation was investigated for different initial He_N average sizes. ii) Peak intensities in the mass range $133-358$ amu were monitored in detail to study caging effects. There we find Cs^+-He_n (Cs_2^+-He_m) of sizes at least up to $n = 56$ ($m = 23$).

In total, three different laser configurations were used: both lasers (1st @ D_1-line, 2nd ionizing), both lasers (1st @ D_2-line, 2nd ionizing), pulsed laser only.

At small masses (< 500 amu) we can identify small Cs^+-He_n products in a single pulsed laser configuration, as they were detected earlier in Ref. 70 with sizes up to $n = 39$. Here, we see sizes up to $n = 56$ (Fig. 5.5). Besides Cs^+-He_n related signals we also identify dimer products Cs_2^+-He_m as well as water related products: Cs^+H_2O, $Cs(CsH)^+$, $Cs(CsOH)^+$.[37] By systematical examination of abundance ratios for neighboring snowball intensities: I_n/I_{n-1} (not shown), one can identify He shell closures as dips. A first shell closure of He_n around Cs^+ with $n = 17-18$ was theoretically predicted by Rossi *et al.*[65], who propose a solid-like structure, and experimentally confirmed by Müller *et al.*[70] with a similar number of n. More shell closures at higher n might be ex-

pected, even if they are of fluctuating character and not solid-like[65]. Calculated second shell closures are given with 21 (28, 32) in the case of Li^+ (Na^+, K^+).[62] Recently published calculations speak of 32 He atoms in the case of Na^+,[69] while for Cs^+ no number is available. Another deviation from a smooth n-dependence of the photoion yield is observed around $n = 50$ and extends over a larger range of He atoms. This points towards a second shell closure that may not be rigid and the exact number of He atoms fluctuates more easily in this case. This is in agreement with Ref. 69. Besides these signatures we do not find any other deviation from a smooth mass number distribution for Cs^+-He_n.

We can further identify a preferred Cs_2^+-He_m structure at $m = 8$ (Fig. 5.6). Theoretical findings expect preferred structures of Ak_2^+-He_m for Li: $6, 14, 16, 18$ (Na: $6, 20$, K: $6, 12, 17, 24$).[64] Observed signals at masses 282 and 283 amu belong to Cs_2^+-He_4 and $Cs(CsOH)^+$ (not shown). As the photo-ion yield of $Cs(CsOH)^+$ is $\sim 10\times$larger than the one of Cs_2^+-He_4 we cannot separate both peaks seriously and do not want to speculate about a preferred structure of Cs_2^+-He_m in this case.

By applying the additional laser for the two-step scheme (1st @ D_1-line, 2nd ionizing) we only see a significant difference in the signal at 133 amu. With L1 at 11197 cm^{-1}, no exciplexes are formed and only additional pure Cs^+ is detected (not shown).

At heavy masses (> 2000 amu) we identify large ion signals for all three different laser configurations (Fig. 5.7a). We can see that the formation of these ions is strictly related to the presence of L1 and to the choice of excitation energy of the first step (that is, whether L1 excites the atoms from the ground state into the $^2\Pi_{1/2}$, $^2\Pi_{3/2}$, or $^2\Sigma_{1/2}$ state). As the most stable position for all ions in a He nanodroplet environment is its center[125], the Cs atom immerses in the nanodroplet when ionized during its residence at the surface of the nanodroplet. The immersion is, therefore, greatly enhanced if an intermediate excitation into the non-desorbing $6^2P_{1/2}$ ($^2\Pi_{1/2}$) state is applied. Because the chosen photon-energy of the pulsed laser L2 can also lead to a resonant excitation of a dimer state[145] and a monomer state close to the $7^2P_{3/2}$ state of the bare Cs atom[61], the immersion of Cs_2^+ and Cs^+ in a pulsed laser configuration only can also be observed (Fig. 5.7a). We obtain the selective monomer signals as the difference between the signals with and without the cw "first-step laser" (Fig. 5.7b). Note, Cs dimers are ionized by a resonant two-photon ionization (R2PI) scheme with the pulsed laser only, so they tend to form snowball-like structures in the interior of a He nanodroplet, too. Only excitation of Cs with the first laser L1 into the $6^2P_{1/2}$ ($^2\Pi_{1/2}$) state provides the very effective springboard for ionization of the large Cs^+-He_N complex through the laser pulse of L2.

Theoretical calculations show a formation of He shells around Na^+ and K^+ in a super-

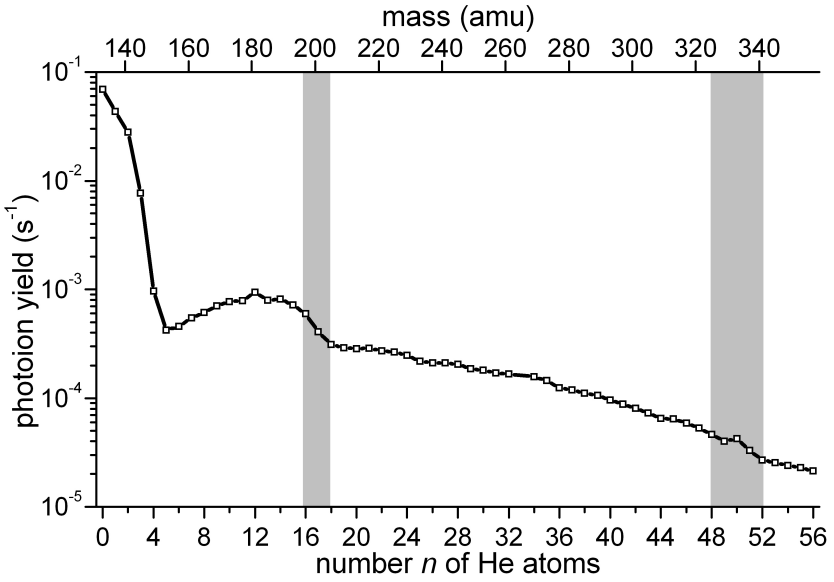

Figure 5.5.: Cs^+-He_n products of Cs doped He nanodroplets with an initial size of $\bar{N}_i \sim 15000$ He atoms for the pulsed laser only configuration (photon energy $22100\,cm^{-1}$). The bottom (top) abscissa scale is given in numbers of He atoms (amu). The time-of-flight mass spectrum has been fitted with a gaussian distribution. The given signal of Cs^+-He_n products corresponds to the area of each peak. The black line serves only to guide the eye. Drops and increases in the intensity at $n = 17 - 18$ and around $n = 50$ are marked by gray bars and indicate shell closures of He atoms.

fluid He environment[122]. Another theoretical study on Na-ion doped He clusters (Na^+-He_N) finds a triple-layer structure for $N \geq 100$ at low temperatures ($T \leq 1\,K$).[66] Earlier theoretical findings of Reatto and co-workers indicate a fluctuating structure in the case of Li^+ and Cs^+, as they readily exchange with the He surrounding.[62] More recent calculations of this group show a first solid-like shell for Cs^+ with $n = 17$ or 18,[65,69] which seems to be experimentally verified.[70] The formation of solid-like Ak^+-He_n snowballs surrounded by a liquid-like environment is theoretically predicted by Coccia *et al.*[123] As result of our experiments, we consider most likely that Cs^+ forms an one-layer snowball in the He nanodroplet with surrounding fluctuating layers.

Determined by our source conditions, the initial average nanodroplet size for the results depicted in Fig. 5.7 is $\bar{N}_i \sim 8000$ He atoms.[29] The difference in estimated initial nanodroplet sizes $\bar{N}_i$ and observed masses can be explained by two facts: (i) nanodroplet size reduction due to evaporation and (ii) an instrumental function, which we will discuss both. (i) The energy levels of Rydberg states at the surface of liquid He are shifted only by a small amount.[111] Therefore the ionization threshold for Cs on He nanodroplets

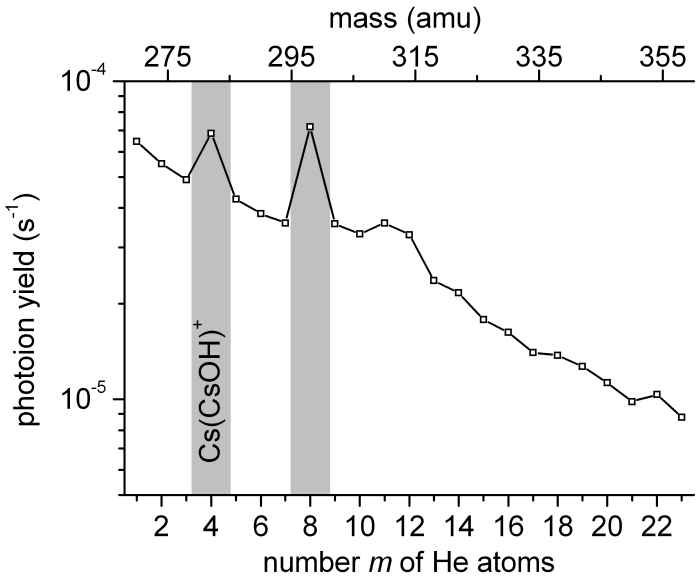

Figure 5.6.: Cs_2^+-He_m abundance of Cs doped He nanodroplets with an initial size of $\bar{N}_i \sim 15000$ He atoms for the pulsed laser only configuration (photon energy $22100\,cm^{-1}$). Significant drops in the intensity beyond $m = 4, 8$ are marked by gray bars and are explained in the text.

should be close to the ionization threshold of bare Cs atoms. With an approximate excess energy of $1800\,cm^{-1}$ above the ionization threshold an evaporation of about 450 He atoms from the nanodroplet is expected. Note, that the binding energy of He atoms to the nanodroplet is $\sim 5\,cm^{-1}$.[26] The binding energy between the ion and the nanodroplet is transformed into He evaporation. The difference in energy between an ion at the center and one near the edge of the He nanodroplets is given as $\sim 150\,cm^{-1}$.[125] We assume that approximately 30 He atoms will be evaporated due to this process. The pick-up process itself lowers the nanodroplet size by approximately 240 He atoms according to Ref. 45. Moreover, the formation of snowballs itself could also lead to an energy release and therefore to an additional evaporation of He. In Ref. 69 the total energy for a Cs^+-He_{128} system is given with 22.90 K per He atom. With this we deduce a further evaporation of 420 He atoms. In total, we estimate a nanodroplet size reduction of ~ 1140 He atoms. (ii) The sensitivity of our multi-channel-plate detector is strongly mass dependent in this regime[146], so that higher masses will not be recorded well. The recorded masses show therefore only the lower portion of the nanodroplet size distribution. We also note that the observed signals, shown in Figs. 5.7 and 5.8, may not reflect the actual mass distribution due to voltage limitations of our extraction field. The measured signal should be a convolution of an instrumental function and the He_N size distribution. A best fit turns out to be given by a log-normal distribution, which

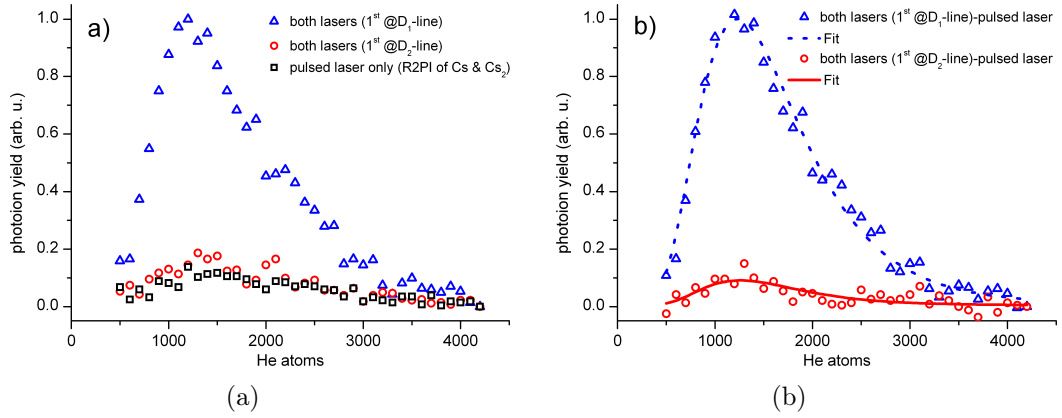

(a) (b)

Figure 5.7.: a) Measured signals for three different laser configurations, where the abscissa scale is given in numbers of He atoms. The different ionization products of Cs doped He nanodroplets with an initial size of $\bar{N}_i \sim 8000$ He atoms have been monitored with and without the cw laser for the first-step excitation. Photon energies were set to D_1: 11197 cm^{-1}, D_2: 11835 cm^{-1}, and pulsed laser: 22204 cm^{-1}. The signals were binned with a bin width of 25 He atoms, where the central number is labeled in the graph. **b)** Difference of signals: "both lasers" - "pulsed laser only". The difference signals are fitted using a lognormal function. The values are scaled to the maximum of the fit amplitude.

reproduces the measured intensities in a proper way.

Finally, we studied the Cs^+-He_N signal ($Cs^+ \leftarrow 6^2P_{1/2} \leftarrow 6^2S_{1/2}$) in detail for different initial nanodroplet sizes in the range of $\bar{N}_i = 3 - 15 \times 10^3$ atoms by choosing our source parameters according to the scaling laws of Ref. 29 (Fig. 5.8). The measured intensities, as well as the fits, correlate clearly with the nanodroplet size, including the mentioned reasons for the size reduction. Under all nozzle conditions given in Fig. 5.8, only negligible ion signals at high masses were detected without the cw pump laser as in Fig. 5.7a.

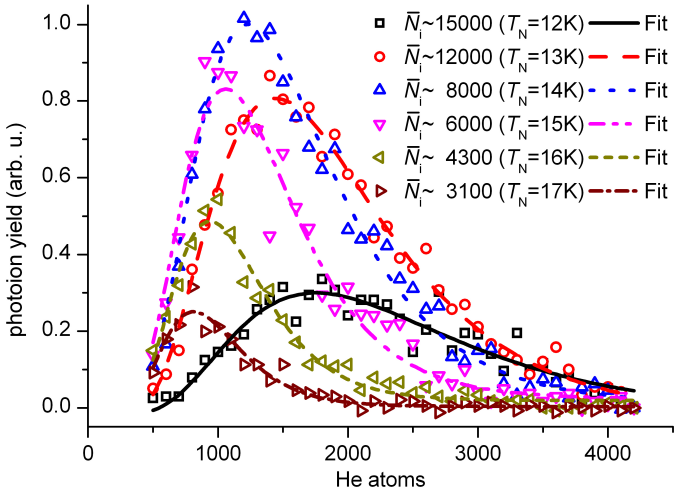

Figure 5.8.: Comparison of TOF spectra (difference signals) obtained with different nanodroplet sizes $\bar{N}_i$. Photon energies were set to D_1: 11197 cm^{-1} and pulsed laser: 22204 cm^{-1}. The data are fitted with a lognormal function. The fit values for $\bar{N}_f$, given in ascending order, are 950, 1100, 1250, 1500, 1800, and 2250.

5.5. Theoretical approach

In this Section we describe the model used for the simulation of the emission spectrum of Cs doped He droplets shown in this Chapter. Within this approach the density distribution of cesium doped He_N has been calculated for Cs in its ground state $6^2S_{1/2}$ ($^2\Sigma_{1/2}$) as well as in its excited state $6^2P_{1/2}$ ($^2\Pi$). The used method has been introduced by G. Auböck and is described in great detail in Ref. 96. Similar methods have been used in Refs. 57,136. We will briefly repeat the described method[96] and show our own results. For convenience we state diatomic **AkHe** states and their properties in bold letters to distinguish between Ak-He_N potential energy curves. Excited state potentials are denoted with * (e.g. Cs*).

The valence electron of the alkali-metal atom on the He droplet can be described with a Hamiltonian consisting of three parts

$$\mathcal{H} = \mathcal{H}_{\text{atom}} + \mathcal{H}_{\text{SO}} + \mathcal{H}_{\text{droplet}} \tag{5.1}$$

where $\mathcal{H}_{\text{atom}}$ is the Hamiltonian of the bare atom without spin-orbit coupling, which potential energies are well known. $\mathcal{H}_{\text{SO}}$ is the spin-orbit (SO) coupling Hamiltonian. The interaction between Ak atom and the N He atoms of He_N is described by $\mathcal{H}_{\text{droplet}}$, which depends on the distance R between Ak atom and each He atom.

The introduction of a spin-orbit related perturbation $\mathcal{H}_{\text{SO}}$ not dependent on R is in analogy to Takami and co-workers[106] and Reho *et al.*[107] and is well known. As in this section only the spin-orbit coupling for the 6^2P-states ($L = 1$) is relevant, we state here only the relevant Hamiltonian in the given basis[107]

$$\mathcal{H}_{\text{SO}} = A_{\text{SO}} \begin{pmatrix} 0 & \frac{\sqrt{2}}{2} & 0 \\ \frac{\sqrt{2}}{2} & -\frac{1}{2} & 0 \\ 0 & 0 & \frac{1}{2} \end{pmatrix} \tag{5.2}$$

The SO coupling constant A_{SO} can be calculated from the energy splitting of the atomic state (Δ_{SO}): $2/3\,\Delta_{\text{SO}}$. For the 6^2P states of Cs this is $\Delta_{\text{SO}} \sim 554\,\text{cm}^{-1}$.

The energy splitting of the lowest electronic states of Cs is large compared to the droplet-induced perturbation, which is known from recorded D-line spectra of Cs-He_N, so that the system can be expressed in terms of a diatomic molecule, often called *pseudo − diatomic molecule*, in order to explain absorption spectra. In Ref. 96 the notation used here was derived in great detail: the basis states of $\mathcal{H}$ are chosen to be the eigenstates of $\mathcal{H}_{\text{atom}}$. The coordinate system is chosen to be cartesian (X, Y, and Z), with the quantization axis z. Then the basis states can be expressed by n, L, Λ, S, and

Σ: $|nL\Lambda\rangle\,|S\Sigma\rangle$. n is the main quantum number, L is the electronic angular momentum, Λ its projection on the quantization axis ($\Lambda = -L, -L+1, ..., L$), S is the electron spin (here 1/2) and Σ its projection ($= \pm 1/2$). In this basis $\mathcal{H}_{\text{atom}}$ becomes diagonal.

To obtain $\mathcal{H}_{\text{droplet}}$ one has to include the interaction of the Ak atom with all $\boldsymbol{k}$ He atoms of the droplet ($\boldsymbol{k}$ = 1-N), which can be done in the following way. Note, that the perturbation of the droplet only influences the electronic wavefunction of the Ak atom, because ^{4}He does not posess any magnetic moment in its ground state, so that the spin S (and Σ) is not influenced. The interaction $\mathcal{H}_k$ can then be described with Ak-He potential energy curves $V_{\textbf{Ak-He}}(r)$ without spin-orbit coupling: $V_{\textbf{Ak-He}}(r_k) = \langle nL\Lambda\,|\mathcal{H}_k|\,nL\Lambda\rangle$, where we introduced a new Hamiltonian, which describes the interaction between the Ak and one He atom in a different coordinate system ($\mathbf{x}$, $\mathbf{y}$, $\mathbf{z}$). Corresponding potential energy curves of Ak-He in different diatomic states can be found in Ref. 138. $\mathcal{H}_{\mathbf{k}}$ depends on the distance r_k between the alkali-metal atom and the $\boldsymbol{k}$-th helium atom. In the global coordinates (X, Y, Z) $\mathcal{H}^z_{\mathbf{k}}$ can be obtained by a rotation[96]

$$\mathcal{H}^Z_{\mathbf{k}} = \mathcal{D}^\dagger \mathcal{H}^z_{\mathbf{k}} \mathcal{D} \tag{5.3}$$

with $\mathcal{D}$ as Wigner rotation matrix. With the assumption that the influence of all He atoms is additive we obtain $\mathcal{H}_{\text{droplet}}$ as the sum over all He atoms

$$\mathcal{H}_{\text{droplet}} = \sum_{k=1}^{N} \mathcal{H}_{\mathbf{k}} \tag{5.4}$$

Let us think about the calculation of $\mathcal{H}_{droplet}$. First, one needs the positions of all $\boldsymbol{k}$ He atoms relative to the dopant. In general, there is the long-ranged van der Waals interaction between Ak atom and He atoms, which is responsible for the attraction. At short distances the Pauli repulsion between valence electron and He atoms forces to minimize the overlap between electron wavefunction and He droplet. The He density, calculated in relation to the Ak atom, is obtained as a convolution of these two conflicting forces. Here, the density distribution calculation of Ak-He$_N$ is performed with a density functional theory (DFT) code by F. Dalfovo[139] modified by K. K. Lehmann and R. Schmied.[140], where details of this code can be found in the corresponding works. For this, the interaction $V_{\textbf{Ak-He}}(r)$ has to be calculated precisely. The CsHe pair potentials[138] are denoted in diatomic states without SO coupling. The corresponding diatomic states of the 6^2S (Σ) and 6^2P (one Σ and one doubly generated Π) states are given in brackets. The calculation of a He density profile with Cs in its ground state is straightforward. The $X\Sigma$ potential of Pascale[138], which asymptotically connects to the 6^2S state of Cs, with a Hund's case (a) coupling scheme used for $V_{\textbf{Ak-He}}(r)$. A spline fit of Pascale's $X\Sigma$ CsHe potential does not vary significantly from newer KTTY-potentials (Kleinekathöfer,

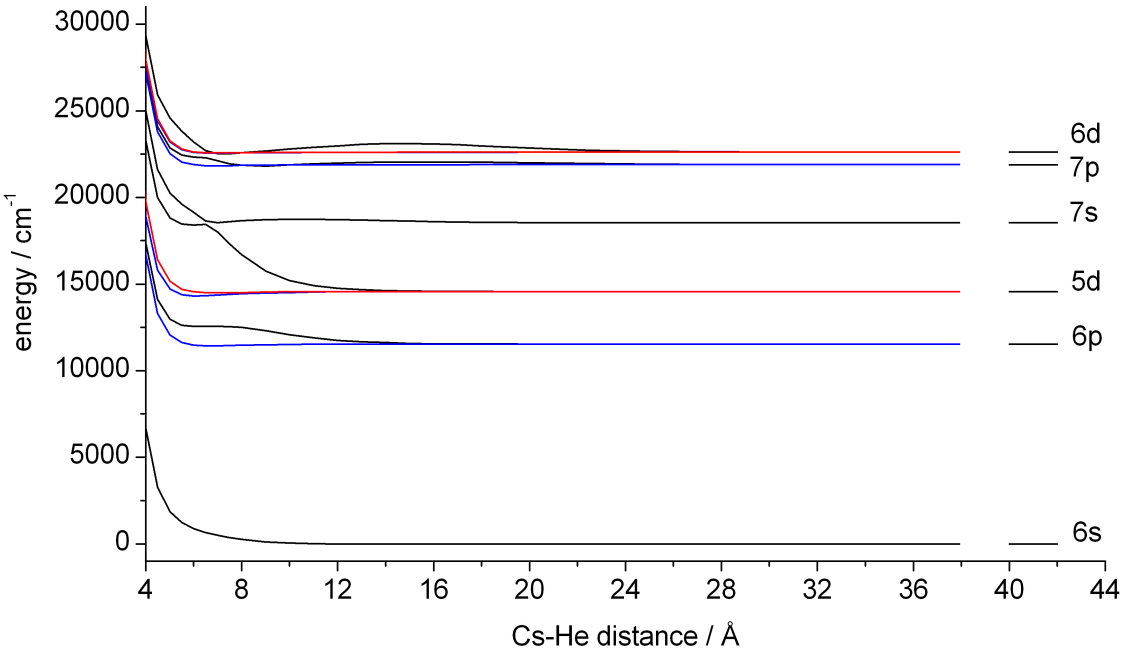

Figure 5.9.: CsHe pair potentials in the different diatomic states Σ (black), Π (blue), and Δ (red) without spin-orbit coupling. The diatomic states connect asymptotically in the $^2n_0$ states of the Cs atom. The underlying data are taken from Ref. 138.

Tang, Toennies, Yiu)[147,148] As we need also excited state CsHe potentials we trust in Pascale's potential energy curves for the calculation of the He densities (Fig. 5.9).

Second, the energy potential curves for Ak-He$_N$ are then obtained from the density profile with a simple integration instead of the sum in eq. 5.3

$$\mathcal{H}_{\text{droplet}} = \int \rho(r)\, \mathcal{H}_k(r) d^3r \tag{5.5}$$

In a dipole approximation, where one can use cylindrical coordinates, this turns to be

$$\mathcal{H}_{\text{droplet}} = \int \rho(r)\, \mathcal{H}_k(r)\, r^2\, \sin(\theta)\, dr d\theta d\phi \tag{5.6}$$

$$\mathcal{H}_{\text{droplet}} = \rho(r)\, \mathcal{H}_k(r)\, r\, 2\pi \tag{5.7}$$

which equals the potential energy curve without a constant shift caused by the atomic energy state (e.g. 6^2P) and a smaller shift due to SO-coupling. For the simulation of absorption spectra one calculates the involved Ak-He$_N$ potential energy curves. The He density is assumed to be frozen during the excitation, so that one uses the relevant diatomic states ($V_{\mathbf{Ak\text{-}He}}(r)$) in oder to obtain the Ak-He$_N$ potential energy curves within

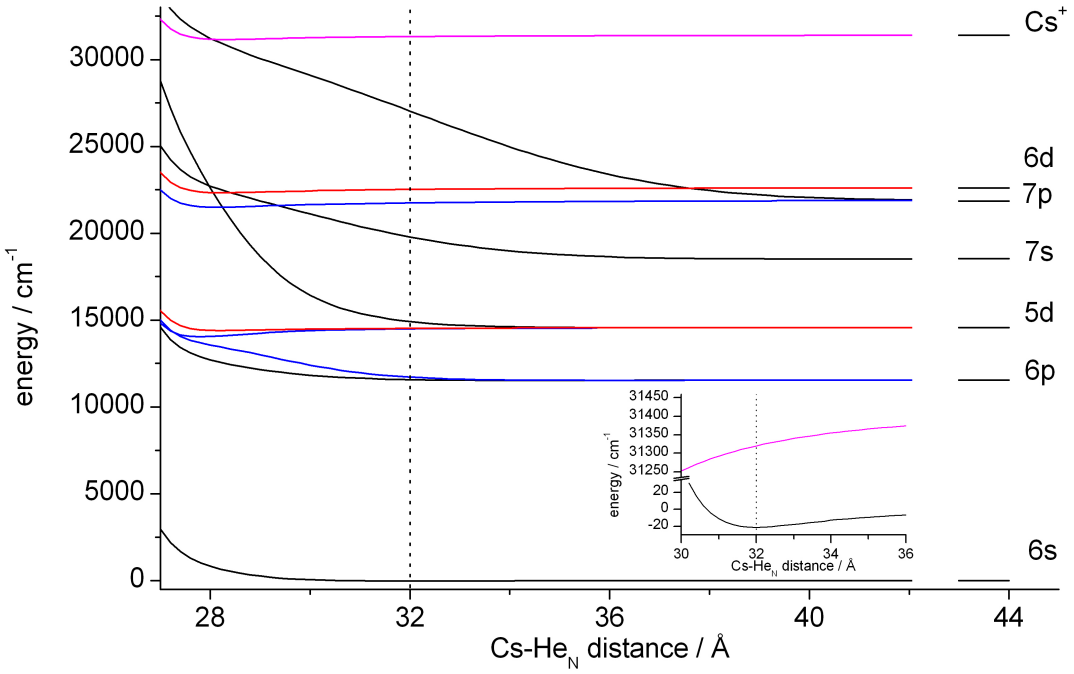

Figure 5.10.: Calculated potential energy curves of Cs on a He droplet in its different diatomic states Σ (black), Π (blue), and Δ (red) without spin-orbit coupling as well as the Cs^+ ion (magenta). The diatomic states connect asymptotically to the atomic states without spin-orbit coupling. The vertical dotted line represents the minimum of the ground state potential. Details of the calculation are given in the text. Note that the He density is assumed to be frozen, so that the potential energy curves represent the situation during the excitation. In the inset one sees that the ground state (black) and the ion (magenta) behave both attractive.

the integration. In Fig. 5.10 the potential energy curves of Cs-He_N ($N = 2000$) without SO-coupling are shown. One sees that the Cs ground state is bound to the surface of the He droplet. At the same distance the ionic potential energy curve is lower in energy than the Cs^+ ionization threshold of 31406.5 cm^{-1}. The potential energy curve increases at lower distances for Cs^+, which is clearly wrong. This is for reasons of calculation, where the He density has not been modified. In this scenario the ionization threshold is redshifted by a small amount.

To explain the emission spectrum (Fig. 5.4) one has to modify the He density, as the relaxation into a vibronic ground state of non-desorbing Ak atoms on He droplets is faster than the decay into the electronic ground state.[1,60] This goes along with a change of the He density due to the increased electron wavefunction of the valence electron.

In the case of the the $6^2P_{1/2}$ ($^2\Pi_{1/2}$) state the He density has to be modified, which

goes along with different diatomic CsHe potential curves: we use the CsHe potential curves $A\Sigma$ (repulsive) and $A\Pi$ (attractive) of Pascale[138], which end asymptotically in the 6^2P_0 state of the Cs atom. G. Auböck has introduced spin-orbit coupling in the calculation of a modified He droplet density in the case Rb^*-He_N in his PhD thesis, when the excitation from the ground state takes place at photon energies close to the atomic D_1-line.[96] It turned out that Σ and Δ are not good quantum numbers anymore, because of the small difference of the $A\Pi$ and $A\Sigma$ state in comparison to the SO-coupling of the free Cs atom. In the Hund's case (c) coupling scheme, which should be used instead, the spin and the electronic angular momentum couple to a total angular momentum first ($J = L + S$), which is then projected on the quantization axis (Ω). This means that the Cs-He_N states $^2\Sigma_{1/2}$ and $^2\Pi_{1/2}$ have to be mixed in order to get $|\Omega\rangle = |1/2\rangle$. $\mathcal{H}_{\mathrm{SO}} + \mathcal{H}_{\mathrm{droplet}}$ has to be diagonalized to obtain mixing coefficients. For a calculation with full precision one has to do this in every iteration step of the calculation for the He density. This has been fully treated in recent publications based on Monte Carlo simulations (cf. Refs. 149,150), where excited states of Rb atoms on cold helium have been calculated. A simplified approach is used here instead.

Before we explain the approach we want to remind the reader about the shape of the orbital radius of the $6^2P_{1/2}$ state of Cs, which plays an important role in the formation of exciplexes[109] as well as in the calculation of the He density. The wavefunction of the $6^2P_{1/2}$ state of free Cs atoms is a convolution of two sublevel wavefunctions. The 6^2P state manifold splits into two sublevels with $J = 1/2$ and $3/2$ ($J = L + S$), thus $m_J = \pm 1/2, \pm 3/2$. In the basis $|L, m_L, S, m_S\rangle$ and with the normalization condition $|\alpha| + |\beta| = 1$ we get for the $6^2P_{1/2}$ state ($J = 1/2$, $|m_J| = 1/2$)

$$\Psi_{J,m_J} = \Psi_{1/2,1/2} = \alpha\,|1, 1, 1/2, -1/2\rangle - \beta\,|1, 0, 1/2, 1/2\rangle \tag{5.8}$$

With

$$\langle S, m_S | S, m'_S\rangle = \delta_{m_S, m'_S} \tag{5.9}$$

one gets

$$\left\langle \Psi_{1/2,1/2} | \Psi_{1/2,1/2} \right\rangle = \left|\Psi_{1/2,1/2}\right|^2 \tag{5.10}$$

$$= |\alpha|^2 \langle 1, 1 | 1, 1\rangle - |\beta|^2 \langle 1, 0, | 1, 0\rangle \tag{5.11}$$

Let us express this in terms of spherical harmonics $\Upsilon_L^{m_L}$:

$$\Upsilon_1^1 = -\frac{1}{2}\sqrt{\frac{3}{2\pi}}\,\sin\theta\,\mathrm{e}^{-i\phi} \tag{5.12}$$

$$\Upsilon_1^0 = \frac{1}{2}\sqrt{\frac{3}{\pi}}\,\cos\theta \tag{5.13}$$

With $\alpha = \sqrt{2/3}$ and $\beta = -\sqrt{1/3}$ we obtain

$$\left|\Psi_{1/2,1/2}\right|^2 = \frac{1}{4\pi}(\sin^2\theta + \cos^2\theta), \tag{5.14}$$

which is clearly spherical.[109]

Let us now briefly explain the density calculation. The perturbation by the droplet ($\sim 10\,\mathrm{cm}^{-1}$) is fairly small in comparison to the SO-coupling ($\Delta_{\mathrm{SO}} \sim 554\,\mathrm{cm}^{-1}$) for the ^{2}P states of the Cs atom). The slight droplet-induced perturbation can be seen in the emission spectrum (Fig. 5.4), where the difference between on-droplet emission of Cs atoms and off-droplet emission is tiny. In this case a Hund's case (c) coupling scheme with Ω as quantum number can be used. For the calculation of the interesting non-desorbing Cs-He state$_{\mathrm{N}}$ we have $L = 1$, $S = \frac{1}{2}$, $J = \frac{1}{2}$, and $\Omega = \frac{1}{2}$. The mixing is represented by Clebsch-Gordon coefficients similar to the previous calculations leading to a new potential for the interaction between Cs atom and each He atom

$$V^{\Omega=1/2}_{\text{Ak-He}}(r) = c^2_{\Pi} V^{\Pi}_{\text{Ak-He}}(r) + c^2_{\Sigma} V^{\Sigma}_{\text{Ak-He}}(r) \tag{5.15}$$

$$V^{\Omega=1/2}_{\text{Ak-He}}(r) = \frac{2}{3} V^{\Pi}_{\text{Ak-He}}(r) + \frac{1}{3} V^{\Sigma}_{\text{Ak-He}}(r) \tag{5.16}$$

With this, we obtain a density profile, which deviates from the one of the electronic ground state (Fig. 5.11). The Cs atom is pushed further away from the droplet's center of mass due to the larger electron wavefunction. As a consequence the dimple size decreases compared to the one of Cs-He$_{\mathrm{N}}$, which is caused by a weaker interaction between Cs and He droplet. Also the geometry of the droplet itself is changed.

Note that the approximations used for the calculation of the Hamiltonian $\mathcal{H}_{\mathrm{droplet}}$, which describes the influence of the droplet, are only valid, if the perturbation is small compared to the difference of electronic states of the bare atom. This seems to be the case only for the lowest electronic states (e.g. Cs: 6^2S, 6^2P, 6^2D). For the calculation of higher electronic states a different approach as in Ref. 105 should be used.

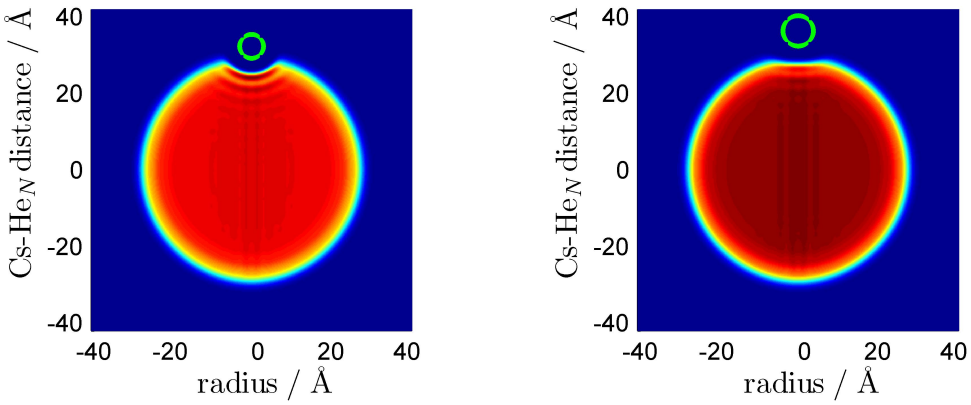

(a) (b)

Figure 5.11.: (a) Equilibrium helium density of a Cs-doped He droplet ($N = 2000$) with the Cs atom in its ground state. The green circle represents the orbital radius of the Cs atom. In (b) the Cs atom is in its first excited state, so that the He density is modified and the orbital radius is slightly increased. Details of the calculation and their explanations are given in the text.

6. Ionization thresholds of Rb and Cs on He droplets and Rydberg states dynamics

In this chapter we report measurements of the ionization threshold of single rubidium (Rb) and cesium (Cs) atoms on He nanodroplets (He_N). Alkali-metal atoms usually detach from the surface of a He_N when electronically excited. As an exception Rb and Cs atoms do not desorb when excited with photon energies close to their D_1 line. Upon photoionization the positively charged ions immerse into the He_N, where they most probably form snowballs. We report measurements of the photoionization efficiency for the rubidium-He_N and cesium-He_N systems and find that the ionization threshold is lowered compared to the free atoms. The corresponding energy shift increases when going from heavy to light alkali metals and from small to large helium droplets. Both effects can be explained by the difference in polarization energies associated with submerged alkali metal cations. The findings agree qualitatively well with recent calculations of helium snowball formation around alkali metal cations. In addition we show measured lifetimes of highly excited Cs-He complexes, which indicate the proposed non-desorbing character of these states.

6.1. Ionization thresholds of Rb and Cs atoms on He droplets

Helium droplets (He_N) serve as unique spectroscopic matrix for the isolation of atoms, molecules and clusters in a nanoscale superfluid environment of about 0.4 K temperature[26] while allowing the application of basically all molecular beam techniques.[78] The superfluid property permits unhindered nuclear motion of the dopant and sharp lines in microwave and infrared spectra.[26,78] Electronic excitation spectra may be strongly broadened because of the Pauli repulsion by the surrounding helium.[78] So far, mainly neutral impurities have been studied in and on helium droplets. As mass selection of dopants is sometimes an important issue, the interaction of ionic species with helium is a subject of increasing interest. Based on the electrostatic potential produced by the

dielectric response of the helium to an ionic impurity, Lehmann and Northby[125] presented a potential for the motion of an ion inside a helium droplet. While they derive an almost harmonic trapping potential for any ionic impurity with the minimum in the center of the droplet and a positive anharmonicity that lets the potential energy rise steeply towards the droplet surface, the absolute depth depends of course on the species. Because of the significantly different interaction energy of neutral and ionized impurities with helium a deviation of the ionization threshold (IT) from the free atom or molecule value is to be expected.

As neutrals, alkali metal (Ak) atoms and molecules play a special role in helium droplet isolation spectroscopy because of the extremely weak alkali metal-helium interaction. As already observed in the first experiments at Princeton,[57] alkali metal dopants reside on the droplet surface and do not migrate into the helium. Ak ions, however, will strongly polarize nearby helium atoms and surround themselves by a helium snowball.[69] In fact, the immersion of rubidium[2] (Rb) and cesium[4] (Cs) ions into helium droplets was recently reported. Galli, Ceperley, and Reatto[69] present theoretical results for the interaction energy of alkali metal ions with surrounding helium in small droplets that allow an estimate for the trend in the shift of ionization thresholds for Na, K, and Cs.

The immersion of positively charged Ak ions into the He_N creates strong electrostatic effects between He_N and Ak^+ ion and has recently been studied in various experiments (cf. Refs. 2,4,151). With this in mind, an artificial atom[152] consisting of a positively charged ion in the He nanodroplet and an electron outside could be created with Ak atoms. Due to the strong polarization of helium around a positively charged Ak ion, the Ak atom core can already migrate into the droplet if the electron density of the Ak atom valence electron becomes negligibly small in the He droplet region. A decrease of the ionization threshold (IT) should be an indication that the positively charged Ak atom core starts to polarize the He droplet before the electron is fully removed and is therefore of fundamental interest. Also our calculations in Sec. 5.5 indicate a slightly lower IT.

Experimentally, the determination of the on-droplet ionization threshold requires ionization sources of the appropriate energy and the detection of the well-defined ion product. Simply detecting ionized alkali metals with attached helium may result from ionization of larger Ak aggregates on helium droplets and subsequent fragmentation in the same cluster beam. Rubidium and cesium offer the unique opportunity to avoid this ambiguity through a two-step ionization taking advantage of an intermediate resonance. Whereas the lighter Ak atoms detach from the surface of the He_N after electronic excitation, the excitation of Rb-He_N[60] into the $5^2P_{1/2}$ ($^2\Pi_{1/2}$) state and Cs-He_N[4] into the $6^2P_{1/2}$ ($^2\Pi_{1/2}$) does not lead to detachment but leaves the excited atoms residing on the surface. Corresponding excitation and emission spectra of Rb-He_N and Cs-He_N are

shown in Refs. 60 and 4, respectively. These findings have allowed a number of investigations that make use of this bound $n^2P_{1/2}$ ($^2\Pi_{1/2}$) state (Rb: $n = 5$, Cs: $n = 6$) as springboard for further excitation or ionization [1,2,4] of Ak-He_N complexes while excluding a simultaneous detection of fragmentation products. The recent assignment of nS, nP, and nD Rydberg series of Cs atoms on helium droplets [5] is an example.

The notation of electronically excited states of Ak-He_N with moderate principal quantum number n is based on a pseudo-diatomic model, in which the He_N acts as one large atom and the "internuclear axis" from the droplet center to the surface located Ak atom serves as quantization axis for orbital and spin momenta in a Hund's coupling *case a*. As described in detail in Refs. 1 and 61, a state is then characterized by its atomic designation in the LS coupling scheme (e.g. $n^2P_{1/2}$) and the diatomic molecule *case a* notation (e.g. $^2\Pi_{1/2}$). In the detailed study of Ref. 5, this pseudo-diatomic picture was judged to be valid up to $n \sim 10$ for Cs-He_N. For higher excitations, the role of the "internuclear axis" vanishes and we are faced with atomic like Rydberg states with an indication that the Ak ion core starts to sink into the droplet. [5]

Here, helium droplets are produced in a supersonic beam expansion of 60 bar of helium gas through a 5 μm diameter nozzle at temperatures between 14 and 20 K, yielding average sizes of helium droplets between 5000 and 15000 atoms/droplet according to the scaling laws of Harms, Toennies, and Dalfovo. [29] As details of the experimental set-up, the doping with Ak atoms, and the applied laser systems have been provided in Refs. 1,4,5 and in previous chapters, we will restrict ourselves to explaining the applied laser excitation/ionization scheme in the following. Rb (Cs) monomers on He_N are ionized in a resonant 2-photon ionization (R2PI) scheme with two pulsed lasers. First, they are excited into their non-desorbing $n^2P_{1/2}$ ($^2\Pi_{1/2}$) state (Rb: $n = 5$, Cs: $n = 6$) with laser 1 (L1, Ti:Sapphire laser Coherent Indigo S, pulse duration 30 ns, pulse energy 75 μJ, linewidth $< 0.125\,cm^{-1}$). A second photon of laser 2 (L2, dye laser Lambda Physik FL 3002, pulse duration 30 ns, pulse energy 6 mJ, linewidth $\sim 0.2\,cm^{-1}$) ionizes these Ak*-He_N complexes (* indicates an excited state). Both lasers have a linewidth $\leq 0.2\,cm^{-1}$, i.e. much smaller than the $\sim 10\,cm^{-1}$ wide $n^2P_{1/2}$ ($^2\Pi_{1/2}$) state excitation, where the atom stays bound to the He_N. [4,60] As L1 has a repetition rate of 5 kHz and L2 of 100 Hz, a home-made synchronization device was built to guarantee the time overlap of two laser pulses of L1 and L2. Every 50^{th} pulse of the 5 kHz L1 (master) coincides with one L2 pulse (slave). The time delay between both laser pulses was adjusted to be smaller than 10 ns, i.e. smaller than the radiative lifetime of the intermediate state ($\tau \sim 30$ ns). Laser wavenumbers were determined using a wavemeter (Coherent WaveMaster, accuracy < 0.005 nm). The non-desorption of the first excited state makes this specific R2PI scheme favorable as demonstrated in Refs. 1,4,5. The subsequent immersion of the positive charge is observed in time-of-flight (TOF) mass spectra at large masses, where the

Ak cation sticks together with at least 500 He atoms. The photoionization efficiency (PIE) of the Ak-He$_N$ is observed by varying the photon energy of L2 and simultaneously monitoring the photo ion yield with our TOF mass spectrometer at these large masses.

The influence of the extraction field lowering the IT was taken into account by calibration with free alkali metal atom ionization. The influence of the extraction field lowering the IT was taken into account by calibration with free alkali-metal atom ionization: the IT is lowered by a constant value due the constant electric field in the ionization regime. We therefore corrected this decrease of the IT by adding this value ΔE to the photon energies. The decrease can be estimated with $\Delta E = 6.12\sqrt{F}$ (eq. 2.3) in the case of hydrogenic atoms and if the perturbation by the electric field F is small. At larger electric field, which we use to detect Ak$^+$-He$_N$ complexes, and for Ak atoms ΔE differs from this value. In order to find the correct shift of the ionization threshold we measured the Rb$^+$ ion yield in dependence of the photon energies of L2 with two different field strengths. The first one is given with 317 V/cm; the latter one (1150 V/cm) is used to detect Ak$^+$-He$_N$ complexes. We know from other measurements[5] that the ionization threshold of the pure Ak$^+$ in a R2PI scheme is not lowered. With this the influence of the electric field in the latter case can be derived to $\Delta E = 189\,\mathrm{cm}^{-1}$. As in our previous two-step experiments,[2,4] the ion yield obtained when using only L1 was recorded separately. It turned out to be within the noise level and could be neglected.

In general, the ionization threshold can be extracted with several methods from the PIE. Here, we use a Gaussian error function $f(\epsilon)$ (Refs. 153,154)

$$f(\epsilon) = \frac{1}{\pi} \int_{b(E-\epsilon)}^{\infty} e^{-t^2} dt. \tag{6.1}$$

Within this approach one fits Gaussians to the derivative of the photo ion yield function, where E and b are fit parameters. b is inversely proportional to the half width of the first derivative and E is at its maximum. We can interpret E as the vertical ionization potential[155]. Note that the linewidth of L2 is much smaller than the energy, where the photo ion yield increases, so that the non-finite linewidth can be neglected. As described in Refs. 1, 4, and 60, the binding energy of Rb and Cs to the droplet is at most $20\,\mathrm{cm}^{-1}$ in the ground state, i.e. the $n^2\mathrm{S}_{1/2}$ ($^2\Sigma_{1/2}$) state and even less, namely about $5\,\mathrm{cm}^{-1}$ in the shallow $n^2\mathrm{P}_{1/2}$ ($^2\Pi_{1/2}$) potential (Rb: $n = 5$, Cs: $n = 6$). Vibrational level spacings in this excited state potential will amount to about $1\,\mathrm{cm}^{-1}$. Even if we assume an immediate relaxation in this intermediate state, the error in relating the energy for the second step to the value of the ionization threshold is only between 3 and $4\,\mathrm{cm}^{-1}$. In order to be on the safe side and give an upper limit of the IT, we have chosen the atomic $n^2\mathrm{P}_{1/2}$ state as zero point (consistent with Ref. 5).

In Fig. 6.1 we display the photo ion yield of Rb and Cs doped He_N with an average size of $\bar{R} = 52 - 55$ Å as well as Gaussian error function fits (eq. 6.1). One can see that the ionization threshold is lowered for both Ak species by a small amount ΔIT. We also see that ΔIT is a function of the Ak species, which we will explain in terms of diatomic Ak^+He potentials. L2 was scanned continuously in the case of Rb-He_N and stepwise in the case of Cs-He_N, which explains the different illustrations (Rb: line, Cs: dots) in Figs. 6.1, 6.2, and 6.3. The dots represent an average of $\sim 1.3 \times 10^3$ laser shots of L2.

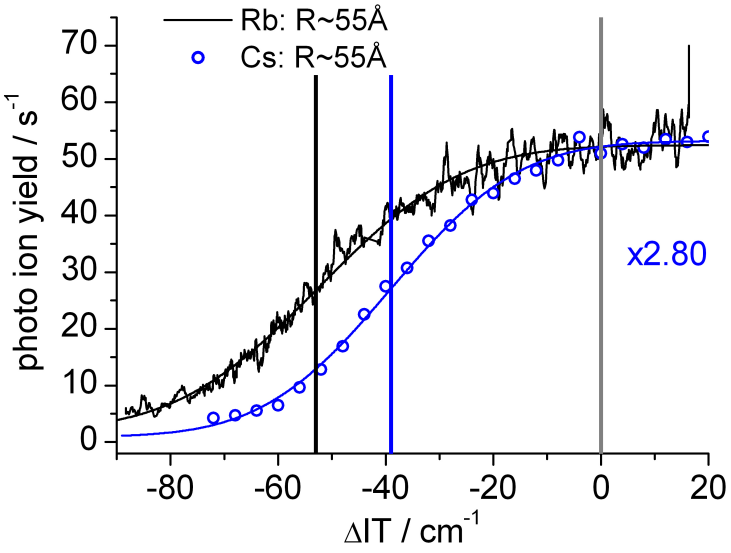

Figure 6.1.: Photo ion yield of Rb^+-He_N (black) and Cs^+-He_N (blue) complexes as a function of the photon energy of L2 relative to the IT of free Rb and Cs, respectively. The mean droplet size $\bar{N}$ is $\sim 13 - 15 \times 10^3$ He atoms, which is equivalent to $\bar{R} = 52 - 55$ Å. The gray vertical line represents the ionization threshold of Rb (Cs) atoms from their $n^2P_{1/2}$ states (Rb: $n = 5$, Cs: $n = 6$) and serves as zero point for the abscissa scale. The Cs^+-He_N signals are scaled to the height of the signal of Rb^+-He_N (smoothed). An error function fit has been applied. The black (blue) colored vertical line represents the ionization threshold of Rb (Cs) doped He_N measured with this technique. Features of the signals and the fits are discussed in the text.

Besides the influence of the Ak species on ΔIT we observe that ΔIT is also a function of the He droplet size. The He_N size is determined by the source conditions,[29] so that the mean radius $\bar{R}$ can be varied by either changing the nozzle pressure or the temperature. In Fig. 6.2 the photo ion yields of Rb (Cs) doped He_N with different mean droplet radii

are shown. One clearly sees that a larger He$_N$ leads to a stronger decrease of the ionization energy. This is consistent with measurements on sodium (Na) doped He droplets.[151]

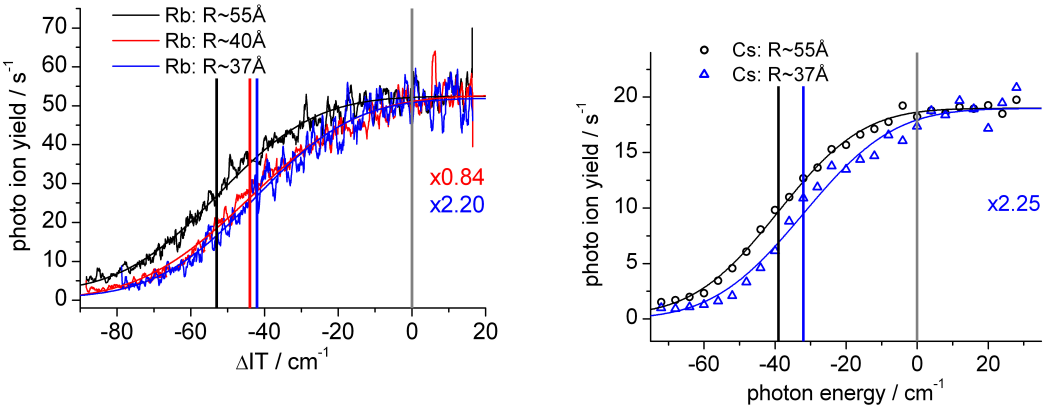

(a) (b)

Figure 6.2.: Photo ion yield of Ak$^+$-He$_N$ (**(a)** Ak=Rb, **(b)** Ak=Cs) complexes as a function of the photon energy of L2 (same scale as in Fig. 6.1). The mean droplet radius $\bar{R}$ is varied: ~ 55 (black), ~ 40 (red), and ~ 37 Å (blue). The gray vertical line represents the ionization threshold of Ak from its $n^2P_{1/2}$ (Rb: $n = 5$, Cs: $n = 6$) state and serves as zero point for the abscissa scale. The signals are scaled to the height of the signal of Ak$^+$-He$_N$ (**(a)** Ak=Rb, **(b)** Ak=Cs) with $R \sim 55$ Å and are smoothed. An error function fit has been applied. The colored vertical lines represent the ionization thresholds. Features of the signals and the fits are discussed in the text.

In addition, the photon energy of L1 is varied within the bandwidth of the $n^2P_{1/2}$ ($^2\Pi_{1/2}$) $\leftarrow$ $n^2S_{1/2}$ ($^2\Sigma_{1/2}$) on-droplet transition to show that this has no significant influence on the photo ion yield as a function of the wavelength of L2 (Fig. 6.3). In other words, the Ak*-He$_N$ relaxes in a pseudo-diatomic model into the lowest vibrational level of the intermediate state potential, which is consistent with earlier findings in Refs. 1 and 4.

In Fig. 6.4, we display recorded mass spectra of Cs$^+$-He$_N$ ($\bar{N} \sim 13 - 15 \times 10^3$ He atoms) with L2 tuned to photon energies slightly above or below the listed IT for this droplet size (6.1). For low photon energies, the observed size distribution shows that only larger Cs-He$_N$ were ionized, while higher energies are necessary to address smaller complexes within the distribution. In the case of small mean droplet sizes $\bar{N}$ the signal decreases and cannot be described anymore by a lognormal distribution (Fig. 6.3 **(b)**). The difference in estimated initial He droplet size and observed masses after ionization

has several reasons: As described in detail in Ref. 4, He_N size reduction is partly due to evaporation after the energy release caused by pick-up of the neutral atoms and after photoionization followed by the formation of strongly bound helium snowballs around the ion (loss of approximately 1000 He atoms[4,69]). To a larger extent the discrepancy is due to the sensitivity of our multi-channel-plate detector, which decreases strongly towards higher masses in the regime of our measurements.[146] The latter effect which may be included in an instrumental function is even increased by the fact that our extraction field is not large enough to efficiently pull the high masses out of the beam.

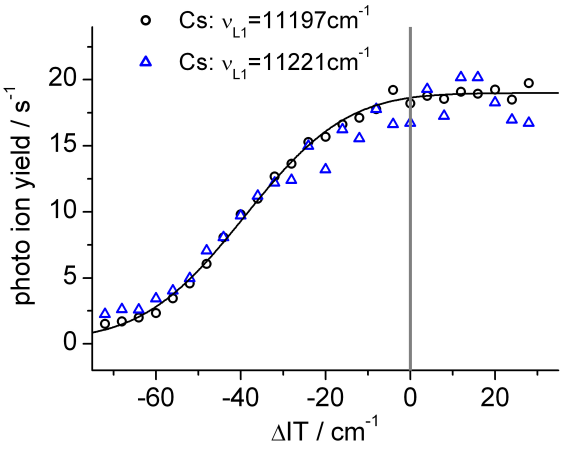

Figure 6.3.: Photo ion yield of Cs^+-He_N complexes ($\bar{R} \sim 55\,\text{Å}$) as a function of the photon energy of L2 for two different photon energies of L1: 11197 (black) and 11221 cm^{-1} (blue) (same scale as in Fig. 6.1). The gray vertical line represents the ionization threshold of Cs from its $6^2P_{1/2}$ state and serves as zero point for the abscissa scale. Features of the signals are discussed in the text.

In Tab. 6.1 we summarize the redshifts of the ionization threshold ΔIT of Rb and Cs doped He_N. The listed error is a combination of the statistical error ($\sim 5\,\text{cm}^{-1}$), the remaining uncertainty of the electric field ($\sim 3\,\text{cm}^{-1}$) and an uncertainty due to the finite depth of the intermediate $n^2P_{1/2}$ ($^2\Pi_{1/2}$) potential ($\sim 5\,\text{cm}^{-1}$). As explained above, the derived values of IT are based on the measured wavenumber of L2 and an energy calibration set by the atomic $n^2P_{1/2}$ level. This means that the IT for vertical ionization out of the intermediate state may be larger by up to $5\,\text{cm}^{-1}$. For this reason, we list a combined error with asymmetric boundaries. We also display recently published results, which show the influence of the He droplet on the ionization threshold of sodium (Na) atoms.[151] The decrease of the IT measured with our technique (PIE) can be compared with the IT of Cs on He_N given in Ref. 5, where the IT was found to be lowered by

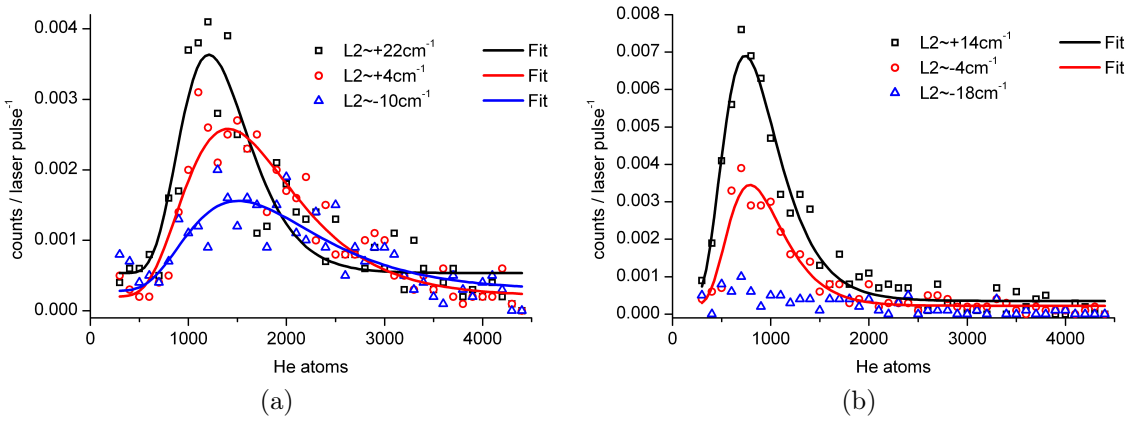

Figure 6.4.: TOF mass spectra of Cs^+-He$_N$ for three different photon energies of L2. The values of L2 are given in relation to the observed ionization threshold of Cs^+-He$_N$. The abscissa scale is given in numbers of He atoms. The He nanodroplets have an initial size $\bar{N} \sim 13 - 15 \times 10^3$ He atoms, which is equivalent to $\bar{R} \sim 55\,\text{Å}$. The signals were binned with a bin width of 100 He atoms, where the central number is plotted in the graph. The signals are fitted using a lognormal function, which describes the size distribution of He$_N$ formed with our conditions in a proper way. In **(a)** the droplet radius is set to $\sim 55\,\text{Å}$; in **(b)** to $\sim 37\,\text{Å}$

$\sim 50\,\text{cm}^{-1}$ for droplet sizes of $\bar{R} \sim 50\,\text{Å}$. There, a series of nS, nP, and nD states (up to $n \sim 20$) was fitted with the Rydberg formula. However, the formula may require some adjustment for very high Rydberg states where the electron is far away from the He$_N$, the Ak ion core dives into the He droplet surface, and the valence electron density becomes negligibly small at the He$_N$. This is the case for electronic states slightly below the IT, where the classical atomic orbital radii are large compared to the droplet size.

The extrapolation of Rydberg state energies works well for molecules where the Rydberg state potentials have very similar potentials as the ground state molecular ion. For an Ak atom on a He$_N$, the situation is different. In Fig. 6.5, we present a qualitative picture for Cs on He$_N$ ($N = 2000$) to explain the situation. Energy potentials are sketched for different ranges of excitation. The helium droplet surface is indicated by the dotted line at about $R = 27\,\text{Å}$. The Cs-He$_N$ ground state $6^2S_{1/2}$ ($^2\Sigma_{1/2}$) has a well depth of about 12 to $15\,\text{cm}^{-1}$ (Ref. 105) and the $6^2P_{1/2}$ ($^2\Pi_{1/2}$) potential one of about $5\,\text{cm}^{-1}$. The potentials for states with principal quantum numbers up to $n \sim 10$ exhibit a similar qualitative shape by showing a strong repulsion towards the surface of the droplet. As reported in Ref. 5, the situation changes for higher n. Measured excitation energies are lower than for the corresponding free atoms which means that for the R-range of the indicated Franck-Condon vertical excitation region the potential is lower than the free

Table 6.1.: Influence of He droplets on the IT of alkali metals in dependence of the mean He_N size $\bar{N}$ and the mean radius $\bar{R}$. The redshift of the IT is given in relation to the free atom IT. The values of Na^+ are taken from Ref. 151 (method ZEKE electron spectroscopy).

cation	$\bar{N}$ /He atoms	$\bar{R}$ /Å	ΔIT /cm^{-1}
Rb^+	13-15$\times 10^3$	52-55	53 ± 15
	6.0×10^3	40	44 ± 16
	4.7×10^3	37	42 ± 15
Cs^+	13.0×10^3	52	39 ± 14
	4.7×10^3	37	32 ± 14
Na^+	-	54	145
	-	40	130
	-	37	125

atom energy. On the other hand, the Ak^+ ion has its equilibrium position in the center of the droplet and non-penetrating Rydberg states should have qualitatively similar potentials. According to Ref. 69, polarization of helium atoms located around the ion leads to fairly rigid helium shells implying effectively an energy drop of almost 2000 cm^{-1} (using the total energy per particle of Cs doped helium clusters with $N = 128$ from Ref. 69). With the estimate of Ref. 125, the potential rises by approximately 150 cm^{-1} from the center of the droplet to $R = 0.9\,R_{\text{droplet}}$. In this model, the rest of the energy difference to the free Ak ion has to be "bridged" in the outer 10% of the helium droplet and the first few Å outside. This is indicated by the dotted part of the ion potential. The measured IT represents the value for "vertical ionization" from the minimum of the $6^2P_{1/2}$ ($^2\Pi_{1/2}$) potential. Assuming similar shape of all Ak^+-He_N potentials, the measured trends from heavy to light alkali atoms should correspond to the absolute depths of the ion in helium potentials as the calculated values of Ref. 69 actually do. Also the trend from smaller to larger droplets is in agreement with Galli et al.[69], who upon an increase of the helium cluster by a factor of 2 (from $N = 64$ to 128) find an increase in total binding of the ion by 20%. Ak^+-He diatomic potentials were calculated by various authors and confirm the trend.[63,120,121,156]

Fig. 6.5 also shows that direct ionization from the ground state may yield a slightly lower IT and provide the chance to obtain a further point on the potential energy curve. As mentioned, a drawback consists of the uncertainty due to signal contributions from fragmentation products. Rydberg states close to the IT should approach a similar potential shape and shed more light on the dynamics of the ion core "diving" into the nanoscale superfluid. Further theoretical calculations along the lines of Ref. 69 would

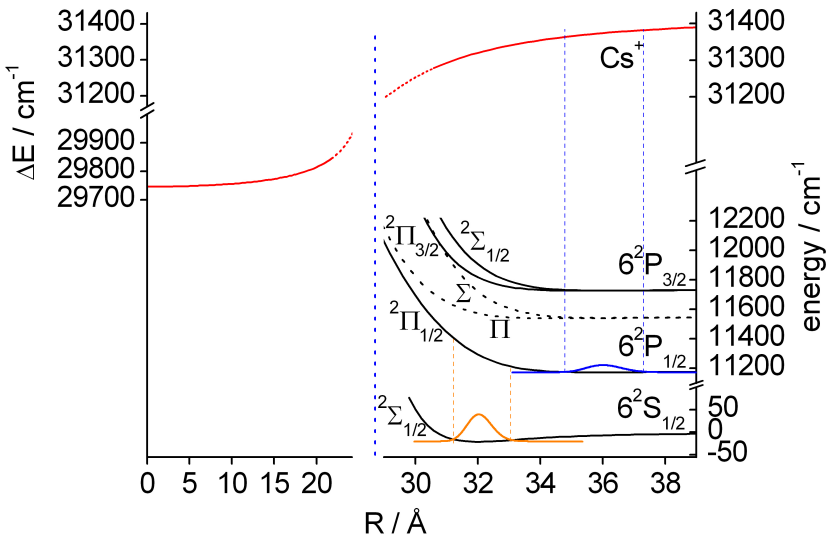

Figure 6.5.: Approximate energy potentials of Cs-He$_N$ and Cs$^+$-He$_N$ for $N = 2000$ and $R \sim 27$ Å. Ψ^2 and Franck-Condon vertical excitation region relevant to the experimental excitation scheme are indicated. Energy values are only approximate as explained in the text. The dotted line near $R \sim 27$ Å shows the boundary of the helium droplet.

certainly help our understanding of this fundamentally interesting system.

6.2. Rydberg state dynamics

The excitation of Ak atoms on He droplets to different electronic states goes along with a droplet-induced broadening of the transition. In the case of Cs the broadening exceeds the energy spacing between two levels at $\sim 200\,\mathrm{cm}^{-1}$ below the ionization threshold, which is lowered by $\sim 40\,\mathrm{cm}^{-1}$. Cs atoms are excited close to the ionization threshold in a resonant two-photon excitation scheme with two pulsed lasers (1$^{\mathrm{st}}$ Coherent Indigo-S, 2$^{\mathrm{nd}}$ dye laser). By using the $6^2P_{1/2}$ ($^2\Pi_{1/2}$) state as intermediate state the Cs atom is fully attached to the droplets surface during the excitation process. The highly excited state is then ionized by means of a pulsed electric field, which is built up in ~ 20 ns. By variation of the delay time one can examine the lifetime or the dynamics of the highly excited state by monitoring the amount of produced Cs$^+$ and Cs$^+$-He$_n$. The ion signal of Cs$^+$ and Cs$^+$-He with different delay times of the pulsed field is displayed in Fig. 6.6. The lasers (L1, L2) were set to photon energies of 11197 and 20140 cm^{-1}. The droplet beam and with this the Cs atom has a velocity of ~ 400 m/s and the entrance of the acceleration grid in our TOF-apparatus has a diameter of ~ 25 mm. The laser foci should be set to the center position of the grids in beam direction. A reliable ion signal

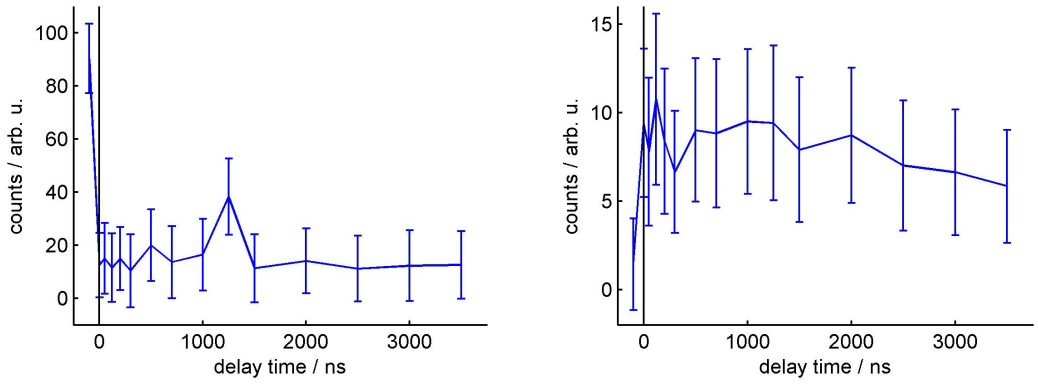

Figure 6.6.: Rydberg states dynamics. Cs^+ (a) and Cs^+-He (b) have been monitored for different delay times of the pulsed field after laser excitation $\sim 25\,cm^{-1}$ below the ionization threshold. Features of the signal are explained in the text.

can then only be achieved within a delay time of $\sim 5000\,ns$.

If the electric field is present before the laser pulses, the atom is directly ionized due to the lower ionization threshold. In the case of a delayed field (t>0μs) the atom is excited to a high Rydberg state and is then ionized by means of the electric field. The Cs^+ signal rapidly decreases to a nearly constant value. Instead the Cs^+-He signal increases and reaches a constant value, too. Let us first discuss the nearly constant asymptotic value. The lifetime scales with n^{*3} so that a HR state of Cs ($n \sim 100$) should have a lifetime in the millisecond range, which explains the asymptotic behavior of our signal. Remarkable is the rapid decrease at $t \sim 0$ of the Cs^+-signal and the increase of Cs^+-He. Usually one would not expect the decrease as the ionization probability is high for field ionization. The increase of the Cs^+-He signal could be connected to the Sekatskii atom.[152] The ionic core of the Cs atom penetrates the He droplet stronger if the electron radius is increased, so that the distance between Cs and He droplet could be lowered.

Nevertheless, for the existence of a Cs-He_N Rydberg complex the electron density of the valence electron of the Cs atom should exceed the size of the droplet, so that the droplet mostly interacts with the positively charged Ak atom core. We can compare this size with the radius of the He droplet. According to Ref. 80 the expectation value of the orbital radius r in $\AA$ is given by

$$\langle r \rangle = \frac{a_0}{2}\left[3n^{*2} - l(l+1)\right]. \tag{6.2}$$

$n*$ is the effective main quantum number: $n^* = n - \delta(n,l)$, $\delta(n,l)$ is quantum defect, and a_0 the Bohr radius. In an approximation we neglect $\delta(n,l)$ for highly excited states

(e.g. $n > 50$):

$$\langle r \rangle \sim \frac{0.53}{2} 3n^2, \tag{6.3}$$

which gives an expectation value of $\langle r \rangle \sim 2000\,\text{Å}$ ($n = 50$) and exceeds the He droplet radius by far. We have neglected that the electron density of the valence electron in the core region is not zero until the magnetic quantum number reaches high values ($l > 10$). To directly observe the existence of the proposed Sekatskii atom [152] we intend to monitor the lifetime of Ak^+-He_N as well as to excite the Ak atoms into levels with large l in the future. The already tested ZEKE detection mechanism could also gain new insights.

7. Alkali-metal clusters in their low- and high-spin states on He nanodroplets

Besides single alkali-metal atoms on helium droplets we examined small rubidium (Rb) and cesium (Cs) clusters, too. The study of these clusters is intended to fill the knowledge gap between single atoms and bulk material. He nanodroplets are a nearly ideal matrix for preparing and investigating clusters in a superfluid environment. Alkali-metal atoms are only bound very weakly to their surface by van-der-Waals forces. Due to the formation process high-spin states of alkali-metal clusters on He nanodroplets are favorably observed, which is in contrast to the abundance in other preparation processes. Until now the prevailing opinion was that stable clusters of the heavy alkali-metal atoms, Rb and Cs on He nanodroplets, are limited to 5 or 3 atoms, respectively (Schulz et al., Phys. Rev. Lett., 2004, 92, 13401)[157]*. Here, we present stable complexes of* Rb_n^+ *and* Cs_n^+ *consisting of up to* $n = 30$ *atoms, with the detection of large alkali-metal clusters being strongly enhanced by one-photon ionization. Our results also suggest that we monitored both high-spin and low-spin state clusters created on nanodroplets. The van-der-Waals bound high-spin alkali-metal clusters should show strong magnetic behavior, while low-spin states are predicted to exhibit metallic characteristics. Alkali-metal clusters prepared in these two configurations appear to be ideal candidates for investigating nanosized particles with ferromagnetic or metallic properties. After a small review of droplet flow, droplet sizes, and energy considerations, we present our results, which have been published in J. Chem. Phys. A Jan. P. Toennies Festschrift* ***115*** *(2011), 7005 (Ref. 3)*

7.1. Introduction

The design and development of nanoscaled materials is of large interest in modern material science. Relatively small clusters of atoms with tailored properties may be created as building blocks for new materials. Moreover, the binding properties, the formation

process and the stability of small atomic clusters are important for the understanding of larger nanoparticles. Alkali-metal (Ak) atoms are ideal candidates for the observation of a property change of the clusters with spin configuration and accordingly different electronic shell structure[73]. Recently, size-dependent stable configurations of both low- and high-spin states have been theoretically examined[158].

Here, we observe the formation and stability of Ak_n clusters with $n \leq 30$ consisting of rubidium (Rb) and cesium (Cs) atoms on a superfluid helium substrate. So far, clusters of heavy Ak atoms created on He nanodroplets (He_N) had only been discovered for small cluster sizes $n \leq 5$ (3) for Rb (Cs)[157]. Due to the formation process, observation of Ak clusters in high-spin states is strongly favored,[39] so the question arises whether larger Rb (Cs) clusters also exist in high-spin states on He_N. On large helium nanodroplets, also low-spin states of Ak_n may exist, if the deposited binding energy does not destroy the nanodroplet.

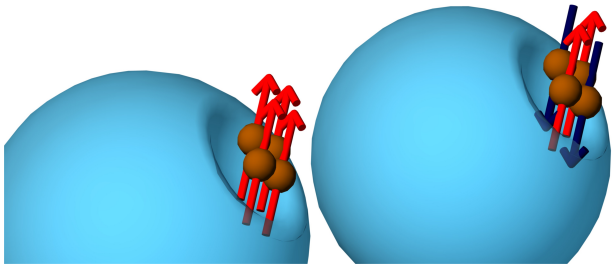

Figure 7.1.: Schematic of an alkali-metal cluster doped He droplet in different spin states.

7.2. Calculations of He droplet flows, droplet sizes, and energies

The formation of high-spin (HS) and low-spin (LS) alkali-metal (Ak) clusters on He droplets is connected to energy considerations and initial droplet sizes, which are described in Sec. 1.2. The production of clusters in different spin states could be linked with surface physics, if one is able to use the He droplet as a carrier to deposit clusters on cold surfaces. In this case, the corresponding surface properties could be studied with different methods. Mozhayskiy *et al.* demonstrated that the most gentle method to deposit clusters on a surface, namely to use He droplets as a carrier, works in principle.[31] Recently, this method has been used to deposit large Ag_n ($n \sim 300 - 6000$) clusters on an amorphous carbon substrate.[159]

In the following, we estimate (i) the He_N flow, (ii) the He_N size distribution, and (iii) compare these with deposited energies of small clusters in a short review.

(i) The He flow has been calculated in Sec. 1.2 (eqs. 1.15 - 1.18). (ii) The size distribution has been described in Sec. 1.2 (eq. 1.21) and follows a log-normal distribution for the subcritical expansion regime: $P(N) = \frac{1}{\sqrt{2\pi}N\delta} e^{-\frac{(lnN-\mu)^2}{2\delta^2}}$. μ and δ are the mean and standard deviation, respectively, of the variable's natural logarithm. The mean number $\bar{N}$ of He atoms, the median value N_m, the maximum of the size distribution $N_{\max}$, and the full width at half maximum $\Delta N_{1/2}$ are then given by (Fig. 7.2)

$$\bar{N} = \exp(\mu + \frac{\sigma^2}{2}), \tag{7.1}$$

$$N_m = \exp(\mu), \tag{7.2}$$

$$N_{\max} = \exp(\mu - \sigma^2), \tag{7.3}$$

$$\Delta N_{1/2} = \exp(\mu - \sigma^2 + \sigma\sqrt{2\ln 2}) - \exp(\mu - \sigma^2 - \sigma\sqrt{2\ln 2}). \tag{7.4}$$

Measured values of droplet sizes obtained at different stagnation pressures p_0 and nozzle temperatures T_0 can be found in Ref. 29. With droplet size scaling laws as found in Ref. 160 we can estimate intermediate values used in our experiments (Tab. 7.1).

Table 7.1.: Typical droplet sizes for different source conditions: T_0 and p_0 with fixed nozzle diameter $d = 5\,\mu$m

p_0/bar	T_0/K	μ	σ	$\bar{N}$	N_m	$N_{\max}$	$\Delta N_{1/2}$	Ref.
40	12.0	9.645	0.610	18600	15500	10600	16640	estimated
40	13.5	9.29	0.612	13000	10800	7400	11700	29
40	15.0	8.91	0.607	8900	7400	5100	8000	29
40	16.0	8.74	0.662	7700	6200	4000	6900	29
40	17.0	8.54	0.603	6100	5100	3600	5500	29
40	18.0	8.29	0.573	4700	4000	2900	4200	29
40	20.0	7.73	0.528	2600	2300	1700	2300	29
40	22.0	7.36	0.407	1700	1600	1300	1300	29
40	24.0	6.46	0.426	700	640	530	550	29

We can then estimate the total number of droplets with a specific size using the He flow and the size distribution. Let us keep in mind that the sum of all He droplets multiplied with their specific atom size has to equal the total number of He atoms. The size distribution $P(N)$ has then to be scaled with the He flow I_0 and the mean number

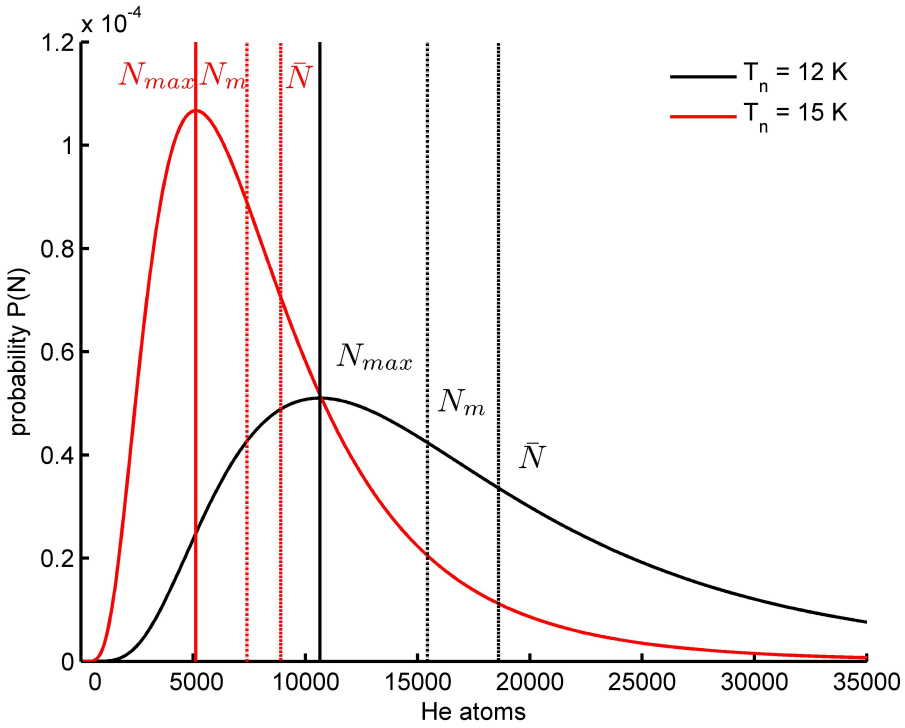

Figure 7.2.: Calculated normalized He droplet size distributions with a stagnation pressure of 40 bar. With higher temperatures the droplets shrink in size and the distributions become narrower. Vertical lines represent N_{max}, N_m, and $\bar{N}$ as described in the text.

$\bar{N}$, given by

$$\bar{N} = \frac{\int P(N)NdN}{\int P(N)dN} = \int P(N)NdN = \exp\left(\mu + \frac{\sigma^2}{2}\right), \tag{7.5}$$

where $P(N)$ is already normalized ($\int P(N)dN = 1$). With the normalized size distribution and

$$\bar{N} = \int P(N)NdN, \tag{7.6}$$

$$\int c_i P(N)NdN \stackrel{!}{=} I_{0,i} \rightarrow c_i = \frac{I_{0,i}}{\bar{N}}, \tag{7.7}$$

where c_i is a constant factor dependent on the initial source conditions, we obtain the He droplet size probability in $s^{-1}\,sr^{-1}$

$$P_{drop}(N) = \frac{I_0 \times P(N)}{\bar{N}} \tag{7.8}$$

The integration of P_{drop} multiplied with the specific droplet size leads again to the He flow

$$\int P_{drop}NdN = \int I_0 \frac{P(N)}{\bar{N}}NdN = \frac{I_0}{\bar{N}}\int P(N)NdN = I_0 \tag{7.9}$$

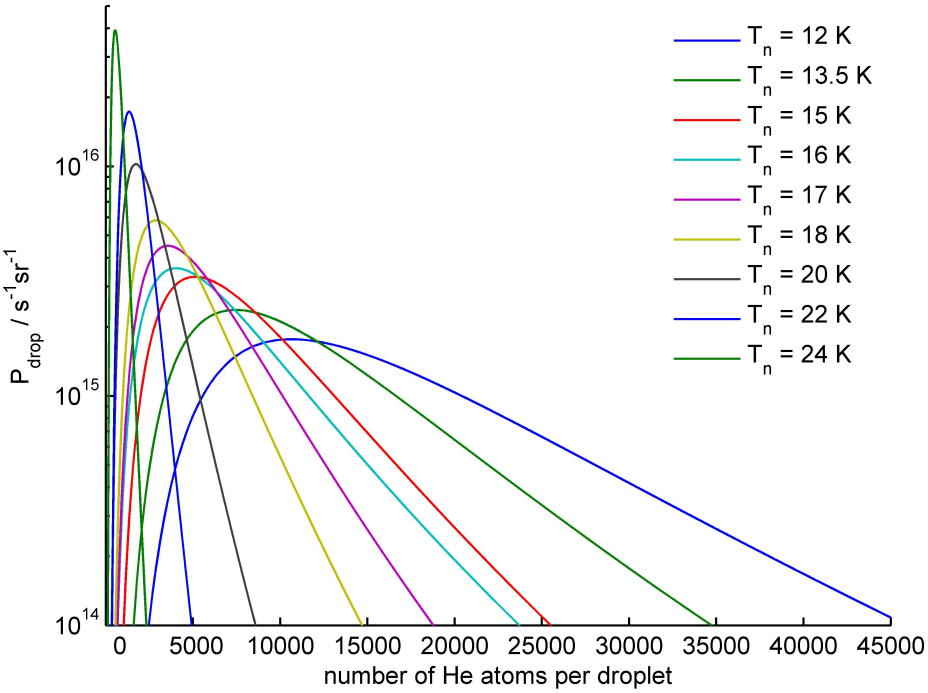

Figure 7.3.: Semilogarithmic plot of calculated He droplet numbers with a stagnation pressure of 40 bar. With higher temperatures the droplets shrink in size and the distributions become narrower.

In Fig. 7.3 calculated numbers of He droplets P_{drop} are displayed for different nozzle temperatures.

The pick-up of any particle leads to an energy transfer from the kinetic energy of the dopant ($E = \frac{k_b T}{2}$) into the evaporation of He atoms from the droplet ($\sim 5\,\mathrm{cm}^{-1}$ per He atom[26]). By this process the droplets shrink in size. The droplet size distribution as well as its proposed shrinking will be of importance in the next Sections, when observing larger Ak clusters of Rb and Cs.

7.3. Experimental

He nanodroplets are generated using our droplet beam apparatus, which has already been described in Refs. 2,46. In brief, He_N are formed in a supersonic expansion of He gas (Air Liquide, Alphagaz 2, grade 6.0) with a stagnation pressure of 40 bar through a 5 μm nozzle. The average size $\bar{N}$ of the He_N can be steered by varying the nozzle temperature[26]. After creation the nanodroplets are doped by passing through Ak vapor located in a heated pick-up cell, which contains bulk Ak. Rb and Cs samples are loaded into the pick-up cell under argon gas. The cell is operated at ~ 405 K for Rb and

$\sim 390\,\mathrm{K}$ for Cs in order to generate about $1 - 2 \times 10^{-3}\,\mathrm{mbar}$ vapor pressure.

When several atoms are picked up by one He nanodroplet Ak clusters are formed in the cold environment. Energy considerations favor the survival of nanodroplets with spin polarized Ak atom clusters, which can be explained by looking at the example of Rb dimers. The binding energy E_b of Rb_2 strongly depends on the spin states, with $E_b = 3875\,\mathrm{cm}^{-1}$ for singlet states and $252\,\mathrm{cm}^{-1}$ for triplets[161]. Under usual thermal conditions only the singlet state can be observed due to its higher stability. On the He nanodroplet the large binding energy when forming low-spin clusters leads to a large release of energy into the nanodroplet. This excess energy causes evaporation of He ($\sim 5\,\mathrm{cm}^{-1}$ per He atom[26]), so that the He nanodroplets shrink in size and can be destroyed. In general, the smaller the binding energy the more probable will be the existence of large Ak clusters on He_N. The pick-up process for Ak clusters itself shows a non-Poissonian behavior[46,47], which is a convolution of the Poissonian pick-up and a spin-dependent component.

We have summarized available calculated binding energies E_b of Rb and Cs for clusters in high- and low-spin states in Tab. 7.2, whereby the binding energies for Rb and Cs are of the same order. Ab initio studies of cesium (Cs), sodium (Na) and potassium (K) clusters in their low-spin states have been published for $n \leq 20$ (Na: $n \leq 10$, K: $n \leq 20$). By trend, the calculated total binding energy divided by the cluster size ("binding energy per atom") increases with the cluster size.[162–164]. So far, only for Li_n and Na_n ($n = 1 - 12$) the binding energies in their high-spin states have been derived in a systematic comparison (cf. Ref. 158). We assume a similar qualitative behavior for Rb and Cs.

A time-of-flight (TOF) mass spectrometer (Jordan, angular reflectron time of flight D-850) is placed along the beam axis about 35 cm downstream from the pick-up cell, which allows us to detect all ionized molecules at one time. The Ak_n loaded He nanodroplets are photo-ionized (Ti:Al_2O_3 laser, Coherent Indigo, repetition rate 5 kHz, pulse width $< 0.5\,\mathrm{cm}^{-1}$ for the fundamental wavelength, pulse length $\sim 30\,\mathrm{ns}$, frequency doubling and tripling available). The used photon energies as well as the pulse fluences are given in Tab. 7.3. The ionization threshold of bare Rb (Cs) atoms is known as $33691\,\mathrm{cm}^{-1}$ ($31406\,\mathrm{cm}^{-1}$). The one of Cs_2 is reported as $\sim 29200\,\mathrm{cm}^{-1}$ from the $^1\Sigma_g^+$ state[116,167] and $\sim 26000\,\mathrm{cm}^{-1}$ from the $^3\Sigma_u$ state. For Cs_3 an ionization limit of $24690 \pm 30\,\mathrm{cm}^{-1}$ can be found in Ref. 167. As the ionization threshold decreases with n down to the bulk value, which is equivalent to the work function (Rb: 2.1 eV, Cs: 1.9 eV)[118], the chosen photon energies of frequency doubled and tripled Ti:Al_2O_3 radiation allow to ionize large clusters by an one-photon process, which is essential for avoiding strong fragmentation. Critical Ak_n cluster sizes for submersion as calculated in Ref. 168 are not reached, so that they tend to reside in a dimple on the surface of the He nanodroplet. Moreover, bulk

Table 7.2.: Total binding energies for small Rb and Cs clusters in different spin states given in cm^{-1}. In addition, the numbers of He atoms is given, which evaporate through the cluster formation process and the Ak atom pick-up process (Rb: ~ 170 He atoms per pick-up, Cs: ~ 240)[45] from He_N as given in Ref. 26.

	low-spin		high-spin		
Cluster	cm^{-1}	evaporated He atoms	cm^{-1}	evaporated He atoms	Reference
Rb_2	3875	1120	250	390	161
Rb_3	5321	1580	939	700	165
Cs_2	3629	1210	267	530	161
Cs_3	-		1144	950	166
Cs_3	4597	1650	-		162
Cs_4	7130	2400	-		162
Cs_5	8711	2950	-		162
Cs_6	11227	3700	-		162
Cs_7	16204	4940	-		162
Cs_8	18970	5740	-		162
Cs_9	24753	7140	-		162
Cs_{10}	28149	8070	-		162
⋮	⋮	⋮	⋮	⋮	⋮
Cs_{20}	63556	17590	-		162

Cs is not wetted by superfluid He,[169] so that immersion into the He_N is unlikely. With our measurement technique we cannot determine, if larger Ak clusters are wetted or not.

7.4. Results and discussion

Variation of the nanodroplet size was achieved by changing the nozzle temperature at a fixed helium backing pressure of 40 bar and nozzle diameter of 5 μm. References 26 and 29 present scaling laws for the mean helium nanodroplet size and the size distribution versus nozzle temperature and pressure. At 40 bar, the data and corresponding curves become somewhat unreliable for nozzle temperatures below 13 K. Below about 10.5 K, an abrupt change occurs when the expansion conditions change from subcritical to supercritical where much larger nanodroplets, up to several 10^6 He atoms each, are formed. It seems that the scaling displayed in Ref. 26 overestimates nanodroplet sizes under subcritical conditions in the 11 to 13 K range. In this range, there is a considerable deviation from the scaling formula given by Knuth[160]. In the higher temperature range,

Table 7.3.: Photon energies and estimated pulse fluence applied in the experiments for the different ionization processes and Ak clusters

Ak	photon energy (cm^{-1})	pulse fluence ($^{mJ}/_{cm^2}$)	ionization process
Rb	33584	~ 0.7	one-photon
Cs	32955	~ 1.0	one-photon
Cs	26535	~ 2.6	one- and multi-photon
Cs	11200	~ 28.0	multi-photon

the results of the different authors agree reasonably well. We used Knuth's results for $\bar{N}_i$. A lognormal distribution was applied for $T_n = 12.0$, 13.5 and 15 K[29] in order to calculate survival chances (Tab. 7.4) for He nanodroplets loaded with Ak_n clusters setting free a corresponding amount of energy and burning off the number of He atoms listed in Tab. 7.2. This means that we took into account the complete size distribution including the large sizes as correctly as possible in this model. At large initial nanodroplet sizes ($\bar{N}_i \sim 18600$ He atoms) we monitored cluster sizes up to $n = 30$ (21) atoms for Rb (Cs) with one-photon ionization (Fig. 7.4). The signals at cluster sizes $n = 5, 9$ compared to the one at cluster sizes $n - 1$ and $n + 1$ are larger, which can be interpreted as stable Ak_n^+ formations. This agrees with theoretical investigations of W. Ekardt et al.[170]. Moreover, the signal alternates between even and odd n. The actual measured intensities do therefore not reflect the stability of Ak_n cluster on the He_N, but directly reflect the stability of Ak_n^+. The different absolute values for the different species can be explained by different excess energies and dissociation energies of the Ak_n^+. Besides, it is obvious that the cluster size in the case of Rb exceeds the one of Cs, which reflects the larger amount of energy deposited into the nanodroplet by pick-up and bonding for Cs than for Rb. Major electronic shell closures in free Ak_n ($n = 8, 20, 40, ...$) can be found in the experimental pioneer work of this topic[171]. In several review articles (e.g. Ref. 172) further shell closures ($n = 18, 34, ...$) are discussed. Please note, that our measured abundances can have systematic errors due to (a) the lower sensitivity of our detector at higher masses and (b) the influence of a further electrical field in the TOF apparatus, which is needed to direct the ions into the detector.

In the previous work of C. P. Schulz et al.[157], who observed only sizes of up to $n = 5(3)$ atoms for Rb (Cs) clusters, it was argued that the large SO-coupling of these two Ak atoms results in a spin flip, where excess energy is converted into the evaporation of He atoms[157]. It was further argued that the nonexistence of stable high-spin states for larger cluster sizes is evidently shown by the non-observation of cluster sizes beyond $n = 5(3)$.[35,157].

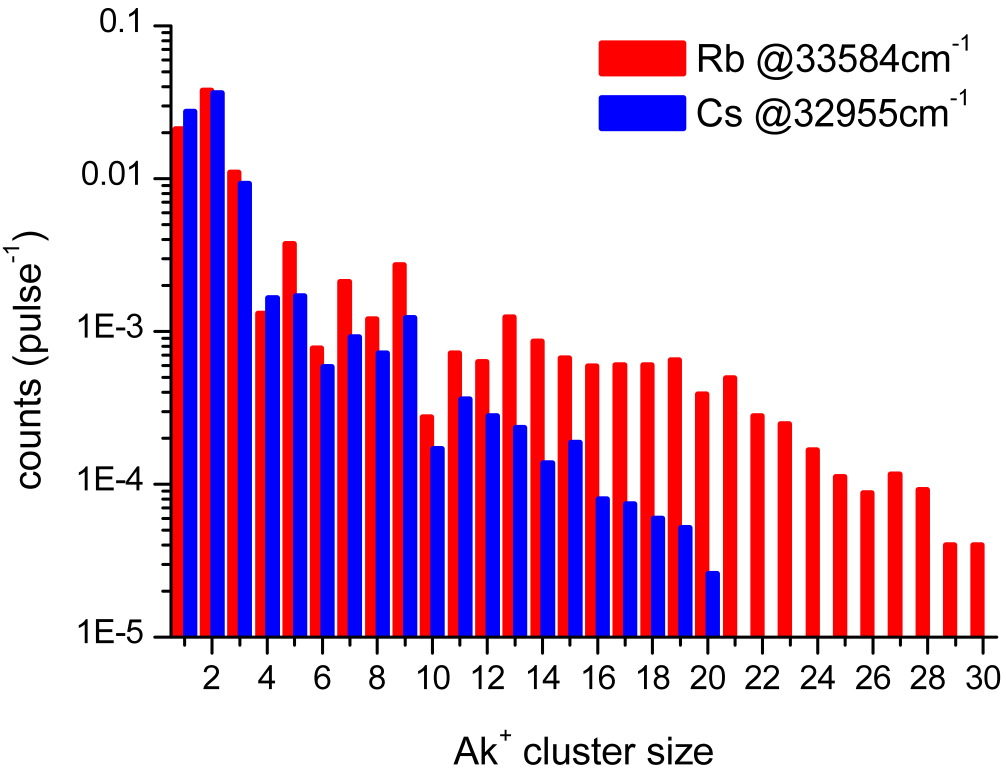

Figure 7.4.: Size distribution of Rb_n^+ (red) and Cs_n^+ (blue) clusters per laser pulse. The size distribution reflects the stability of such clusters. Features of the prominent signals at $n = 5$ and $n = 9$ are explained in the text as well as those at $n = 21$ and $n = 28$.

In our one-photon ionization data for Rb and Cs we see prominent ion intensities at $n = 5$ and $n = 9$, which were previously monitored for sodium (Na) and potassium (K)[157]. In this previous work, another maximum for $n = 21$ (K) was shown. We cannot find such a strong maximum for Rb (Cs) in our TOF experiments, but we also see an increased signal for Rb_{21}^+. In addition to those three stable cluster sizes, we find a strong decrease in intensity beyond $n = 28$ (Fig. 7.4).

To determine the open question, if we see low- or high-spin states of Ak clusters we further observed Cs clusters in two ways: i) we used different photon energies and ii) we used different initial nanodroplet sizes.

i) Three different photon energies: $\tilde{\nu} = 32955$, 26535 and $11200\,\mathrm{cm}^{-1}$ were used, to study the competition between one-photon ionization and multi-photon ionization in the

case of large initial nanodroplets sizes ($\bar{N}_i \sim 18600$ He atoms). In the multi-photon ionization scheme ($\tilde{\nu} = 11200\,\mathrm{cm}^{-1}$) we can identify only oligomers up to $n = 3$ (Fig. 7.5), which is in agreement with Refs. 35,157.

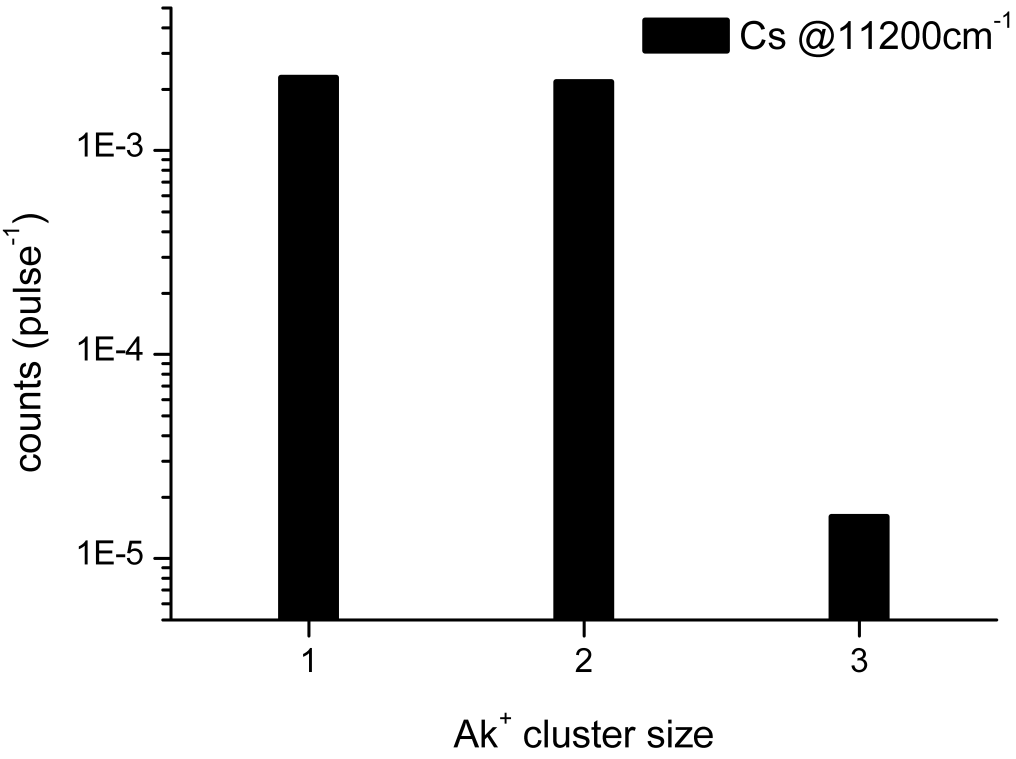

Figure 7.5.: Size distribution of Cs_n^+ clusters obtained at $\tilde{\nu} = 11200\,\mathrm{cm}^{-1}$. Features of the signals are explained in the text.

For a photon energy of $\tilde{\nu} = 32955\,\mathrm{cm}^{-1}$ only one-photon ionization will occur. For $\tilde{\nu} = 26535\,\mathrm{cm}^{-1}$ we assume that at least trimers are ionized directly. A comparison for the two different photon energies is plotted in Fig. 7.6. By trend, the two plots show the same stable cluster sizes at prominent numbers ($n = 5, 9, 19$) and an even-odd alternation. The difference in signal heights for $n = 1, 2$ and $n \geq 2$ for both photon energies can be well explained. The energy difference between photon energy and ionization threshold leads to fragmentation, where the most stable complexes in this process are $n = 1, 2$. With a photon energy of $\tilde{\nu} = 32955\,\mathrm{cm}^{-1}$ more fragmentation will occur than in the case of $\tilde{\nu} = 26535\,\mathrm{cm}^{-1}$, for which the ratio of signals at $n = 1, 2$ and $n \geq 2$ is lower. We can see that the ionization process plays a large role, especially for the multi-photon ionization, where no larger clusters than $n = 3$ can be found.

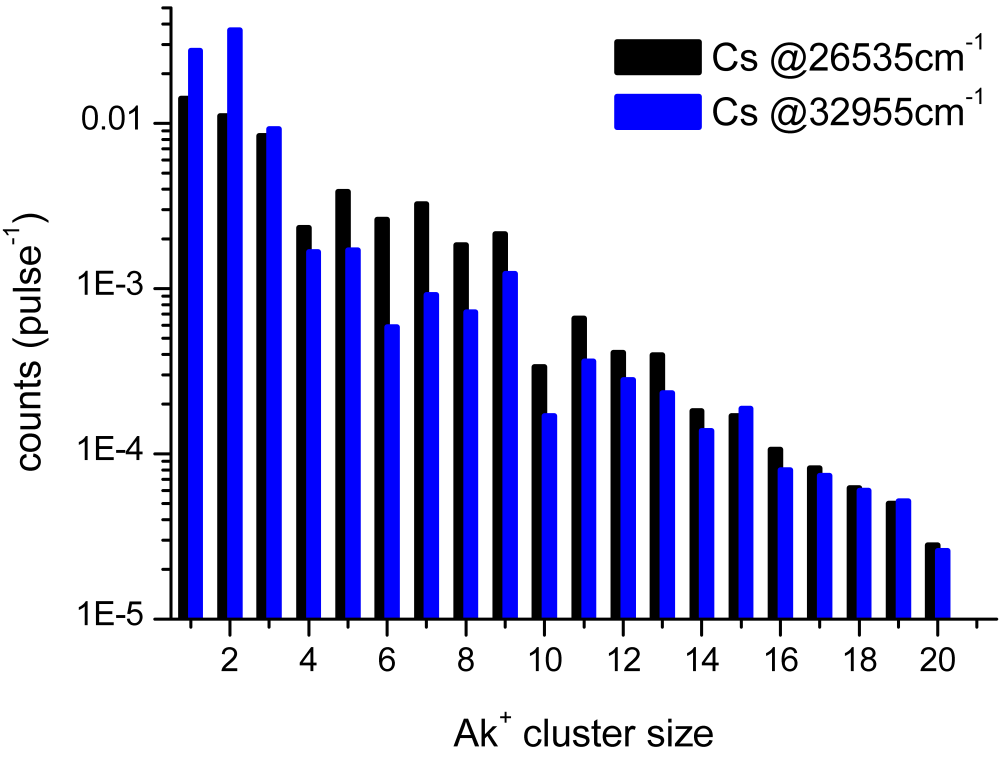

Figure 7.6.: Size distribution of Cs_n^+ clusters obtained at different photon energies per laser pulse. Features of the signals are explained in the text.

ii) The initial nanodroplet size was varied by changing the nozzle temperature, while we kept the photon energy fixed ($\tilde{\nu} = 32955\,\mathrm{cm}^{-1}$). In Fig. 7.7 we plotted the measured intensities of Cs_n^+ clusters ($n = 2, 3, 5, 7, 9$) for different He_N sizes.

At large initial nanodroplet sizes we can identify all Cs_n^+ sizes. At smaller nanodroplet size the signal shrinks for all sizes. When we compare the signals for $n = 2, 3, 5, 7, 9$ for different nanodroplet sizes, we see that the decrease of signals for $n = 5, 7, 9$ compared to those of $n = 2, 3$ is stronger for small initial droplet sizes than for large ones.

The probabilities to form Ak_n in a high-spin configuration was derived in Ref. 47 and is given as $\frac{n+1}{2^n}$. For $n = 9$ this is $\sim 2.0\%$ ($n = 7$: $\sim 6.3\%$, $n = 5$: $\sim 18.8\%$, $n = 3$: 50.0%, $n = 2$: 75.0%). All others will release additional energy by a spin-flip process[47] or by the higher binding energy of low-spin configurations. There is no indication that a spontaneous spin-flip of high-spin clusters occurs on He_N. Therefore we believe that the nanodroplets carry Ak_n in both spin configurations limited only by the energy released through pick-up and formation. On large nanodroplets, this gives room for cold Ak_n of

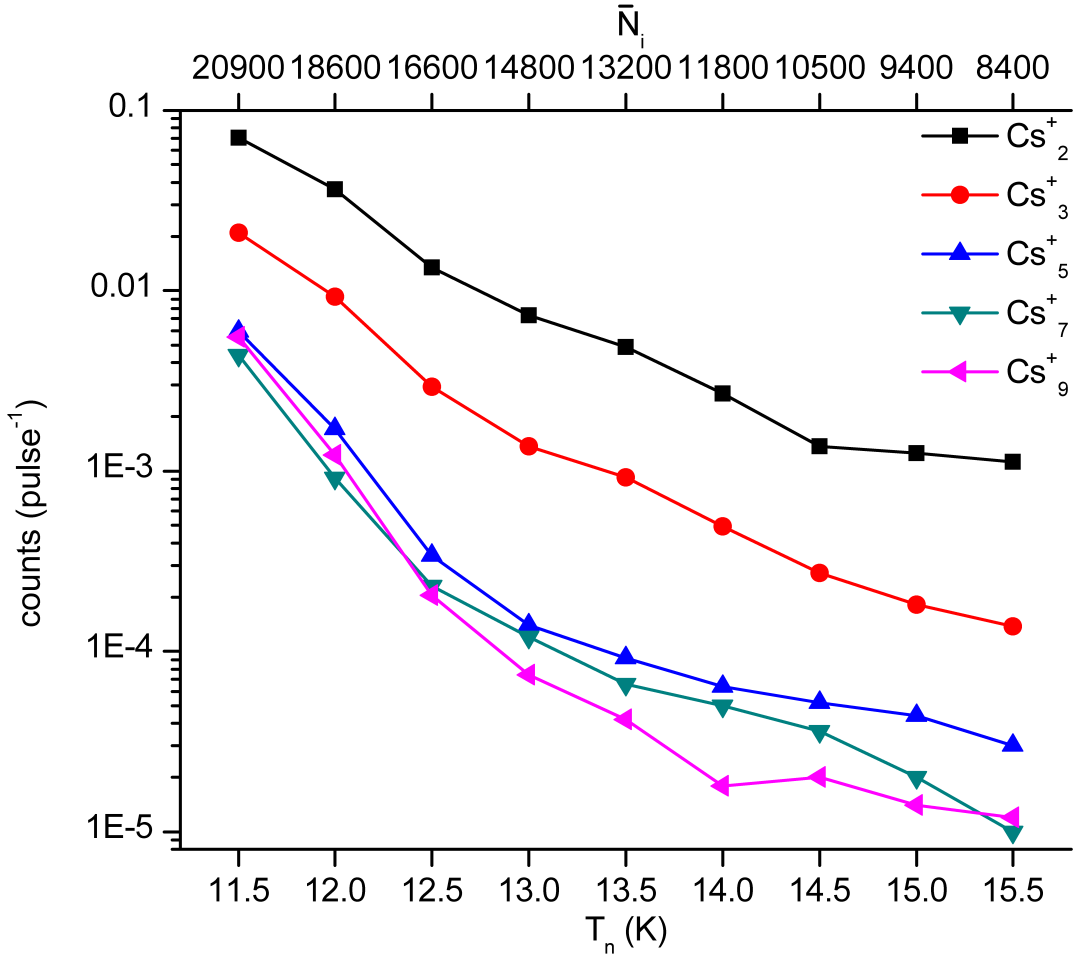

Figure 7.7.: Measured intensity for Cs_n^+ ($n = 2, 3, 5, 9$) per laser pulse obtained at different nozzle temperatures. Initial nanodroplet sizes $\bar{N}_i$ given in number of He atoms have been estimated using the model given in Ref. 160.

high- and low-spin.

We do not have an explicit proof for the existence of high-spin clusters of Cs_n with $n > 3$. But to underline the existence of high-spin Ak_n, we compare the energy release with the subsequent survival chance of the nanodroplet for different nanodroplet sizes.

The formation probability does not mean that the Ak_n in a certain spin-configuration survives the formation process, because of a spin-dependent energy release, which is transformed into He evaporation. The survival chance of the Ak_n loaded nanodroplet can be estimated by comparing the energy release due to the pick-up process of Cs atoms ($\sim 1200\,\mathrm{cm}^{-1}$ per Cs atom according to Ref. 45, which is equivalent to the evaporation of 240 He atoms) and the Cs cluster formation (Tab. 7.2) with the nanodroplet size.

With this, the total shrinking of the nanodroplet given in He atoms can be estimated for $n = 2$: ~ 1200 (~ 530, high spin), $n = 3$: ~ 1650 (~ 950, high spin), $n = 5$: ~ 2950, $n = 7$: ~ 4940, $n = 9$: ~ 7140 (only low-spin values known).

There are several models, which estimate the He atoms burned off before the Ak_n desorbs: (i) Vongehr and Kresin proposed that, if the spin becomes less than maximal, the Ak_n cluster relaxes back into the low-spin ground state and desorbs. The nanodroplet, which is decreased in size, can pick up Ak atoms again.[47] Recently published results favor a model (ii), where only the burn-off of He atoms near the droplet surface is allowed for the aggregate to remain stable. More burn-off leads to a blowing of the whole cluster.[30] This would mean that mostly high-spin states have a chance to survive. For example, assuming a uniform He density, nanodroplets with the size of 8400 He atoms have ~ 1180 He atoms in the outer shell region, which is equivalent to a maximum energy release of $\sim 5900\,\mathrm{cm}^{-1}$. In this case the abundance of Cs_9 becomes improbable for smaller nanodroplet sizes. By comparing the approximate number of outer He atoms with the total energy release we can estimate, if a cluster can survive the formation process according to model (ii) (cf. Tab. 7.4). The extreme case (iii) that all He atoms have to evaporate before disintegration seems rather unlikely, but will be considered. With model (ii) and (iii) we estimate the survival chances for low-spin Cs_n. We compare the initial nanodroplet size distribution as given in Ref. 29 with the proposed shrinking in size due to the pick-up process of Cs atoms ($\sim 1200\,\mathrm{cm}^{-1}$ per Cs atom according to Ref. 45, which is equivalent to the evaporation of ~ 240 He atoms) and the Cs cluster formation (Tab. 7.2). The He_N distribution for $T_n = 12\,\mathrm{K}$ was estimated by extrapolating the experimental data. By transforming the nanodroplet size distribution from He atoms into energy (1 He atom equals $\sim 5\,\mathrm{cm}^{-1}$) and comparing this with the total energy release due to pick-up and cluster formation we can estimate the chance of survival of the nanodroplet (cf. Tab. 7.4). The normalized size distribution was integrated from zero to the He_N size needed for a total burn off (model (iii), Cs_9: 7140 He atoms). The average size within the droplet distribution must not be mixed up with the most probable droplet size. E.g. nanodroplets with $\overline{N}_i = 13000$ He atoms consist to $\sim 25\%$ of sizes smaller than 7140 He atoms so that $\sim 75\%$ can survive the formation process according to model (iii). On the other hand, droplets with $\overline{N}_i = 18600$ He atoms consist to $\sim 42\%$ of sizes larger than 18000 He atoms so that $\sim 42\%$ can survive the formation of low-spin Cs_{20}. This extreme example should only tell us that there is some chance of these He droplets to carry even a low-spin Cs_{20}. How about high-spin Cs clusters? Unfortunately the binding energies per atom are not known. For high-spin clusters of Li and Na, de Visser, Danovich, and Shaik (Ref. 158) calculated the corresponding values with the result that for cluster sizes around 10, they approach about three times the value of the high-spin trimer binding energy per atom. If we take our own calculated high-spin Cs_3 binding energy of $1144\,\mathrm{cm}^{-1}$ (cf. Tab. 7.2, Ref. 166),

i.e. about $400\,\mathrm{cm}^{-1}$ per atom, we may use about $1200\,\mathrm{cm}^{-1}$ per atom for a Cs_{10} to Cs_{20} binding estimate. Including the energy release per pick-up, formation of a Cs_{10} high-spin cluster should burn off ~ 4800 He atoms, formation of high-spin Cs_{20} should reduce the droplet by ~ 9600 He atoms, roughly half of the evaporation caused by low-spin Cs_{20} (cf. Tab. 7.2). According to model (iii), almost 90% of the droplets with $\overline{N}_i = 18600$ would survive formation of high-spin Cs_{20} compared to 42% for low-spin formation. According to Fig. 7.6 the Cs_{20} signal of $\sim 3 \times 10^{-5}$ counts/pulse compares with the Cs signal of $\sim 3 \times 10^{-2}$ counts/pulse, which indicates a relative abundance of 10^{-3}. The formation probability if high-spin Cs_{20} is only 2×10^{-5} but its survival rate should be high.

As for model (ii), the number of He atoms in the droplet surface layer is ~ 440 for a He_{2000} droplet and ~ 10000 for He_{100000} assuming an average He-He separation of $0.222\,\mathrm{nm}$[27]. If only the evaporation of the surface layer should be decisive for the survival of droplets, we should not have detected Cs_{20} at all. Model (i) with relaxation of intermediate spin configuration and subsequent desorption, can unfortunately not be commented by us, because we have no way to observe intermediate processes.

Table 7.4.: Estimated survival chances for He nanodroplets according to model (ii) and (iii) after formation of Cs_n (low-spin)

T_n (K)	$\overline{N}_i$	model	Cs_3	Cs_5	Cs_7	Cs_9	Cs_{20}
12.0 K	~ 18600	(ii)	$\sim 58\%$	$\sim 11\%$	$\sim 1\%$	$< 1\%$	$< 1\%$
		(iii)	$> 99\%$	$> 99\%$	$\sim 97\%$	$\sim 90\%$	$\sim 42\%$
13.5 K	~ 13000	(ii)	$\sim 35\%$	$\sim 4\%$	$< 1\%$	$< 1\%$	$< 1\%$
		(iii)	$> 99\%$	$\sim 98\%$	$\sim 90\%$	$\sim 75\%$	$\sim 21\%$
15.0 K	~ 9000	(ii)	$\sim 15\%$	$< 1\%$	$< 1\%$	$< 1\%$	$< 1\%$
		(iii)	$> 99\%$	$\sim 94\%$	$\sim 75\%$	$\sim 50\%$	$\sim 7\%$

We have no indication that the Ak clusters dissociate or change their spin configuration on the cold nanodroplets unless they are excited or ionized with laser radiation. Therefore we believe that the nanodroplets carry Ak_n in both spin configurations limited only by the energy released through pick-up and formation. On large nanodroplets, this gives room for cold Ak_n of high- and low-spin.

7.5. Conclusions

We have shown that Rb_n (Cs_n) with $n > 5$ ($n > 3$) on He_N exist. The detection process, here photo-ionization, has a strong influence on fragmentation of the Ak_n. Only

one-photon ionization leads to a conclusive observation of meaningful cluster size distributions. The excess energy has an influence on the Ak_n^+ distribution, too. Based on energy considerations, we believe that we find both low-spin and high-spin Ak_n cluster configurations for Cs_n ($n > 3$).

The bonding character of high- and low-spin Ak_n differs strongly with large magnetic moments in the first case[73] and delocalization of valence electrons in the second[74]. It will therefore be interesting to examine two types in detail experimentally. Studies in inhomogeneous magnetic (Stern-Gerlach)[173] and electric fields[174] may offer the chance for deeper insights.

8. Summary

The present work investigates the interaction of single rubidium (Rb) and cesium (Cs) atoms with helium droplets (He_N), the interaction of positively charged Rb and Cs ions with He_N, and the examination of small Rb and Cs clusters on He_N. The main results are summarized below.

Rb and Cs atoms on He droplets

Alkali-metal atoms are surface-located when picked up by He droplets. They tend to form a dimple on the surface of the He_N with a dimple size correlated to the Ak atom size. Due to the surface location one can describe the system in a pseudo-diatomic model with the Ak atoms as one atom and the He droplet as other. Normally, the Ak atoms detach from the surface when electronically excited. When Rb (Cs) atoms are excited with photon energies close to the D_1-line of the bare atom they show an unusual behavior: this excited state system is stable, meaning that the Ak atom does not desorb and relaxes back into its electronic ground state fully attached to the He droplet. The atom can be re-excited from its ground state. Experimental investigations can be explained by theoretical findings, which underline the stability of this fragile system. In addition, Rb (Cs) can then be further excited from this first excited state $n^2P_{1/2}$ ($^2\Pi_{1/2}$) (Rb: $n = 5$, Cs: $n = 6$) to higher electronic states.

Interaction between Rb^+ and Cs^+ ions and He droplets

The alkali-metal atom polarizes the He atoms only slightly, so that the alkali-metal atom does not immerse into the He droplet. The interaction between Ak atom and He droplet changes dramatically when an electron is removed. The Ak^+ polarizes He atoms in a much stronger way, so that He atoms try to surround the positively charged ion. The depth well between Ak^+ and He is so deep that the mean distance between two He atoms lies in the repulsive part of the corresponding potential energy curves. As a conclusion the He density exceeds the crystallization limit and one speaks of a *snowball*. In our experiments we find shells and magic numbers of He atoms around the Ak^+, which agree well with theoretical findings. In addition Cs_2^+-He_m also shows a preferred structure.

The strong interaction can also be used to locate a positive charge in the He droplet: a single Rb (Cs) ion can be created in a resonant two-photon ionization (R2PI) scheme on the surface of the droplet when using the non-desorbing $n^2P_{1/2}$ ($^2\Pi_{1/2}$) state. In time-of-flight mass spectra one can clearly identify the immersion of the ion into the droplet at large masses (> 4000 amu). Only ionization through the non-desorbing $n^2P_{1/2}$ ($^2\Pi_{1/2}$) state leads to a high ion yield of Ak^+-He_N.

Due to the strong attraction between positively charge Ak core and He droplet the ionization threshold is lowered by a small amount. This effect depends on the size of the He droplet. For large He droplets the shift in the IT is stronger than for small droplets. A comparison with Na atoms shows that this shift is also a function of the alkali-metal species. The diatomic Ak^+He energy potentials help to explain the trend that ΔIT is larger for light Ak ions (Na^+) than for heavy Ak^+ ions (Rb^+, Cs^+).

Rb and Cs clusters on He droplets

Alkali-metal clusters can be created on He droplets by the pick-up of single Ak atoms and a subsequent cluster formation process. In general, high-spin clusters have a lower binding energy than low-spin states so that the preferred cluster state should be a low-spin state. On He droplets the binding energy is transformed into the evaporation of He atoms, which goes along with a possible destruction of the droplet. Therefore on He droplets high-spin states are favorably observed. In our time-of-flight mass spectra we see Ak_n cluster sizes up to $n = 30$ (Rb) and $n = 20$ (Cs). A comparison between monitored clusters sizes at different He droplet sizes with binding energies and formation probabilities let us assume that we observe both, high-spin and low-spin cluster of these sizes.

Bibliography

[1] M. Theisen, F. Lackner, F. Ancilotto, C. Callegari, and W. E. Ernst, European Physical Journal D **61**, 403 (2011).

[2] M. Theisen, F. Lackner, and W. E. Ernst, Phys. Chem. Chem. Phys. **12**, 14861 (2010).

[3] M. Theisen, F. Lackner, and W. E. Ernst, J. Phys. Chem. A **115**, 7005 (2011).

[4] M. Theisen, F. Lackner, and W. E. Ernst, J. Chem. Phys. **135**, 074306 (7 pages) (2011).

[5] F. Lackner, G. Krois, M. Theisen, M. Koch, and W. E. Ernst, Phys. Chem. Chem. Phys. in press (2011).

[6] J. P. Toennies, Physik Journal **7**, 49 (2002).

[7] W. H. Keesom, *Helium* (Elsevier, Amsterdam, 1942).

[8] S. D. Bergeson, A. Balakrishnan, K. G. H. Baldwin, T. B. Lucatorto, J. P. Marangos, T. J. McIlrath, T. R. O'Brian, S. L. Rolston, C. J. Sansonetti, J. Wen, et al., Phys. Rev. Lett. **80**, 3475 (1998).

[9] L. Landau, Journal of Physics, USSR **5**, 71 (1941).

[10] P. L. Kapitza, Nature **141**, 74 (1938).

[11] J. F. Allen and A. D. Misener, Nature **141**, 75 (1938).

[12] E. L. Andronikashvili, Journal of Physics, USSR **10**, 201 (1946).

[13] L. Tisza, Nature **141**, 913 (1938).

[14] P. V. E. McClintock, Z. Phys. B **98**, 429 (1995).

[15] R. J. Donnelly, *Quantized Vortices in Helium II* (Cambridge University Press, 1991).

[16] A. D. B. Woods and R. A. Cowley, Reports on Progress in Physics **36**, 1135 (1973).

[17] K. T. Tang, J. P. Toennies, and C. L. Yiu, Phys. Rev. Lett. **74**, 1546 (1995).

[18] K. Tang and J. Toennies, J. Chem. Phys. **118**, 4976 (2003).

[19] R. E. Grisenti, W. Schollkopf, J. P. Toennies, G. C. Hegerfeldt, T. Kohler, and M. Stoll, Phys. Rev. Lett. **85**, 2284 (2000).

[20] W. Schöllkopf and J. P. Toennies, Science **266**, 1345 (1994).

[21] W. Schöllkopf and J. P. Toennies, J. Chem. Phys. **104**, 1155 (1996).

[22] E. W. Becker, R. Klingelhöfer, and P. Lohse, Z. Naturforsch. A **16A**, 1259 (1959).

[23] D. R. Miller, *Atomic and Molecular Beam Methods* (Oxford University Press, New York, 1988), vol. 1, chap. 2. Free Jet Sources, pp. 14–53.

[24] H. Pauly, *Atom, Molecule, and Cluster Beams I*, vol. 28 of *Springer series on atomic, optical, and plasma physics* (Springer, New York, 2000).

[25] K. Bier and B. Schmidt, Z. Angew. Phys. **13**, 493 (1961).

[26] J. P. Toennies and A. F. Vilesov, Angewandte Chemie International Edition **43**, 2622 (2004).

[27] D. Brink and S. Stringari, Z. Phys. D **15**, 257 (1990).

[28] A. Guirao, M. Pi, and M. Barranco, Z. Phys. D **21**, 185 (1991).

[29] J. Harms, J. P. Toennies, and F. Dalfovo, Phys. Rev. B **58**, 3341 (1998).

[30] O. Bünermann and F. Stienkemeier, Eur. Phys. J. D **61**, 645 (2011).

[31] V. Mozhayskiy, M. N. Slipchenko, V. K. Adamchuk, and A. F. Vilesov, J. Chem. Phys. **127**, 94701 (6 pages) (2007).

[32] S. Stringari and J. Treiner, J. Chem. Phys. **87**, 5021 (1987).

[33] F. Stienkemeier and K. K. Lehmann, J. Phys. B **39**, R127 (2006).

[34] M. Y. Choi, G. E. Douberly, T. Falconer, W. K. Lewis, C. M. Lindsay, J. M. Merritt, P. Stiles, and R. E. Miller, Int. Rev. Phys. Chem. **25**, 15 (2006).

[35] J. Tiggesbäumker and F. Stienkemeier, Phys. Chem. Chem. Phys. **9**, 4748 (2007).

[36] E. Lugovoj, J. P. Toennies, and A. F. Vilesov, J. Chem. Phys. **112**, 8217 (2000).

[37] S. Müller, S. Krapf, T. Koslowski, M. Mudrich, and F. Stienkemeier, Phys. Rev-Lett. **102**, 183401 (4 pages) (2009).

[38] S. A. Krasnokutski and F. Huisken, J. Phys. Chem. A **115**, 7120 (2011).

[39] J. Higgins, C. Callegari, J. Reho, F. Stienkemeier, W. E. Ernst, K. K. Lehmann, M. Gutowski, and G. Scoles, Science **273**, 629 (1996).

[40] F. Bierau, P. Kupser, G. Meijer, and G. von Helden, Phys. Rev. Lett. **105**, 133402 (4 pages) (2010).

[41] P. Claas, S.-O. Mende, and F. Stienkemeier, Rev. Sci. Instr. **74**, 4071 (2003).

[42] M. Ratschek, Master's thesis, Graz University of Technology (2010).

[43] T. E. Gough, M. Mengel, P. A. Rowntree, and G. Scoles, J. Chem. Phys. **83**, 4958 (1985).

[44] A. Scheidemann, J. P. Toennies, and J. A. Northby, Phys. Rev. Lett. **64**, 1899 (1990).

[45] M. Lewerenz, B. Schilling, and J. P. Toennies, J. Chem. Phys. **102**, 8191 (1995).

[46] J. Nagl, A. W. Hauser, G. Auböck, C. Callegari, and W. E. Ernst, J. Phys. Chem. A **111**, 12386 (2007).

[47] S. Vongehr and V. V. Kresin, J. Chem. Phys. **119**, 11124 (2003).

[48] F. Dalfovo, Z. Phys. D **14**, 263 (1989).

[49] F. Stienkemeier, J. Higgins, W. E. Ernst, and G. Scoles, Phys. Rev. Lett. **74**, 3592 (1995).

[50] F. Stienkemeier, W. E. Ernst, J. Higgins, and G. Scoles, J. Chem. Phys. **102**, 615 (1995).

[51] F. Stienkemeier, F. Meier, and H. O. Lutz, J. Chem. Phys. **107**, 10816 (1997).

[52] F. Ancilotto, P. B. Lerner, and M. W. Cole, J. Low Temp. Phys. **101**, 1123 (1995).

[53] J. Harms, M. Hartmann, S. Sartakov, J. P. Toennies, and A. Vilesov, J. Mol. Spectr. **185**, 204 (1997).

[54] S. Grebenev, M. Hartmann, M. Havenith, B. Sartakov, J. P. Toennies, and A. F. Vilesov, J. Chem. Phys. **112**, 4485 (2000).

[55] Y. Takahashi, K. Sano, T. Kinoshita, and T. Yabuzaki, Phys. Rev. Lett. **71**, 1035 (1993).

[56] F. Stienkemeier, J. Higgins, W. E. Ernst, and G. Scoles, Z. Phys. B **98**, 413 (1995).

[57] F. Stienkemeier, J. Higgins, C. Callegari, S. I. Kanorsky, W. E. Ernst, and G. Scoles, Z. Phys. D **38**, 253 (1996).

[58] J. Higgins, C. Callegari, J. Reho, F. Stienkemeier, W. E. Ernst, M. Gutowski, and G. Scoles, J. Phys. Chem. A **102**, 4952 (1998).

[59] F. R. Brühl, R. A. Trasca, and W. E. Ernst, J. Chem. Phys. **115**, 10220 (5 pages) (2001), Iss. 22. Special Topic: *Helium nanodroplets: a novel medium for chemistry and physics.*

[60] G. Auböck, J. Nagl, C. Callegari, and W. E. Ernst, Phys. Rev. Lett. **101**, 035301 (4 pp.) (2008).

[61] A. Pifrader, O. Allard, G. Auböck, C. Callegari, W. E. Ernst, R. Huber, and F. Ancilotto, J. Chem. Phys. **133**, 164502 (7 pages) (2010).

[62] M. Buzzacchi, D. E. Galli, and L. Reatto, Phys. Rev. B **64**, 94512 (10 pages) (2001).

[63] F. Marinetti, E. Coccia, E. Bodo, F. Gianturco, E. Yurtsever, M. Yurtsever, and E. Yildirim, Theoretical Chemistry Accounts **118**, 53 (2007).

[64] F. Marinetti, L. Uranga-Pina, E. Coccia, D. Lopez-Duran, E. Bodo, and F. Gianturco, J. Phys. Chem. A **111**, 12289 (2007).

[65] M. Rossi, M. Verona, D. E. Galli, and L. Reatto, Phys. Rev. B **69**, 212510 (4 pages) (2004).

[66] A. Nakayama and K. Yamashita, J. Chem. Phys. **112**, 10966 (2000).

[67] C. C. Duminuco, D. Galli, and L. Reatto, Physica B **284-288**, 109 (2000).

[68] X. Bu and C. Zhong, Journal of Molecular Structure: THEOCHEM **726**, 99 (2005).

[69] D. E. Galli, D. M. Ceperley, and L. Reatto, J. Phys. Chem. A **115**, 7300 (2011).

[70] S. Müller, M. Mudrich, and F. Stienkemeier, J. Chem. Phys. **131**, 044319 (7 pages) (2009).

[71] T. Döppner, T. Diederich, S. Göde, A. Przystawik, J. Tiggesbäumker, and K.-H. Meiwes-Broer, J. Chem. Phys. **126**, 244513 (7 pages) (2007).

[72] T. Döppner, Ph.D. thesis, Univerität Rostock (2003).

[73] A. W. Hauser, C. Callegari, and W. E. Ernst, in *Advances in the Theory of Atomic and Molecular Systems*, edited by P. Piecuch, J. Maruani, and G. Delgado-Barrio (Springer Science+Business Media B.V., 2009), vol. 20 of *Progress in Theoretical Chemistry and Physics*, pp. 201–215.

[74] L. H. Coudert, W. E. Ernst, and O. Golonzka, J. Chem. Phys. **117**, 7102 (2002).

[75] F. Lackner, Master's thesis, Graz University of Technology (2009).

[76] J. Nagl, Master's thesis, Graz University of Technology (2004).

[77] F. Stienkemeier, M. Wewer, F. Meier, and H. Lutz, Rev. Sci. Instr. **71**, 3480 (2000).

[78] C. Callegari and W. E. Ernst, in: *Handbook of High-Resolution Spectroscopy* edited by M. Quack and F. Merkt (John Wiley & Sons, Chichester, 2011), vol. 3, chap. Helium Droplets as Nanocryostats for Molecular Spectroscopy - from the Vacuum Ultraviolet to the Microwave Regime, pp. 1551–1594, 1st ed.

[79] K. Müller-Dethlefs, M. Sander, and E. Schlag, Chem. Phys. Lett. **112**, 291 (1984).

[80] T. F. Gallagher, Reports on Progress in Physics: Rydberg Atoms **51**, 143 (1988).

[81] E. W. Schlag, ed., *ZEKE spectroscopy* (Cambridge University Press, Cambridge, 1998).

[82] T. F. Gallagher, *Rydberg Atoms. Cambridge Monographs on Atomic, Molecular, and Chemical Physics* edited by A. Dalgarno, P. L. Knight, F. H. Read, and R. N. Zare, vol. 3 (Cambridge University Press, Cambridge, 1994).

[83] W. A. Chupka, J. Chem. Phys. **98**, 4520 (1993).

[84] M. C. R. Cockett, Chem. Soc. Rev. **34**, 935 (2005).

[85] F. Merkt, Annu. Rev. Phys. Chem. **48**, 675 (1997).

[86] G. Scoles, ed., *Atomic and molecular beam methods*, vol. 1 (Oxford University Press, New York, 1988).

[87] H. Wollnik, Mass Spectrom. Rev. **12**, 89 (1993).

[88] M. Guilhaus, J. Mass Spectrom. **30**, 1519 (1995).

[89] N. Mirsaleh-Kohan, W. D. Robertson, and R. N. Compton, Mass Spectrom. Rev. **27**, 237 (2008).

[90] W. C. Wiley and I. H. McLaren, Rev. Sci. Instrum. **26**, 1150 (1955).

[91] P. Dahl, ed., *Introduction to Electron and Ion Optics* (Academic Press, New York, 1972).

[92] C. Flory, R. Taber, and G. Yefchak, Int. J. Mass Spectrom. Ion Processes **152**, 177 (1996).

[93] S. G. Alikanov, Sov. Phys. JETP **4**, 452 (1957).

[94] W. Demtröder, *Laser spectroscopy* (Springer Verlag, Berlin New York, 2003), 3rd ed.

[95] J. Nagl, Ph.D. thesis, Graz University of Technology (2008).

[96] G. Auböck, Ph.D. thesis, Graz University of Technology (2008).

[97] J. E. Sansonetti, J. Phys. Chem. Ref. Data **37**, 1183 (2008).

[98] J. Nagl, G. Auböck, A. W. Hauser, O. Allard, C. Callegari, and W. E. Ernst, J. Chem. Phys. **128**, 154320 (2008).

[99] R. Kurucz and B. Bell, *Atomic line data*, CD-ROM No. 23 (1995).

[100] J. Reho, J. Higgins, K. K. Lehmann, and G. Scoles, J. Chem. Phys. **113**, 9694 (2000).

[101] T. Kinoshita, K. Fukuda, T. Matsuura, and T. Yabuzaki, Phys. Rev. A **53**, 4054 (1996).

[102] G. Auböck, J. Nagl, C. Callegari, and W. E. Ernst, J. Phys. Chem. A **111**, 7404 (2007).

[103] C. L. A. Collins, K. D. Bonin, and M. A. Kadar-Kallen, Opt. Lett. **18**, 1754 (1993).

[104] R. W. Boyd, *Nonlinear Optics*, Burlington, USA (Elsevier, 2008), 3rd ed.

[105] C. Callegari and F. Ancilotto, J. Phys. Chem. A **115**, 6789 (2011).

[106] J. L. Persson, Q. Hui, Z. J. Jakubek, M. Nakamura, and M. Takami, Phys. Rev. Lett. **76**, 1501 (1996).

[107] J. Reho, C. Callegari, J. Higgins, W. E. Ernst, K. K. Lehmann, and G. Scoles, Faraday Discussions **108**, 161 (1997).

[108] R. J. Le Roy and G. T. Kraemer, Chemical Physics Research Report CP-650R^2, University of Waterloo (2004), see the "Computer Programs" link at `http://leroy.uwaterloo.ca`.

[109] M. Zbiri and C. Daul, Physics Letters A **341**, 170 (2005).

[110] F. Ancilotto, M. Pi, R. Mayol, M. Barranco, and K. Lehmann, J. Phys. Chem. A **111**, 12695 (2007).

[111] P. B. Lerner and I. M. Sokolov, JETP Lett. **44**, 644 (1986).

[112] U. Buck and C. Steinbach, J. Phys. Chem. A **102**, 7333 (1998).

[113] L. Bewig, U. Buck, S. Rakowsky, M. Reymann, and C. Steinbach, J. Phys. Chem. A **102**, 1124 (1998).

[114] C. Mundy, J. Hutter, and M. Parrinello, J. Am. Chem. Soc. **122**, 4837 (2000).

[115] *Nist atomic spectra database, v. 3.1.5* (2008), URL `http://physics.nist.gov/PhysRefData/ASD/index.html`.

[116] G. Igelmann, U. Wedig, P. Fuentealba, and H. Stoll, J. Chem. Phys. **84**, 5007 (1986).

[117] K. P. Huber and G. Herzberg, *Molecular Spectra and Molecular Structure* (van Nostrand, New York, 1979), 4th ed.

[118] F. Cardarelli, *Materials Handbook. A Concise Desktop Reference.* (Springer Verlag, London, 2000), 2nd ed.

[119] K. R. Atkins, Phys. Rev. **116**, 1339 (1959).

[120] R. Ahlrichs, H. J. Bohm, S. Brode, K. T. Tang, and J. P. Toennies, J. Chem. Phys. **88**, 6290 (1988).

[121] A. D. Koutselos, E. A. Mason, and L. A. Viehland, J. Chem. Phys. **93**, 7125 (1990).

[122] D. E. Galli, M. Buzzacchi, and L. Reatto, J. Chem. Phys. **115**, 10239 (2001).

[123] E. Coccia, E. Bodo, and F. A. Gianturco, Europhysics Letters **82**, 23001 (2008).

[124] E. Yurtsever, E. Yildirim, M. Yurtsever, E. Bodo, and F. A. Gianturco, European Physical Journal D **43**, 105 (2007).

[125] K. K. Lehmann and J. A. Northby, Mol. Phys. **97**, 639 (1999).

[126] G. Auböck, M. Aymar, O. Dulieu, and W. E. Ernst, J. Chem. Phys. **132**, 054304 (7 pp.) (2010).

[127] E. Coccia, E. Bodo, F. Marinetti, F. Gianturco, E. Yildrim, M. Yurtsever, and E. Yurtsever, J. Chem. Phys. **126**, 124319 (2007).

[128] G. Droppelmann, O. Bünermann, C. P. Schulz, and F. Stienkemeier, Phys. Rev. Lett. **93**, 23402 (2004).

[129] H. Buchenau, E. L. Knuth, J. Northby, J. P. Toennies, and C. Winkler, J. Chem. Phys. **92**, 6875 (1990).

[130] G. Douberly, private communication (2011).

[131] S. L. Broadley, T. Vondrak, and J. M. C. Plane, Phys. Chem. Chem. Phys. **9**, 4357 (2007).

[132] A. W. Castleman, Advances in Colloid and Interface Science **10**, 73 (1979).

[133] B. Roux and R. MacKinnon, Science **285**, 100 (1999).

[134] M. Koch, G. Auböck, C. Callegari, and W. Ernst, Phys. Rev. Lett. **103**, 035302 (4 pp.) (2009).

[135] O. Bünermann, M. Mudrich, M. Weidemüller, and F. Stienkemeier, J. Chem. Phys. **121**, 8880 (2004).

[136] O. Bünermann, G. Droppelmann, A. Hernando, R. Mayol, and F. Stienkemeier, J. Phys. Chem. A **111**, 12684 (2007).

[137] S. Paolini, F. Ancilotto, and F. Toigo, J. Chem. Phys. **126**, 124317 (2007).

[138] J. Pascale, Phys. Rev. A **28**, 632 (1983), data published as Technical Report, Service de Physique des Atoms et des Surfaces (C.E.N. Saclay), Gif sur Yvette-Cedex, France, 1983.

[139] F. Dalfovo, A. Lastri, L. Pricaupenko, S. Stringari, and J. Treiner, Phys. Rev. B **52**, 1193 (1995).

[140] R. Schmied, Ph.D. thesis, Princeton University (2006).

[141] R. J. Le Roy, Chemical Physics Research Report CP-663, University of Waterloo (2007), see the "Computer Programs" link at `http://leroy.uwaterloo.ca`.

[142] K. Enomoto, K. Hirano, M. Kumakura, Y. Takahashi, and T. Yabuzaki, Phys. Rev. A **66**, 42505 (2002).

[143] M. Zbiri and C. Daul, Journal of Chemical Physics **121**, 11625 (2004).

[144] P. Moroshkin, A. Hofer, D. Nettels, S. Ulzega, and A. Weis, Journal Of Chemical Physics **124**, 24511 (2006).

[145] W. E. Ernst, R. Huber, S. Jiang, R. Beuc, M. Movre, and G. Pichler, J. Chem. Phys. **124**, 24313 (2006).

[146] I. Gilmore and M. Seah, International Journal of Mass Spectrometry **202**, 217 (2000).

[147] U. Kleinekathöfer, M. Lewerenz, and M. Mladenovic, Phys. Rev. Lett. **83**, 4717 (1999).

[148] U. Kleinekathöfer, K. Tang, J. Toennies, and C. Yiu, Chem. Phys. Lett. **249**, 257 (1996).

[149] M. Leino, A. Viel, and R. E. Zillich, J. Chem. Phys. **129**, 184308 (2008).

[150] M. Leino, A. Viel, and R. Zillich, J. Chem. Phys. **134**, 024316 (2011), ISSN 0021-9606.

[151] E. Loginov and M. Drabbels, Phys. Rev. Lett. **106**, 083401 (2011).

[152] A. Golov and S. Sekatskii, Z. Phys. D **27**, 349 (1993).

[153] H. G. Limberger and T. P. Martin, J. Chem. Phys. **90**, 2979 (1989).

[154] T. Bergmann and T. P. Martin, J. Chem. Phys. **90**, 2848 (1989).

[155] H. Göhlich, T. Lange, T. Bergmann, U. Näher, and T. P. Martin, Chem. Phys. Lett. **187**, 67 (1991).

[156] D. Bellert and W. H. Breckenridge, Chemical Reviews **102**, 1595 (2002).

[157] C. P. Schulz, P. Claas, D. Schumacher, and F. Stienkemeier, Phys. Rev. Lett. **92**, 13401 (2004).

[158] S. de Visser, D. Danovich, and S. Shaik, Phys. Chem. Chem. Phys. **5**, 158 (2003).

[159] E. Loginov, L. F. Gomez, and A. F. Vilesov, J. Phys. Chem. A **115**, 7199 (2011).

[160] E. L. Knuth, J. Chem. Phys. **107**, 9125 (1997).

[161] M. Foucrault, P. Millie, and J. P. Daudey, J. Chem. Phys. **96**, 1257 (1992).

[162] B. Assadollahzadeh, C. Thierfelder, and P. Schwerdtfeger, Phys. Rev. B **78**, 245423 (11 pp.) (2008).

[163] K. R. S. Chandrakumar, T. K. Ghanty, and S. K. Ghosh, J. Chem. Phys. **120**, 6487 (2004).

[164] A. Banerjee, T. K. Ghanty, and A. Chakrabarti, J. Phys. Chem. A **112**, 12303 (2008).

[165] A. W. Hauser, G. Auböck, C. Callegari, and W. E. Ernst, J. Chem. Phys. **132** (2010).

[166] A. W. Hauser, G. Auböck, and W. E. Ernst, in *Vibronic Interactions and the Jahn-Teller Effect I: Theory*, edited by C. Daul (Springer, 2011 in press), Progress in Theoretical Chemistry and Physics.

[167] B. S. Kim and K. Yoshihara, Chemical Physics Letters **202**, 437 (1993).

[168] C. Stark and V. V. Kresin, Phys. Rev. B **81**, 085401 (2010).

[169] D. Ross, J. E. Rutledge, and P. Taborek, Science **278**, 664 (1997).

[170] W. Ekardt, W.-D. Schöne, and J. Pacheco, in: *Metal Clusters* edited by W. Ekardt (John Wiley & Sons Ltd., Chichester, 1999), chap. Application of the Jellium Model and its Refinements to the Study of the Electronic Properties of Metal Clusters, pp. 1–27, John Wiley's Series in Theoretical Chemistry.

[171] W. D. Knight, K. Clemenger, W. A. de Heer, W. A. Saunders, M. Y. Chou, and M. L. Cohen, Phys. Rev. Lett. **52**, 2141 (1984).

[172] W. A. de Heer, Rev. Mod. Phys. **65**, 611 (1993).

[173] I. M. L. Billas, A. Chatelain, and W. A. DeHeer, Science **265**, 1682 (1994).

[174] K. D. Bonin and V. V. Kresin, *Electric-dipole polarizabilities of atoms, molecules, and clusters* (World Scientific, 1997).

[175] J. Harms and J. P. Toennies, J. Low Temp. Phys. **113**, 501 (1998).

A. Appendix

Typical He droplet sizes and radii

Within this thesis and in several of our works the He droplet sizes were of great importance. We therefore display a short table with typical mean sizes of He droplets and their radii, which may be of practical importance. The radial size of the He droplet is expected as spherical in the ground state so that its radius can be estimated easily with the equilibrium distance between single He atoms

$$R = r_0 N^{1/3}. \tag{A.1}$$

$r_0 = 2.22\,\text{Å}$ is the unit radius of ^{4}He and N is the number of He atoms in the cluster.[32] Typical combinations of stagnation pressure p_0 and nozzle temperature T_0 (for orifices of a $5\,\mu$m diameter) to obtain $\bar{N}$ have been measured in Ref. 29. With droplet size scaling laws[160] missing values can be estimated. The often used pressure $p_0 = 60\,\text{bar}$ is superior to $p_0 = 40\,\text{bar}$ in terms of intensity as the mass flow scales with $\frac{p_0}{\sqrt{T_0}}$. Unfortunately only vague measurements of $\bar{N}$ with $p_0 = 60\,\text{bar}$ in Ref. 26 are known to us. Therefore we recommend to use pressures p_0 of 40 or 80 bar instead of 60 bar, if one needs to know the He droplet sizes precisely in an experiment. Please note that the He droplet sizes have a size distribution, which is lognormal in the subcritical expansion mode, with $\bar{N}$ as the average cluster size. As a rule of thumb the full width at half maximum (FWHM) of this size distribution equals $\bar{N}$, so that $\Delta N \sim \bar{N}$.

Table A.1.: Typical mean He droplet sizes $\bar{N}$ and radii $\bar{R}$ for different combinations of p_0 and T_0. [a] In Ref. 175 $\bar{N}$ is given with 8900 He atoms ($\bar{R} \sim 46.0\,\text{Å}$). We estimate for this combination $\bar{N} = 9400$ He atoms ($\bar{R} \sim 46.6\,\text{Å}$).

$\bar{N}$ / He atoms	$\bar{R}$ / Å	p_0 / bar	T_0 / K	Ref.
0.7×10^3	19.7	40	24.0	29
1.0×10^3	22.2			
1.7×10^3	26.5	40	22.0	29
2.0×10^3	28.0			
2.1×10^3	28.4	80	26.0	29
2.2×10^3	28.9	60	22.4	26
2.6×10^3	30.5	40	20.0	29
3.0×10^3	32.0			
3.1×10^3	32.4	80	24.0	29
4.0×10^3	35.2			
4.7×10^3	37.2	40	18.0	29
5.0×10^3	38.0			
5.2×10^3	38.5	60	19.4	26
6.0×10^3	40.3			
6.1×10^3	40.6	40	17.0	29
6.5×10^3	41.4	80	20.0	29
7.0×10^3	42.5			
7.7×10^3	43.8	40	16.0	29
8.0×10^3	44.4	60	17.5	26
8.4×10^3	45.1	40	15.5	estimated
[a] 8.9×10^3	46.0	40	15.0	29
9.0×10^3	46.2			
9.5×10^3	47.0	80	18.0	29
10.0×10^3	47.8			
10.5×10^3	48.6	40	14.5	estimated
11.8×10^3	50.6	40	14.0	estimated
12.0×10^3	50.8			
12.2×10^3	51.1	60	15.4	26
13.0×10^3	52.2	40	13.5	29
14.8×10^3	54.5	40	13.0	estimated
16.6×10^3	56.6	40	12.5	estimated
18.6×10^3	58.8	40	12.0	estimated
20.9×10^3	61.2	40	11.5	estimated